2016

An Engineered Installation Aid Device For Child Restraint System to Mitigate Misuse

Xinqi Chen
University of Windsor

An Engineered Installation Aid Device For Child Restraint System to Mitigate Misuse

By

Xinqi Chen

A Thesis
Submitted to the Faculty of Graduate Studies
through the Department of **Mechanical, Automotive, and Materials Engineering**
in Partial Fulfillment of the Requirements for
the Degree of Master of Applied Science
at the University of Windsor

Windsor, Ontario, Canada

2016

AN ENGINEERED INSTALLATION AID DEVICE FOR CHILD RESTRAINT SYSTEM TO MITIGATE MISUSE

by

Xinqi Chen

APPROVED BY:

_____

B. Minaker
Department of Mechanical, Automotive,
and Materials Engineering

_____

H. Hu
Department of Mechanical, Automotive,
and Materials Engineering

_____

W. Altenhof, Advisor
Department of Mechanical, Automotive,
and Materials Engineering

09/14/2016

DECLARATION OF ORIGINALITY

I hereby certify that I am the sole author of this thesis and that no part of this thesis has been published or submitted for publication.

I certify that, to the best of my knowledge, my thesis does not infringe upon anyone's copyright nor violate any proprietary rights and that any ideas, techniques, quotations, or any other material from the work of other people included in my thesis, published or otherwise, are fully acknowledged in accordance with the standard referencing practices. Furthermore, to the extent that I have included copyrighted material that surpasses the bounds of fair dealing within the meaning of the Canada Copyright Act, I certify that I have obtained a written permission from the copyright owner(s) to include such material(s) in my thesis and have included copies of such copyright clearances to my appendix.

I declare that this is a true copy of my thesis, including any final revisions, as approved by my thesis committee and the Graduate Studies office, and that this thesis has not been submitted for a higher degree to any other University or Institution.

ABSTRACT

This research focuses on the development of a child restraint system installation-aid device (CRSIAD) for the purpose of mitigating child safety seat misuse in terms of installation. A geometric study was performed base on surveying dimensions of currently existing child safety seat products. Material property experiments were conducted to develop an anisotropic wood material model for the CRSIAD in order to virtually evaluate device stress levels. Finite element analysis (FEA) of both the material model and CRSIAD were performed in comparison with lab test data to validate structural performance. The CRSIAD was then fabricated and finalized after multiple design iterations for geometry and components based on in-car testing. User satisfaction survey and professional review by certified CRS installation personnel were completed to ensure the value of CRSIAD as well as provide feedback for future improvements. From the testing results and user feedbacks, the CRSIAD was believed to be an important contribution towards the improvement of child safety in vehicles.

DEDICATION

For my loving parents who have supported me to complete this thesis and my Master's degree.

ACKNOWLEDGEMENTS

The author would like to thank his academic advisor, Dr. William Altenhof, for his motivation, guidance, valuable comments, patience, suggestions and encouragements throughout the duration of this research. The author would also like to thank Dr. Bruce Minaker, Dr. Henry Hu and their group for their valuable information and knowledge of supporting this research. Sponsorship from Spartan Slings, Inc was greatly appreciated.

TABLE OF CONTENTS

LIST OF TABLES

LIST OF FIGURES

LIST OF APPENDICES

LIST OF ABBREVIATIONS

FAAP	Fellow in the American Academy of Pediatrics
ASTM	American Society for Testing and Materials
CMVSS	Canadian Motor Vehicle Safety Standards
CRS	Child Restraint System
CRSIAD	Child Restraint System Installation Aid Device
FMVSS	Federal Motor Vehicle Safety Standards
HIC	Head Injury Criteria
NICU	Neonatal Intensive Care Unit

NOMENCLATURE

B, D	Softening parameters (parallel and perpendicular)
C_I, C_{II}	Constants that relate fracture intensity to fracture energy
C_{ijkl}	Material stiffness tensor (elastic moduli)
C_{ij}	Material stiffness components
$c\|\|, c\perp$	Hardening-rate parameters (parallel and perpendicular)
$d, d\|\|, d\perp, d_m$ and $max(d\|\|,d\perp)$	Scalar damage parameters (general, parallel, perpendicular,
$d_{max}\|\|, d_{max}\perp$	Maximum damage allowed (parallel and perpendicular)
E_{11}, E_{22}, E_{33}	Normal moduli of an orthotropic material
E_L, E_T	Normal moduli (wood notation)
F_M, F_S	Factors to scale moduli and strengths with temperature
$f\|\|, f\perp$	Yield surface functions (parallel and perpendicular)
$f\|\|^*, f\perp^*$	Trial elastic yield surface functions (parallel and perpendicular)
$G\|\|, G\perp$	Hardening model translational limit functions (parallel and perpendicular)
$G_f\|\|, G_f\perp$	Fracture energies (tension and shear)
$G_{fI}\|\|, G_{fII}\|\|$	Parallel fracture energies (tension and shear)
$G_{fI}\perp, G_{fII}\perp$	Perpendicular fracture energies (tension and shear)
G_{hard}	Hardening parameter to override perfect plasticity

G_{12}, G_{13}, G_{23}	Shear moduli of an orthotropic material
G_{LT}, G_{LR}, G_{TR}	Shear moduli (wood notation)
I_1, I_2, I_3, I_4	Stress invariants of a transversely isotropic material
I_1^*, I_2^*, I_3^*, I_4^*	Trial elastic stress invariants
K_I, K_{II}	Fracture intensities (tension and shear)
L	Element length
M_C	Moisture content
$n\|\|$, $n\perp$	Rate-effect power parameters (parallel and perpendicular)
$N\|\|$, $N\perp$	Hardening initiation parameters (parallel and perpendicular)
Q_T, Q_C	Quality factors (tension/shear and compression)
R	Stress enhancement factors (ratio of dynamic to static strength)
S_{ij}	Compliance coefficients (reciprocals of elastic moduli)
$S\|\|$, $S\perp$	Shear strengths (parallel and perpendicular)
T	Temperature
V	Impact velocity in Hopkinson pressure bar tests
X, X_T, X_C	Parallel wood strengths (general, tension, and compression)
Y, Y_T, Y_C	Perpendicular wood strengths (general, tension, and compression)
α_{ij}	Backstress tensor (and incremental backstress for hardening model
γ, $\gamma\|\|$, $\gamma\perp$	Viscoplastic interpolation parameters (general, parallel, and perpendicular)

ε_{ij}, $\Delta\varepsilon_{ij}$	Strain tensor and strain increments
ε_{11}, ε_{22}, ε_{33}, ε_{12}, ε_{13}, ε_{23}	Strain components of an orthotropic material
ε_1, ε_2, ε_3, ε_4, ε_5, ε_6	Strain components (shorthand notation)
ε_L, ε_T, ε_R, ε_{LT}, ε_{LR}, ε_{TR}	Strain components (wood notation)
$\Delta\varepsilon_L$,$\Delta\varepsilon_{LR}$, $\Delta\varepsilon_{LT}$	Strain-rate increments parallel to the grain (wood notation)
$\Delta\varepsilon_T$, $\Delta\varepsilon_R$, $\Delta\varepsilon_{TR}$	Strain-rate increments perpendicular to the grain (wood notation)
$\varepsilon\|\|$,$\varepsilon\perp$	Scalar effective strain rates (parallel and perpendicular)
$\Delta\varepsilon\|\|$, $\Delta\varepsilon\perp$	Scalar effective strain-rate increments (parallel and perpendicular)
$\Delta\lambda\|\|$, $\Delta\lambda\perp$	Plasticity consistency parameters (parallel and perpendicular)
Δt	Time-step increment
η	General rate-effect fluidity parameter
$\eta\|\|$, $\eta\perp$	Tension/shear rate-effect fluidity parameters (parallel and perpendicular)
$\eta_c\|\|$, $\eta_c\perp$	Compression rate-effect fluidity parameters (parallel and perpendicular)
ρ, ρ_s	Density of wood and of wood solid phase
σ_{11},σ_{22}	Ultimate yield surfaces (parallel and perpendicular)

σ_{ij}, σ_{ij}, σ_{ij},σ_{ij}, σ_{ij} Stress tensors (trial elastic, inviscid, inviscid with backstress, viscid, and viscid with damage)

σ_{11}, σ_{22}, σ_{33} Stress components of an orthotropic material

σ_{12}, σ_{13}, σ_{23}

σ_{1}, σ_{2}, σ_{3} Stress components (shorthand notation)

σ_{4}, σ_{5}, σ_{6}

σ_{L}, σ_{T}, σ_{R} Stress components (wood notation)

σ_{LT}, σ_{LR}, σ_{TR}

$\tau||$, $\tau\perp$ Instantaneous strain energy type term for damage accumulation

$\tau_0||$, $\tau_0\perp$ Initial strain energy type value for damage initiation

ν_{ij} Poisson's ratios (indicial notation)

ν_{LT}, ν_{LR}, ν_{TR} Major Poisson's ratios (wood notation)

Subscripts

L Longitudinal or parallel

T Transverse or perpendicular

R Radial

|| Parallel

$\perp$ Perpendicular

1 INTRODUCTION

Motor vehicle injuries are leading causes for death among children in North America. Children especially infants, due to their body size and weight, are very vulnerable to impact from the car crash. In 2013, total of 8925 injuries of children under age of 14 were reported in Canada [31], among which 430 were seriously injured.

A Child Restraint System (CRS) can greatly reduce the risk for children's injury during car accidents. With appropriate use of a CRS, risk for infants (less than one year old) can be reduced by 71% and 54% for toddlers (aged between one and four) in passenger vehicles [30].

One key component in the vehicle for installing a CRS is LATCH (Lower Anchors and Tethers for Children). LATCH became standard equipment, by law, for all passenger vehicles on September 1st, 2002, which was enforced by NHTSA (Federal Motor Vehicle Safety Standard 225) [1]. Prior to 2002, only car seatbelts were used to restrain Child Restraint Systems (CRSs) in into the car seat, which was proved inadequate to provide the same safety level as a LATCH system. Many vehicle owners who installed CRSs with car seatbelts loosely installed the CRSs so that effective restraining was not achieved [2]. LATCH allows CRS to be tightly and appropriately secured into the car seat so that the CRS will perform at its best capability during a car accident, which drastically reduces the chances of injuries and fatalities of the child occupant.

LATCH started with a good concept but misuse of it can put infants at increased risks of injury in a car crash. Without correctly attaching a CRS with LATCH system, neither the structure of the CRS or the function of LATCH will help reducing the risk of injury. A recent major survey was completed between November 2013 and May 2014 at Oregon Health and Science University Hospital

has revealed a disturbing quantity of CRS misuse among 267 participating families; 93% of installations contained at least one critical error [7]. Another similar large scale survey completed in 2005 [8] resulted in 13% of participants not using LATCH. For the 87% who did use LATCH, only 4% of them made no error in the installation.

The statistics shown above have indicated no significant improvement of children's safety for the last decade mainly due to misuse of LATCH system. With the existing design of the LATCH system on the passenger vehicles, there is no other way a CRS can be installed differently in near future. Correspondingly, the need for a supplemental device, to reduce human effort during installation, could play a significant role in reducing the CRS installation errors and thus mitigate misuse and increase child safety in vehicles.

2. LITERATURE REVIEW

2.1 LATCH Theory

On the vehicle, lower anchor bars are fitted where cushions meet in the car backseat as shown in Figure 1. The locations of the anchor bars are standardized for all car manufacturers.

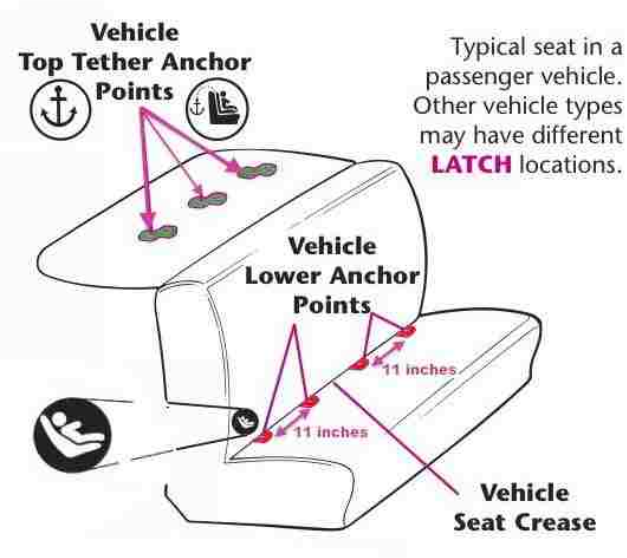

Figure 1.Typical LATCH system on passenger vehicle seat [3].

On the CRS, there are two main webbing harnesses. The lower webbing B in Figure 2 is designed to wrap across the CRS in the lateral direction with two ends that directly clip into the lower anchor locations in the car seat. The lower anchor webbing fastens the CRS into the car seat to minimize lateral and forward movement of the CRS relative to the vehicle. The top webbing A is the top tether that will secure the top portion of CRS to prevent longitudinal movement of the CRS in the car, which effectively reduces head injury during a car accident. For forward-facing installation, the location where the top tether is attached depends on the vehicle and the location of the vehicle interior. If a CRS is installed in the backseat of a sedan, the top tether attach point will be located in the rear deck underneath the

rear window (Point 1 in Figure 2). If the CRS is installed on the second-row seat of a minivan, the location will be on the floor behind the seat (Point 2 in Figure 2).

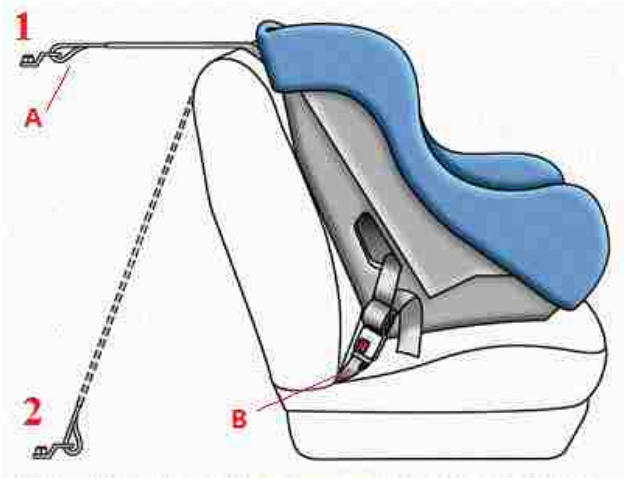

Figure 2. CRS with both top tether and lower anchor webbing [4].

The introduction of LATCH evolved the CRS industry. The main improvement on safety can be described in the following two aspects.

1. Using of the lower anchors instead of seatbelt to restrain the CRS eliminates the need to know how to use the seatbelt or locking clip to install the CRS which had been the core of misuse prior to 2002. The use of LATCH was proved to be an easier method to install the CRS than the use of seatbelt as it provides a tighter fit than the seatbelt itself [5].

2. The introduction of applying a top tether on the CRS effectively reduces forward head excursion of infant during a car accident event. Without a top tether being attached to the CRS, the top portion of CRS will be loose. The slack on the top portion of the CRS will increase the chance of infant's head movement during a car accident. Potential for head contact with vehicle interior parts will increase and cause severe head injuries. Therefore, such chance of head contact is effectively lowered with the use of top tether [6].

2.2 Statistics Associated with LATCH Misuse

Misuse of a CRS can put infants at increased risk of injury in a car crash. A recent major survey was completed between November 2013 and May 2014 at the Oregon Health and Science University Hospital which has revealed a disturbing quantity of CRS misuse among 267 participating families; 93% of installations have contained at least one critical error [7]. The study was conducted with the purpose of estimating the rate of CRS misuse of newborns upon hospital discharge as well as elucidating risk and protective factors for CRS misuse.

At the Oregon Health and Science University Hospital, The Mother Baby Unit discharges about 2500 newborn babies every year. Selected sampling was done on daily basis to ensure the data collected was legitimate. The newborns with less than thirty-seven weeks of gestation age, with Neonatal Intensive Care Unit (NICU) stay over four hours and leaving in personal vehicles were chosen for the experiment. Up to four new mother/infant dyads were surveyed everyday between November 2013 and May 2014. Participants' tasks were to simply place their baby in the CRS and install the CRS into the car that they were leaving with. During the installation process, a certified Child Passenger Safety (CPS) Technician observed these activities and recorded all cases of misuse according to the best-practice guidelines of the Safety Kids Worldwide and American Academy of Pediatrics (APP).

Results from Table 2 present the leading cause of misuse being loose installation. The main focus of this research is on CRS installation errors and results from the most common installation errors showed 43% of participants involved loose installation of either the upper or lower LATCH tethers. The interim analyses suggest that nearly all parents with newborns presented critical misuse on the CRS installation that might lead to increased risk of injury or death.

Most Common Errors in Positioning Infant	Percentage (%)
Harness too loose	69
Retainer clip too low	34
Use of after-market product not approved with seat	20
Harness too high	18
Caregiver not knowing how to adjust harness	15

Table 1. Error Percentage for Infant Positioning [7].

Most Common Installation Errors	Percentage (%)
CRS installed too loosely	43
Angle of car safety seat incorrect	36
Safety belt used but not locked	23
Incorrect spacing between CRS and vehicle front seat	17

Table 2. Error Percentage for CRS Installation [7].

The results from the experiment noted above showed similarity to an experiment conducted in 2005 by the NHTSA, which was completed over a decade ago at the publishing date of this thesis. Between April and October 2005, NHTSA conducted a survey specifically for the misuse of LATCH [8]. This study was the first large-scaled survey specially designed to study LATCH misuse. They engaged the survey at 66 places including shopping centers, child care facilities, health care centers and recreation facilities in 7 states in the USA. NHTSA focused on whether or not drivers with LATCH-equipped vehicles were using LATCH to secure their CRSs to the vehicles and if the CRSs were properly installed. The make, model and type of CRS installed in each seating position were recorded for each of the vehicles. Demographic characteristics and the type of CRS were collected for each vehicle. The information was gathered about the driver's knowledge of LATCH as well as their opinions on how easy it was to use LATCH.

Our best interest of the survey is the data for the lower anchor misuse. Observations showed that 13% of the CRSs were installed in a seat where lower anchors were not equipped, which is the centre seat of the vehicle backseat. For the remaining 87% who did place the CRS at the right location, 40% of these parents did not use the lower anchors bars at all because they relied using the car seatbelt to restrain the CRS. Even if the remaining 60% of participants used lower anchor to attach the CRSs to the vehicle, a significant amount of misuse was identified.

From the entire survey, 52.2% used lower anchors as the method to secure their CRSs and protect their children from car accidents. The ones who did not use lower anchors suggested their lack of knowledge is the primary cause. Figure 3 presents details of the misuse of lower anchors among this survey.

From this chart, the highest percentage of lower anchor misuse appeared to be loose installation. This means the CRS can be moved from side to side for more than one inch after the installation was complete. Loose lower anchor straps will not securely hold the CRS down to the car seat upon an accident, which causes additional slack in the CRS that could lead to increased risk of the occupant's injury and death.

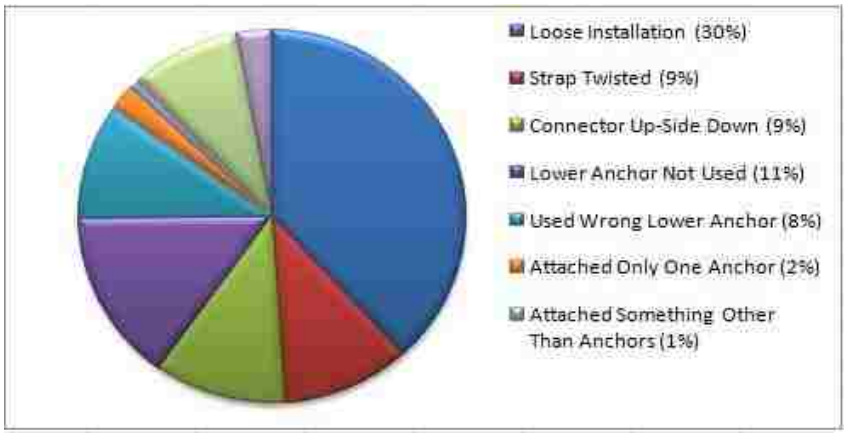

Figure 3. Chart Distribution of Types of Misuse [8].

The two large-scale surveys mentioned above are ten years apart from each other but results are similarly disturbing. With no significant improvement on CRS misuse over the last ten years, it is vital to find out the leading cause of CRS installation misuse. Although CRSs are made as intuitively as possible with clear instructions attached, parents with newborns still tend to misuse them. The experiment performed in 2009 by Tsai and Perel focused on installation errors among both novice and experienced users [9]. Common mistakes presented in both the novice and experienced groups of participants but the novice group showed more errors than the experienced group. The results were consistent with the experiment lead by Benjamin Hoffman, MD, FAAP [7], in which lack of knowledge on CRS installation played a big role in CRS misuse. In 2004, Transport Canada conducted an environmental scan of educational initiatives aimed at increasing physicians understanding of CRS, which identified pediatricians as having lack of understanding for the correct seating of CRS in motor vehicles [10].

2.3 Physical Effort That Leads To LATCH Misuse

Evidence was found from the major survey in 2005 lead by Decina and Lococo that majority of people underestimated the effort and purpose of using lower anchors [11]. From the experiment, "Ease-of-use" ratings among the drivers who attached lower anchor straps to their vehicles were evaluated. The results showed 74% of them indicated "very easy" or "relatively easy". However, the statistics indicated more than half of the installations were incorrect, in which loose installations occupied 30% of the misuse. Figure 4 shows the tightening process of installing the CRS into the backseat of a passenger vehicle which required the installer to bend into an awkward posture on the CRS within the tight vehicle interior space.

Figure 4. CRS installation for forward-facing configuration by certified CRS installer.

CRS misuse is not only caused by lack of education and understanding but also the physical effort needed from the parents and caregivers who perform the installation. An important experiment of performing CRS installation was conducted in 2006 to specifically study the physical effort needed to complete the installation [12]. A group of twenty-seven parents were gathered to install a CRS into a mocked-up second row seat of a minivan. These parents did not have prior experience of installing CRSs which represented the majority of the population. Electrogoniometers were fitted on participants' bodies to measure their body joint extension and radial deviation. Additionally, muscle activation was also assessed in the study. Since this experiment emphasized the effort of correct CRS installation, all participants were guided to a successful installation except two.

Electromyography (EMG) and kinematic data was extracted as illustrated in Figures 5 and 6, below. Results of Figure 5 showed that some muscles reached over 50% level of strength. When taking the highest activations observed across some participants, some muscles had peak levels of 100% during the seat installation and

tethering. The peak levels were observed to be over 90% of maximum in 18 of 30 muscles. Figure 6 shows that the shoulders were forced into extreme postures during all 3 tasks, which were installing seat, securing tether and placing child.

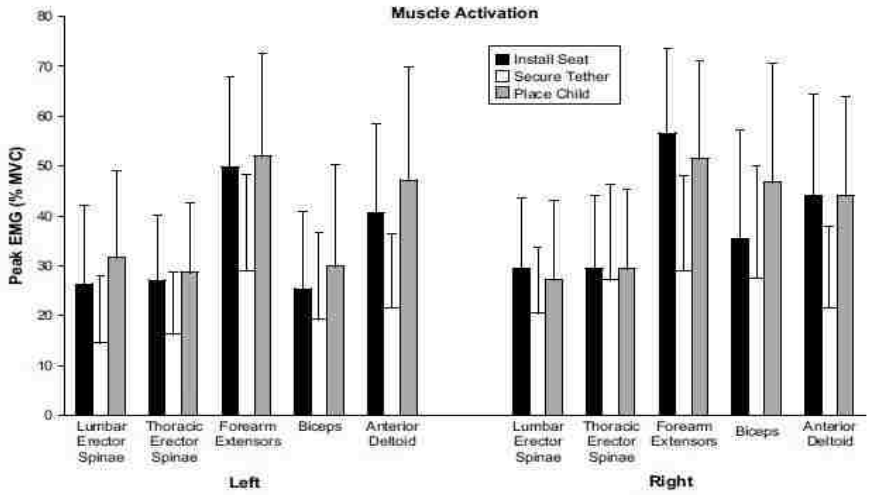

Figure 5. Average peak (99th percentile) EMG amplitudes for each muscle and condition [12].

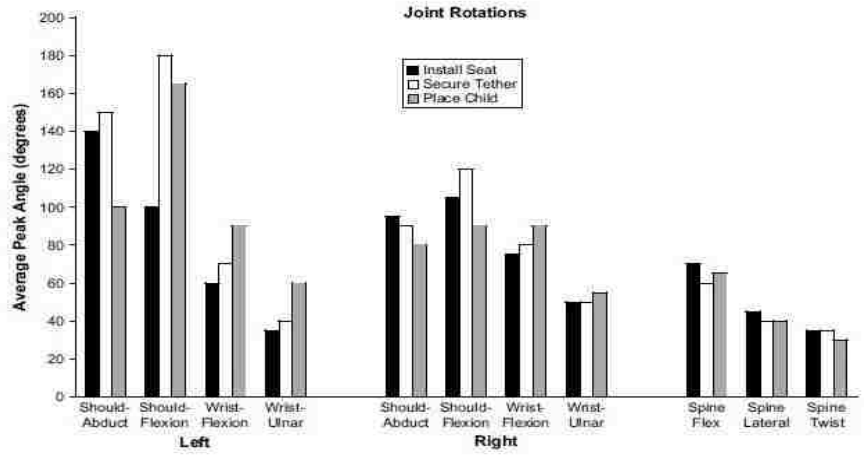

Figure 6. Peak (99th percentile) of average frequency distribution curves for the kinematic data for each joint axis and condition [12].

Therefore, correct CRS installation was found to be very physically demanding. Maximum effort of some muscles could result in inadequate securing of the CRS into the vehicle. The seat installation typically requires high efforts and awkward postures for tightening the upper and lower LATCH straps. These demanding tasks result in loose installation being a frequent misuse characteristic. Even for large size vehicles, the necessary workspace to for CRS installation is tight and requires the installer to bend down and sit on his/her knees to complete installation.

2.4 Effect of Loose LATCH Installation

The use of LATCH started with a good concept but formed a new direction of misuse [6]. LATCH did not increase the safety for children in car accident due to its unfortunate misuse. The leading cause of CRS misuse is loose installation, which is caused by human error due to both lack of understanding and physical demands for correct installation.

The effect of loose LATCH tethers on CRS during a car accident is important to study to find out the level of safety risk for the occupant. Due to high cost of conducting real experiments involving crash test dummies and experimental crashworthiness facilities, numerical simulation is cost-efficient in analyzing a child sized crash test dummy's damage under different crash events.

In the numerical study in 2002 [13], simulations were run to investigate head and neck injuries sustained by toddlers due to CRS misuse under frontal and side impact crashes. Finite element dummy models created based on a 3 year-old child called Hybrid III and Q3 were used in this study. Tests were done according to CMVSS 208 and FMVSS213 testing conditions [14].

Three main scenarios were simulated for both frontal and side impact crashes – No misuse, misuse with slack in seatbelt and misuse of top tether. Seatbelt slack results can also be considered as slack in lower anchor tether as in both cases the

lower portion of CRS is not tightly fastened into the car seat. Simulation predictions illustrating the kinematics of a CRS and 3 year old Q3 dummy for both correct CRS installation and misuse, as presented in Figure 5, has indicated significant difference between the motion of the two different configurations.

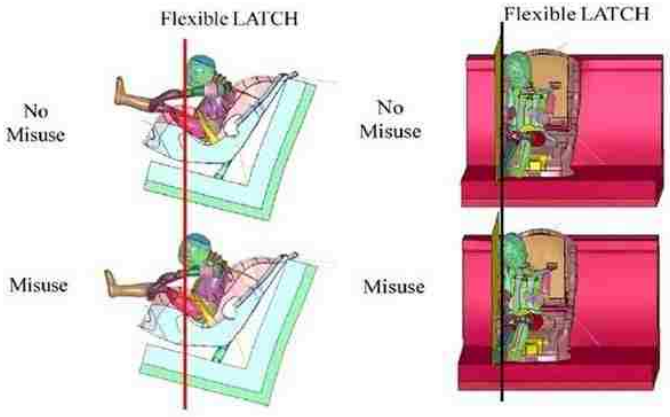

Figure 7. Comparison results for correct and loose LATCH installation for forward collision (left) and side impact (right) scenarios [13].

Acceleration based parameter Head Injury Criterion (HIC) was used to measure head injury risk quantitatively in the crash simulations. In this simulation, HIC_{15} and HIC_{36} were used as appropriate measurements to evaluate head injury according to NHTSA [15]. The results have shown an increase in peak resultant head acceleration by about 12% for the frontal crash condition and 15% for the near-side impact condition due to the lower portion of CRS not being tied down to the car seat properly (slack in seatbelt). Forward head excursion during the crash event was increased by approximately 20% for the Hybrid III dummy due to the presence of slack in the lower portion of CRS.

The HIC_{15} was found to increase by about 35% for the frontal impact and 15% for the near-side impact for the Q3 dummy as a result of misuse. The presence of slack in the CRS will increase the probability of acceleration induced injuries to the

children. For both frontal and near-side impact conditions, neck forces were increased by 5-10% for the Hybrid III dummy and 15-25% for the Q3 dummy due to the slack in lower portion of CRS. Additionally, an increase of approximately 15% of resultant upper neck forces was observed for the same slack in the system.

The increased head acceleration may not lead to death but certainly increases the probability for both brain and neck injuries for the infants. Increased head excursion will raise the potential for contact with vehicle interior parts especially in side-impact cases.

2.5 Review of Loose CRS Installation Errors

Loose installation has been identified as the major cause of CRS misuse. In order to perform a thorough study on how loose installation errors can be eliminated, it is vital to review CRS installation procedures and identify the steps that are causing misuse. Installation procedures can be found on Service Ontario Ministry of Transportation website online [16] and NHTSA official website [15]. A flow chart of proper CRS installation process is shown in Figure 8 as reference.

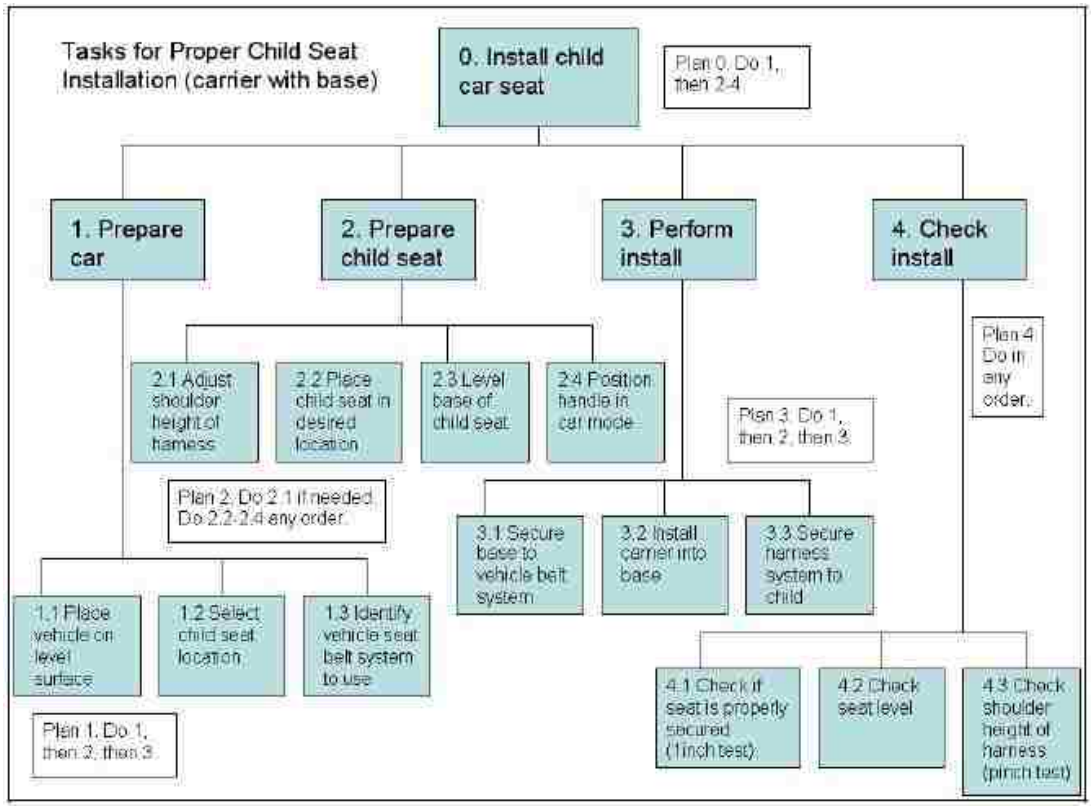

Figure 8. Hierarchical Task Analysis of proper CRS installation [9].

An experimental focused study on CRS installation errors was conducted in 2009 and has shown 85% of loose installation on convertible CRSs [9]. Tightening of the CRS into the car seat was found to be the most challenging task in the installation process. The main issues of CRS installation have been identified as the following:

1. Space - Vehicle interior space is a key limitation for CRS installation. After placing a CRS onto the car seat, the room for the installer to work with the CRS is very limited. Reaching the LATCH strap and tighten it will require some extreme posture of the upper body [12].

2. Instructions - Many parents have been found to become confused between using car seatbelt and LATCH system to fasten a CRS [11]. Some users found the instructions difficult to understand so that they followed wrong instruction order to perform the CRS installation. Some parents complained about the lack of warning signs on the CRS for tightening the system.

3. Adding weight - Most parents did not understand how to get CRS installed in an appropriately tight manner. Some parents ignored the step of placing knees onto the CRS when tightening the LATCH strap because they were not aware that adding weight is the only way to achieve an appropriately tight installation [1]. Some parents were unable to complete the step due to space limitation. For rearward-facing installation, placing a knee onto the CRS was not feasible so hand pressing was needed, in which case an amount of pressure is applied subjectively and is limited by the installer's strength. In some extreme cases where two-door vehicles are used for CRS installation, performing such a step would become very challenging in the limited space in the rear interior compartment.

3 FOCUS OF RESEARCH

After a thorough investigation on the literature regarding child safety in passenger vehicles, it was evident that misuse of CRS is an alarming issue that needs to be addressed. Specific to loose LATCH tether connections, CRS misuse is a result of both human error and inability to provide suitable preloads to the tethers.

Correct installation of LATCH tethers is vital for a CRS to perform as designed. However, from numerous major surveys conducted in North America, the majority of parents are unable to perform correct installation of CRS with the LATCH system. Lack of experience is the first factor that contributes to human error [1]. Most installers of CRSs are new parents who have never previously performed a CRS installation. They were confused by the installation manual and unsure how the LATCH system should be correctly installed. They easily overlook the required tightness of LATCH straps for the CRS to work safely in the vehicle [5].

Tightening LATCH straps in the vehicle is a challenging task due to space limitations and the required physical effort [12]. With the existing design of LATCH system on automobiles, there is no other way CRSs can be installed differently. Correspondingly, the need for a supplemental device, to reduce human effort during installation, could play a significant role in reducing the CRSs installation errors and thus mitigate misuse and increase child safety in vehicles.

In this research, computer aided engineering (CAE), manufacturing, and physical testing was conducted to develop a Child Restraint System Installation Aid Device (CRSIAD) for the purpose of mitigating CRS installation errors. The main focus of this research can be summarized in the following points:

1. To study and build a material model that is suitable to be used for developing the CRSIAD. Standardized material mechanical

characterization is needed to assess the performance of lightweight wood materials, for data needed in the generation of an anisotropic material model. The developed material model will be validated to the experimental data using a suitable quantitative means of model validation.

2. To design a CRSIAD mechanism that will preload the CRS into the car seat, thus reducing the physical effort for installing the CRS and potentially mitigating misuse.

3. To construct the CRSIAD geometry based on given CRS geometry and spatial constraints developed from the surveying of existing CRS products among major suppliers in the market. Following the creation of such CAD data a full FEA model of the CRSIAD will be developed and also incorporate the material model developed in item (1) above. Simulation of the CRS installation loading conditions for both forward-facing and rearward-facing configurations will also be considered. The appropriate geometry design iterations will be performed, using FEA, until the loading stress level is within the yield limit of the material and a lightweight design is achieved.

4. To fabricate the CRSIAD according to the CAE efforts identified in item (3) above. Following the manufacturing, the device will be tested in a number of popular production vehicles. Design iterations will be completed to ensure appropriate performance and ease of use.

5. To obtain user satisfaction input for further design enhancement of the CRSIAD. A comparison of CRS installation ease, with and without the use of the CRSIAD, will also be considered.

4. CRSIAD GEOMETRY DESIGN

4.1 In-car Concept Model Development

To initiate the design for the CRSIAD, it was helpful to start with developing a mock-up system that can achieve preloading of the CRS into a vehicle. The goal was to build such a system with attainable parts from hardware stores.

4.1.1 Loading Mechanism

A readily available loading device is necessary for the system to apply load on the CRS. A suitable product for load application was discovered to be a car scissor jack after exhaustive examination of viable alternatives as shown in Figure 10 in Section 4.2.1. It is designed to support and raise in a quasi-static fashion approximately one-quarter of the weight of a car so that the loading capacity was assumed to be more than sufficient.

4.1.2 Restraining Components

In order to operate in a manner necessary to load the CRS into the vehicle seat, the top end of the scissor jack needed to be constrained so the loading device would apply a counter-force towards the CRS. The seatbelt on the vehicle was found to be the ideal component to restrain the top of the scissor jack. However, the lap belt and shoulder belt counter-react with each other. For example, when the lap belt is being pulled and extended, the shoulder belt retracts because they are on the same belt loop. This feature is by design and allows passengers to adjust the belt according to their body sizes. Therefore, this flexibility will not suitably restrain the top of the jack in a method needed to load the CRS into the vehicle seat.

The solution here was to utilize an H-clip to appropriately apply a kinematic constraint to the seatbelt. An H-clip is readily available on every CRS product in the

market as people who install CRS with car seatbelts are encouraged to use the clip for restraining purposes [3]. Utilizing the H-clip between the lap belt and shoulder belt together results in no counter movement between the two as illustrated in Figure 9. Therefore with the addition of an H-clip, even when the jack was pushing up against the lap belt, the entire seatbelt system remained stationary so that the top of the jack was kinematically constrained.

A **B**

Figure 9. Seatbelt with adjustable webbing (A) and with H-clip (B).

4.2 In-car Concept Model Testing

A feasible concept model was developed with trial-and-error approach for initiating further design process.

4.2.1 Test Setup

The mock-up system is shown in Figure 10. The top of the scissor jack was aligned with the lap belt for a most appropriate loading condition. With the limited space in a car, the original crank handle could not be used due to volume constraints. Correspondingly, the scissor jack was operated by hand instead of the crank handle.

With the lap belt restraining the top of the scissor jack, the scissor jack was expected to push the CRS downwards while being actuated.

Figure 10. Simple scissor jack concept device installed on a CRS.

4.2.2 Test Results

The pilot testing was discovered to be a success for the purpose of preloading. The system was able to preload the CRS into the car seat deep enough so that lower anchor straps could be tightened by hand to complete the CRS installation process. However, there were some areas for improvement that were valuable for further design consideration of the CRSIAD.

The actuation of the scissor jack was very slow which may potentially frustrate the installer as a result of the significant time needed to suitably load the system. The scissor jack was not designed to operate quickly as it may create a kinematic instability (i.e. tip over) when jacking up a car. Therefore, many rotations of cranking were required in this case to preload the CRS to a tight state. It was observed that this characteristic was not user friendly.

Seating of the scissor jack on the CRS was not ideal as a result of surface contour differences between the bottom side of the jack, which exhibits a flat surface, and the seating surface of CRS, which has a curved contour. When the jack was being actuated the alignment of the system was disturbed and was not necessarily ideal. The moving direction of the jack and the supporting direction of the lap belt are not parallel so there was potential for them to separate during the operation.

4.2.3 Recommendations for Designing CRSIAD

The scissor jack configuration served its purpose as a design concept but also exposed issues that need to be resolved during the design phase. The identified issues are listed and discussed as following.

The CRSIAD would need to be operated within a reasonably short time to achieve the preloading process. The issue of slow speed would not affect mechanical performance but rather the user's patience. It is important to maintain enthusiasm of using the CRSIAD so that people who have used it would likely use it again or introduce it to others.

The device would need to be properly seated and aligned in a CRS throughout the entire loading process. The mismatched shape of the scissor jack created issues of alignment which made the preloading process inefficient. This will require the bottom surface of the CRSIAD to appropriately match the contour of the seating surface of CRS. With properly-matched contacting surfaces between the CRSIAD and CRS, maximum efficiency of loading can be achieved. Potential contact with other parts of the CRS should be avoided. Preloading should be concentrated only on the proper contact area to achieve good efficiency. Contact with the side frame of the CRS during operation could also cause misalignment.

Any potential alignment issue or oblique loading condition would need to be addressed. The CRSIAD should have a proper restraint system so that the force

acting on the CRS will be directed to a most effective angle. In this case, the loading direction should directly point to the lower anchors in the car seat, which would effectively create slack in the lower anchor webbing on CRS so that it could be tightened by hand to complete the installation process.

The device should be easy to operate. Using the scissor jack setup was tricky due to the issues above, which could cause confusion for the users. The main purpose of designing CRSIAD is to mitigate misuse. Any confusion of using the CRSIAD could cause new misuse that would defeat the purpose of this project. The CRSIAD should be designed to be used in a reasonably self-explanatory way and also be user-friendly.

4.3 Geometric Constraints

Before designing the geometry of the CRSIAD, it was important to understand the volume that the device could be used within. The geometry of the device would need to correlate with the interior of the vehicle as well as the geometry of the CRS.

4.3.1 Defining the Geometric Constraints For Key Dimensions

The geometric constraints of the CRSIAD are highly dependent on the dimensions of the CRS. To determine such a volume, the geometry of over 30 existing CRS products was examined to measure existing CRSs from major suppliers in the market. These stores included Toys'R'Us, Walmart and Canadian Tire. Survey data for all the critical dimensions are available in Table 1 in Section Appendix A. The geometric constraints were then developed from the surveyed data. Since the CRSIAD would be applied on the seating surface of the CRS, only dimensions in the vicinity of this region would be considered in the development of the geometric constraints.

The inner width of the seating area (the dimension "A" in Figure 11) is critical because the CRSIAD will be located at this region. The width of the CRSIAD must not be narrower than the inner width of a CRS. The minimum inner width of CRS was to be measured and recorded on the survey.

Figure 11. Model name Baby Trend Flex Loc Infant Seat with inner width (the red dimension "A") and outer width (the blue dimension "B").

The CRSIAD would be made of a material that does not flex in any directions in order to support sufficient amount of load to preload the CRS. However, a rigid device may damage the fabric of CRS during the preloading process. If the width of the device is narrower than the inner width of the CRS a more suitable protective environment for the fabric would result. However, this particular width should not be too small to avoid any compromise in the stability of the CRSIAD. Referring to Table 1 in Appendix A, the smallest minimum inner width among all surveyed CRSs (the dimension "A" in Figure 11) is 215.9mm. The seating width of the CRSIAD was then determined to be 190.5mm as a starting point, allowing for approximately 13 mm clearance on each side.

The outer width of the CRS (the dimension "B" in Figure 11) was important for the design of the width for the CRSIAD. The width of the CRSIAD must be greater than the width of the CRS in order for the CRSIAD to be appropriately anchored to the vehicle without potential contact with the CRS. The outer width of the CRS was the distance measured from widest points of the CRS including accessories such as cup holders and armrests. The greatest surveyed value for outer width of CRS was measured to be 510.54 mm as shown in Table 18 in Section Appendix A. Minimum or average values of this dimension are not important since the width of the CRSIAD only needs to overcome the largest measured width of the CRS among all surveyed CRSs.

With the width limits obtained, it was necessary to determine the limitations on the vertical plane (CRS side view plane as shown in figure 12). Due to the variations among the CRS models in the market, a series of critical locations, which may affect the geometry design of the CRSIAD as well as its functionality, had to be defined.

Due to the variations among the CRS models in the market, critical points were selected to limit the side profile of the CRSIAD. Figure 12 presents a typical forward facing configuration when the CRS is installed in the car. Point O is the virtual lower anchor points in the vehicle seat as observed in a side view. Typically this point is located slightly to the lower right of the intersection of the two red lines in Figure 12 because the lower anchor bars are installed in the crevasse of the vehicle seat. Such discrepancy is so small that it was neglected in the design of the CRSIAD geometry. Therefore, Point O was conveniently defined as the origin in this configuration in the x/y coordinate axes. Point 2 is the highest point of the bottom side wings of the CRS and Point 1 is the left-most point of the bolster side wings in the side view. Point 1 and Point 2 were considered as the peak points of the two wing sections.

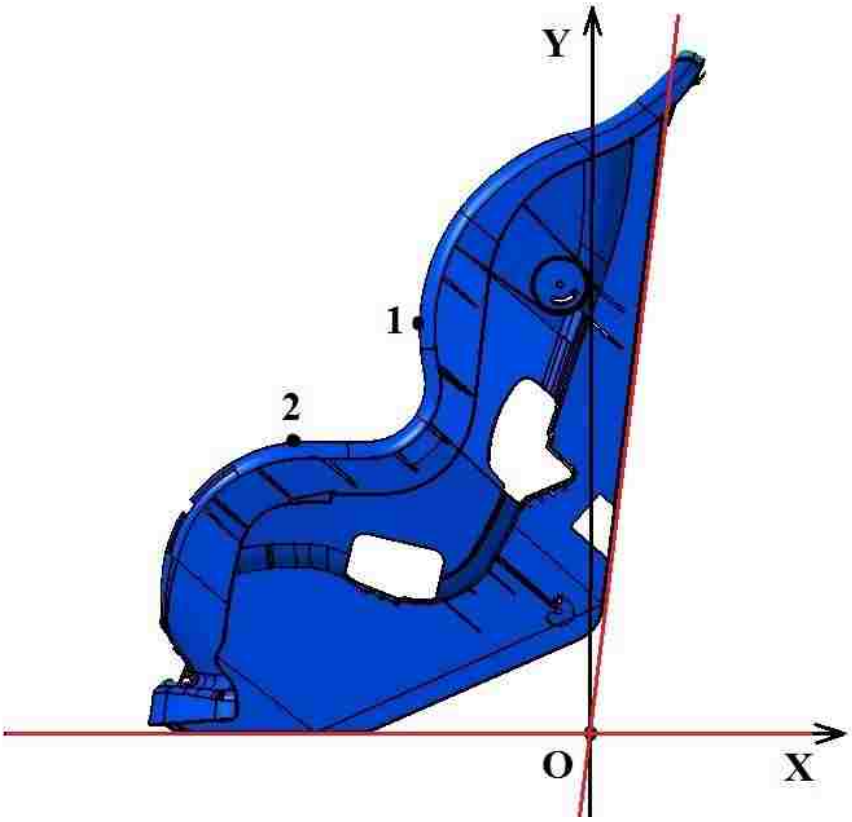

Figure 12. Side View of CRS with Local Coordinate System for Defining Critical Points.

Points 1 and 2 were identified and located on all the surveyed CRSs and their coordinates were defined based on the origin (Point 3). These two x and y coordinates were considered as boundaries in this plane for the CRSIAD. The purpose of this was to make sure any part of CRSIAD that is extended to the outside of CRS side wings would not have potential contact with the side wings, meaning such portion of the CRSIAD should stay to the left of Point 1 and above the top of Point 2 as presented in the side view of the CRS in Figure 12.

4.3.2 Measurement Process

A measuring tape was used to measure the widths of all the surveyed CRSs. Five measurements were done on each dimension and average value was recorded.

The method of identifying the origin, Point O, was mentioned previously in section 4.3.1. Inner and Outer widths from Figure 12 were measured easily with measuring tape. Points 1 and 2 were measured based on the origin (Point O) in the x/y coordinate axes. With the coordinates of Points 1 and 2 obtained, a typical CRS side design envelop was established as shown as the green zone in Figure 13 (A).

Some surveyed CRSs had accessories on the sides such as an armrest or cup holder. In such cases, measurement was simplified shown in Figure 13 (B). Only one point (Point A) was needed to replace both Points 1 and 2 from Figure 14 because Point A is both the highest point of lower wing (due to added armrest) and the left most point of side wing. All recorded coordinates are available in Table 18 in Appendix A.

A **B**

Figure 13. Sample CRSs (A: Graco Comfort Convertible with no accessory; B: Eddie Bauer Alpha Elite with armrest) to demonstrate design envelop measurement (green zone).

4.4 Concept Model Geometry Generation

The previously developed scissor jack system was used as a starting concept for creating the geometry of the CRSIAD. Although only a mock-up, this system was helpful in identifying issues and constraints for further developing the shape of the CRSIAD. Therefore, the design process of CRSIAD commenced with resolving problems from Section 4.2.4 combined with the geometrical constraints from the developed space envelop presented Section 4.3.2.

4.4.1 Main Frame Shaping

The contact section at the base and back of the CRSIAD needed to match closely with existing CRS geometry to avoid any misalignment or load concentration issues.

Existing CAD data of CRS geometry, namely a Graco Convertible CRS was used to create the bottom section of the CRSIAD so that the bottom profile was appropriately aligned. The seating sections for the majority of CRSs in the market were found to be very similar in shape. This was advantageous to the design of the CRSIAD geometry as the CRSIAD would have to fit universally to all CRSs.

Figure 14 shows a representative entity (Entity "A") designed to sit on top of the given CRS geometry (Entity "B"). The bottom section of Entity "A" closely matched the seating area of Entity "B" with the contact section marked in red in Figure 14.

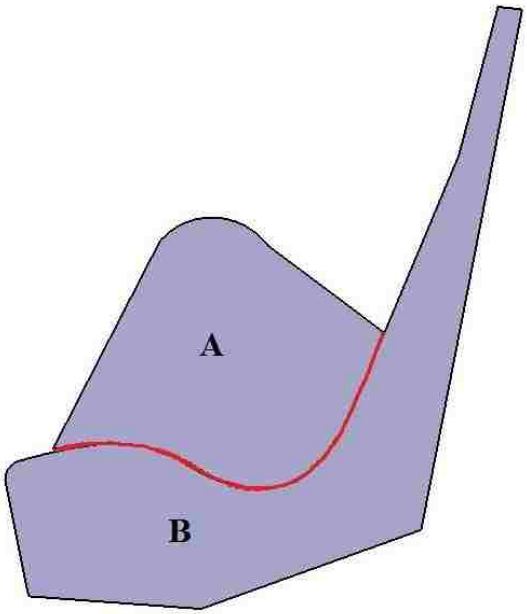

Figure 14. The CRSIAD representative entity A with closely matched bottom profile (red mark) to the given CRS geometry B.

The matched contact surfacing allows the load to be distributed evenly which ensures stability during the preloading process. With the bottom profile of the CRSIAD aligning to the CRS, the potential for the CRSIAD to damage fabric of CRS during the operation was also minimized.

4.4.2 Main Loading Mechanism

The preloading time of the CRSIAD should be controlled within ten seconds for the convenience of the users. Therefore, a fast and convenient mechanism should be adapted in the design to ensure enthusiasm of the installers for using the CRSIAD.

A ratchet strap assembly was chosen as the main loading mechanism after exhaustive examination of feasible alternatives in the market such as electric-powered and pneumatic devices. Installing an electric gearbox for the application of

the CRSIAD requires a motor with sufficient torque to support the loading weight equivalent to a human body. Such a motor is typically heavy and rated at higher voltage than 12 Volts that a normal vehicle can supply. Searching for a suitable pneumatic device was also unsuccessful due to size and packaging limitations during the time of searching. A ratchet strap assembly is robust, compact and readily available in the stores. When properly used, the ratchet strap can appropriately preload with minimal rotation, motion and effort. Car seatbelt webbing was first chosen for the ratchet strap assembly due to its safe loading capacity for passengers. A 1500 lb ratchet was then selected to match the width of the seatbelt webbing which is 50.8 mm.

At this point, the geometric constraints developed previously in Section 4.3.2 must be used for developing the top CRSIAD geometry. The loading points of the ratchet webbing must be located within the "design zone" in Figure 15 to avoid any contact between itself and the CRS body.

4.4.3 Loading Structure

With a ratchet strap loading assembly, the need for a loading beam was identified to allow the strap webbing to run across the CRSIAD in order to appropriately preload, on both sides of the installation aid, the CRS within the vehicle seat. Loading points at the straps had to be properly located on the loading structure so the force would be acting onto the system properly. The width of the loading beam has to be wider than the greatest surveyed CRS outer width value (Section 4.3.1) which was determined to be 550 mm. The original loading beam concept is shown in Figure 15.

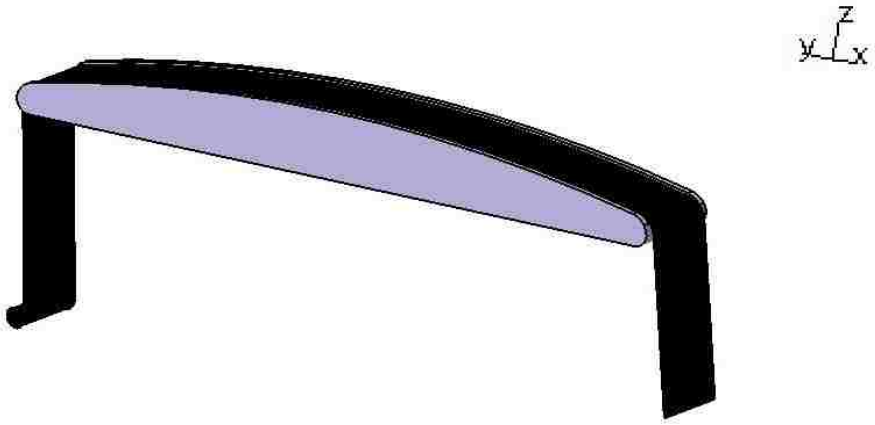

Figure 15. Original design of loading beam of the CRSIAD (black part is a dummy strap that runs across).

This design concept was reasonable and a curved surface ensures even distribution of the load from the webbing. However, the surface contact area between the webbing and beam was predicted to be quite significant in this case. The strap would move in one direction when it was being operated by the ratchet, which would create lateral frictional load on the beam surface. The large amount of friction would compromise stability of the system and potentially tilt the entire system to one side. Such issue needed to be addressed and therefore the beam needed to have as little amount of contact area with the strap as possible while maintaining functionality of the webbing.

Seatbelt D-rings from production vehicles were used for minimizing belt friction in the seatbelt system. They are ready-made and tested for production vehicles with minimum friction and safe for loading. They were to be mounted on each end of the beam so that the webbing can run through them. The updated loading beam design is shown in Figure 16.

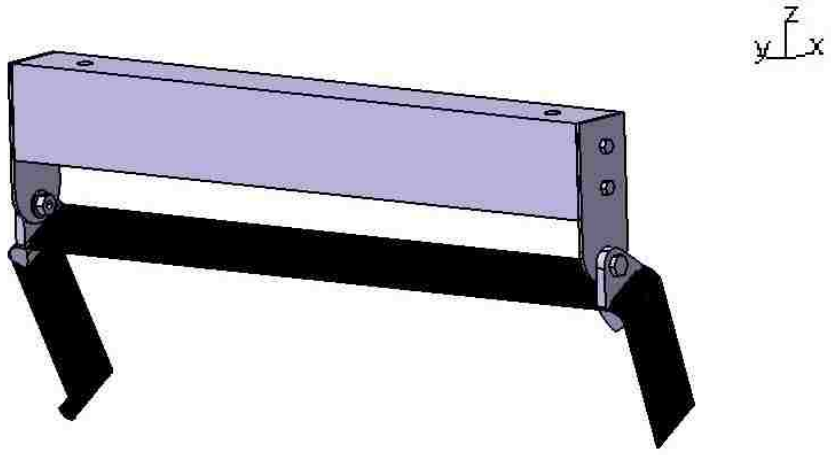

Figure 16. Loading beam design with attached D-rings.

4.4.4 The CRSIAD Restraint System

There is one missing component in the system that plays an important role for the CRSIAD, namely, the restraint system. The foundation of the CRSIAD structure had been established, which consist of a main CRSIAD frame, loading beam and ratchet strap assembly. However, this concept would not work without having the ratchet strap ends being attached to fixed points in order for the system to operate.

From the scissor jack concept model (Section 4.2.3), it was concluded that the loading direction of the CRSIAD should ideally be pointing towards the lower anchor points which will coincide with the loading direction of the LATCH webbing. Existing car seatbelt system was found to be useful during the scissor jack concept testing and would be feasible for CRSIAD.

Seatbelt systems on passenger vehicles are all standardized – one male clip on one side of the seat and one female buckle on the other side. The female buckle is a fixed end where as the male end is adjustable in length for passenger's safety and

comfort. Due to the requirement that both ends need to be fixed for the purpose of restraint, the flexible end (either male or female) would need to be a fixed end. As discussed in Section 4.1.4, an H-clip can be implemented to the extendable end to prevent relative motion between belts.

With all components mentioned above combined, a concept restraint system was designed to serve the loading structure to the CRSIAD as shown in Figure 17. A ratchet is attached to the left side of loading beam with the end attachment being male seatbelt clip; the Female buckle is attached to the webbing located on the right side. Although the design seemed to be feasible, each component needed to be carefully considered and engineered to meet all design specifications. The loading beam would need to be designed to a specific width as mentioned in Section 4.4.3 and built from a suitable material. D-rings and ratchet straps are off-the-shelf products but needed to be carefully selected. Sizing of the webbing and loading capacity had to be considered for the specific CRSIAD application. All the seatbelt clips and buckles needed to fit in majority of production vehicles in the market.

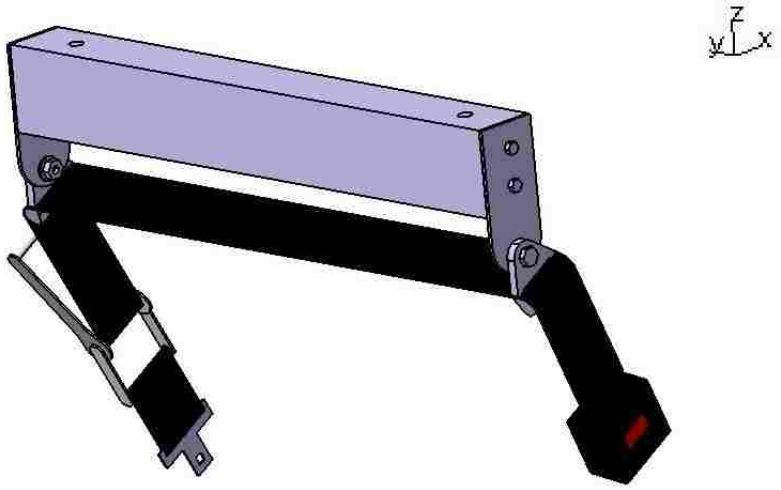

Figure 17. Complete loading structure of the CRSIAD with clip and buckle attachments.

4.4.5 Complete Assembly Geometry

Combing the design of the above three components, a concept restraint system, presented in Figure 18, was developed to serve as the loading structure of the CRSIAD.

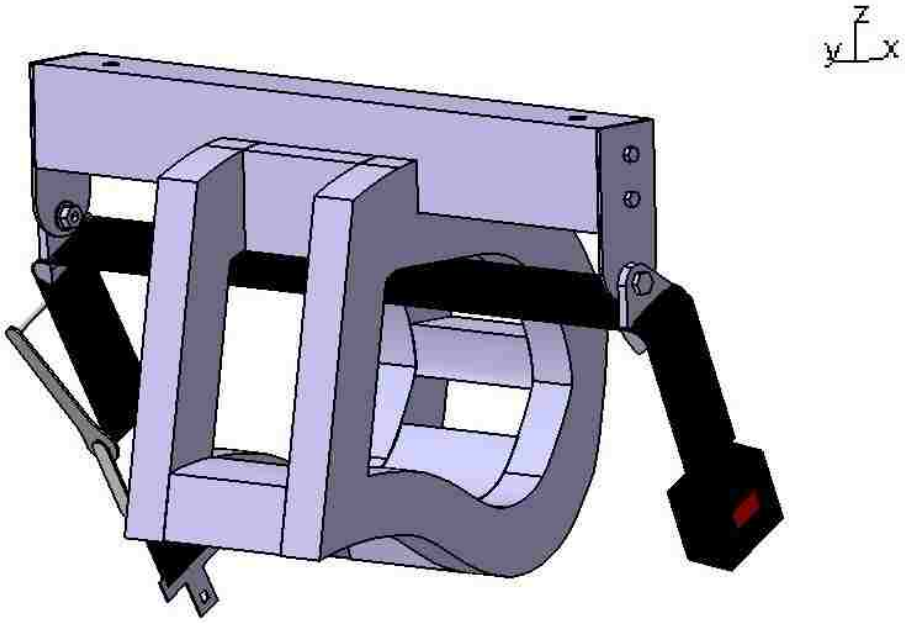

Figure 18. Complete concept CAD model of the CRSIAD.

5. MATERIAL TESTING

5.1 Material Introduction

Several major factors were considered when picking the material for the CRSIAD with a sufficient strength to weight level being the top priority. The CRSIAD was expected to sustain loads equivalent to the weight of a human body because the preloading process of CRSIAD was to replace the weight of the installer. In addition, a lightweight material is preferred due to the need for users to handle such a device often. The material also needed to be relatively rigid because any flex in the system reduce the efficiency of preloading.

Some feasible and commonly used materials were assessed as candidates shown in Table 2 below.

	Density (kg/m^3)	Elastic Modulus (GPa)	Yield Strength (MPa)
Stainless Steel	7750	207	520
Aluminum	2768	73	400
Plywood (Tested)	677	9.8	17.6
ABS Plastic	1000	2.3	N/A
Pine Wood	510	9	15.8

Table 3. Comparison of commonly used materials [18].

Stainless steel has the highest density among the listed materials. As mentioned previously CRSIAD is required to be lightweight so that it can be carried in and out of the car with reasonable physical effort. Weight of steel would become a burden for female users so this material would not be adapted. Aluminum is lightweight and strong. However, such level of strength is not necessary for light loading application as in a CRS installation. Yet, the density of aluminum is still five times

greater than wood. Market pricing of aluminum sheets is also more than twice as much as wood [19]. ABS plastic is lightweight but low elastic modulus value indicates excessive flexibility in the material. As previously mentioned, rigidity is required for CRSIAD to efficiently preload CRS and flex would become a problem. On top of that, ABS plastic is complicated to work with during manufacturing phase.

Plywood is made by laminating wood in thin layers (3mm each ply), which achieves high strength with light weight compared to metal materials [17]. It was chosen to be the main material to construct the frame of the CRSIAD. As an example, in ASTM Standard D143 - 94 [20], pine wood presents good strength, weight and hardness. Although yield strength is significantly lower than metal materials in Table 2, it was considered as good candidate for such light loading application.

A suitable material model is vital for performing FEA analysis for the CRSIAD. Plywood is an upgraded version of conventional sheet wood and is widely used in household and construction applications. It presents good strength, weight, hardness and low cost. Compared to conventional wood sheets, its strength is consistent across all directions of the panel. Its multiple (odd number) plies prevent warping and provide improved rigidity compared to other conventional wood sheets [21].

Therefore, plywood was chosen over pine wood due to all its advantages. The material properties were tested in the lab and carefully examined during simulation phase. The material model was also verified with simulation and validated with findings from real testing.

5.1.1 Background

This study is about creating and validating a suitable material model for plywood, which will be used for the CRSIAD device. Given the nature of plywood,

an anisotropic material model was used in modeling this material plywood and its mechanical material behaviour under loading. Due to the nature of the problem to be studied, LS-DYNA was selected as the finite element solver for CAE studies. A material model applicable to wood, namely, *MAT_143 (MAT_WOOD), was chosen to simulate the plywood for its ability to model orthotropic wood materials. This model is also applicable for all varieties of wood when appropriate material parameters are selected [22].

5.1.2 Material Model Theory

MAT_WOOD consists of five main sections, namely stiffness, strength, hardening, damage and rate effect, which contain key parameters and are listed below in the complete material model list.

As wood is an orthotropic material, elastic modulus may vary in different wood orientations so and correspondingly this model contains four elastic modulii to describe the elastic material behaviors. Therefore, the stiffness section of the material model contains the following four parameters: E_L (Parallel Elastic Modulus), E_T (Perpendicular Elastic Modulus), G_{LT} (Parallel Shear Modulus) and G_{LR} (Perpendicular Shear Modulus). These parameters were determined directly from experimental results from each test event.

The strength contains the following parameters, X_T (Parallel Wood Tensile Strength), X_C (Parallel Wood Compression Strength), Y_T (Perpendicular Wood Tensile Strength), Y_C (Perpendicular Wood Compression Strength), $S\|$ (Parallel Shear Strength) and $S\perp$ (Perpendicular Shear Strength), for assessment of strength characteristics in all directions to the wood fibre. Similar to the elastic moduli, these parameters were obtained through an examination and data contained in the experimental stress/strain material response from laboratory tests. Aspects of material hardening, which describes the pre-peak plastic deformation characteristics of the material, were incorporated into this material model using the following

parameters: $N_{\parallel}$ (Parallel Hardening Initiation Parameter), $N_{\perp}$ (Perpendicular Hardening Initiation Parameter), $c_{\parallel}$ (Parallel Hardening Rate) and $c_{\perp}$ (Perpendicular Hardening Rate). These hardening parameters were derived from the nonlinear portion of compressive stress/strain material responses measured in both parallel and perpendicular directions to the wood fibre.

The material damage describes the characteristics of plastic deformation after the ultimate strength, which in the loading curve starts from ultimate stress to failure point. The parameters in this module, *B* (Parallel Softening Parameter) and *D* (Perpendicular Softening Parameter), are only available for tensile and shear test conditions.

Although the material model incorporates the possibility of involving material rate effect this aspect was not incorporated into the specific application here as the CRSIAD will not to be subjected to any form of high rate loading. Therefore, all rate effect parameters (η) were set to zero.

In addition to the five sections of the material model MAT_WOOD, wood orientation is required to be defined for each test simulation event. Each test specimen is different in wood orientation as it could be either parallel or perpendicular to fibre direction. MAT_WOOD (MAT 143) is specially designed to simulate orthotropic wood material so that such option is available. The material axes option (AOPT) enables orientation definition ability through a locally defined coordinate system to specify vectors for directions parallel and perpendicular to the wood fibre.

MAT_WOOD is constructed by the formulations shown in the flow chart below in Figure 19 [22].

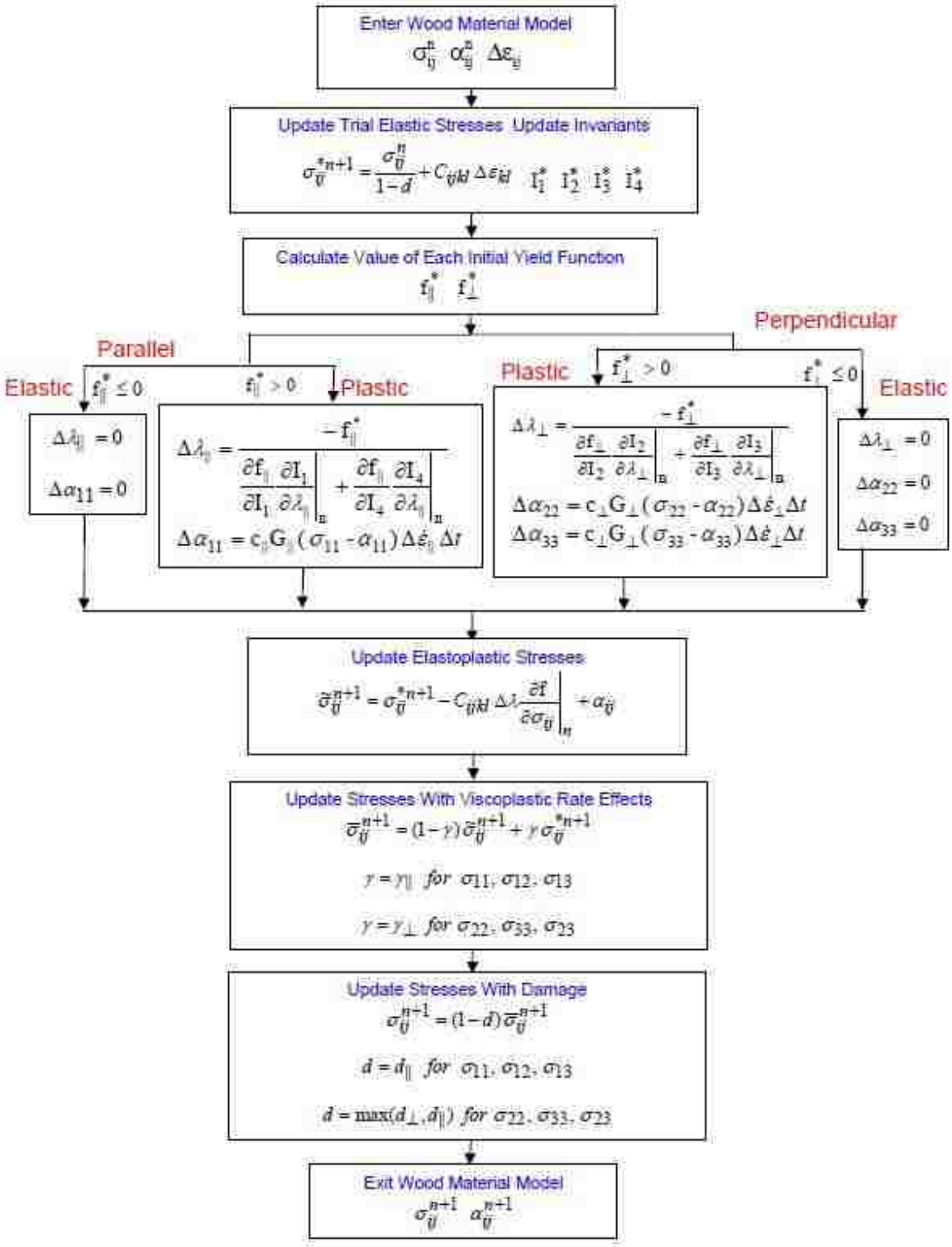

Figure 19. MAT_WOOD material model formulation flow chart [22].

5.2 Material Testing Methodology

5.2.1 Scope of Material Testing

Six primary tests were completed for all orientations of the plywood sheet in order to collect parameters for the material model, namely, tensile and compression tests in the fibre parallel direction, tensile and compression tests perpendicular to the fibre directions, and shear tests in directions both parallel and perpendicular to the fibre. Three-point bending tests were conducted to validate the material model.

Specimens were first fabricated according to each specific test as per ASTM Standard D143-94 [20]. Each testing event was then conducted using an MTS tensile test machine. Load, displacement and stress data was acquired from the tensile test machine controller where as strain data was recorded by using an external video-extensometer. All equipment are described in Section 5.2.3.

Eight test iterations for each testing event were completed to generate load, displacement, stress and strain data. The collected data was imported into SigmaPlot consistently with a resolution of 0.1 second based on the testing. The plots with 80% or above convergence for each testing event were filtered for selecting the best-suited response plot. The response plot with the largest portion of convergence and least amount of anomalies was then selected as the best-suited response plot for its testing event.

Key material parameters such as yield strength, ultimate strength and failure strength were then acquired based on analyzing the representative stress/strain response for each test. Yield strength was determined by proportionality linear analysis, which is appropriate for small wood specimens [23]. Ultimate strength was identified as the peak point of stress-strain material response. Failure strength point was selected where the material showed sign of crack or dislocation during material testing.

5.2.2 Material Specimens:

To acquire the key parameters to construct the five main sections in the material model, good quality plywood sheets were purchased for material testing, namely a Baltic Birch 4 foot by 8 foot 3/4-inch plywood sheet from Miller's Millwork & Hardware located in Windsor, Ontario. All test specimens of this material were conducted according to specific wood testing ASTM standard D1037 - 99 [24]. Specimens were specifically fabricated in accordance to the relevant ASTM standard and all material specimen dimensions and specifications are available as drawings in Section Appendix B.

5.2.3 Test Equipment:

The MTS C45-305, having a load cell capacity of 150 kN, was chosen to conduct the tests within this investigation. The MTS C45-305, with a data acquisition rate of 1000 Hz and 20-bit resolution, was operated in conjunction with the MTS TestSuite TW Elite software on the test computer via USB 2.0 ports. Unique aspects of this testing machine, namely, the capability to test large specimens due to its large grip capability and high load capacity, made this machine choice for the following needed testing: the tensile testing in the parallel direction of the wood fibre, the tensile testing in the perpendicular direction of the wood fibre and the three-point bending testing.

The MTS C43-504, having a load cell capacity of 50kN, was chosen to conduct tests with small specimens due to its smaller grip crosshead such as the compression testing in the parallel direction of the wood fibre, the compression testing in the perpendicular direction of the wood fibre, the shear testing in the parallel direction of the wood fibre and the shear testing in the perpendicular direction of the wood fibre. The MTS C43-504 has identical data acquisition rate and resolution as the MTS C45-305 mentioned above, which are 1000 Hz and 20-bit, respectively. Despite the machine size and load capacity of the MTS C43-504 being smaller than

those of the MTS C45-305, the position resolution of the MTS C43-504 is in fact lower than that of the MTS C43-504, which is 0.00006mm in comparison to 0.000049mm, respectively. With the lowest testing rate among all testing being 2.5 mm/s, both position resolutions are high enough for all testing in the investigation. Testing software for the MTS 43-504 is MTS TestSuite TW Elite, which is also identical to the software used on MTS 45-305.

The Tinius Olsen Shear Test Apparatus (shown in Figure 27 in Section 5.3.5) was used for all shear testing in conjunction with the MTS C43-504. This apparatus was available in the test lab and consistent to the requirements described in ASTM standard D143-94 [20] specifically for shear testing.

The use of the MTS AVX04 Advantage Video-extensometer, as an aid to acquire strain data was also incorporated into the testing apparatus. The MTS AVX04 Advantage, with a frame rate of 17 fps and resolution of 1399×1038, was capable of calculating strain based on real-time image processing on the video-captured strain gauges on the specimen. Image setup and processing were accomplished on the program, namely, the MTS TestWorks installed on a separate computer that is connected to the AVX04 Advantage via a RJ45 Ethernet cable. The strain gauges were developed using dots on the specimen marked by hand in a specific pattern according to ASTM standard D143-94 [20] as shown in Figure 20. Dots were clearly marked by black marker on the clean and bright wood specimen surface with a diameter of 2 mm so that they can be clearly captured by the video camera. Adjacent dots are 12.7 mm apart in both horizontal and vertical directions. In the case of the compression testing in the parallel direction of the wood fibre, the horizontal dots were marked only 6.35 mm apart consecutively due to the width of the specimen. This video-extensometer setup was applied to the tensile testing in the parallel direction of the wood fibre and the compression parallel to the direction of wood fibre due to the sizes of the specimens being large enough for clear marking of strain gauge dots. For the setup of the tensile testing in the parallel direction of

the wood fibre, the labeled strain gauges in Figure 20 allowed the strains between gauge 1 to 5, 2 to 4 and 6 to 7 to be calculated in the MTS TestWorks. The application of the MTS AVX04 was also used in the calculation of Poisson's ratio of the material model.

Figure 20. Hand-marked strain gauge dots (1 to 7) for video extensometer capturing.

The MTS AVX04 Advantage was set up with the video camera fixed on a tri-pod and positioned to directly face the specimen as shown in Figure 21. For the clarity of the video-capturing process, the door of the MTS C43-504 was left open for the camera to be directly exposed to the specimen to perform video capturing.

Figure 21. Setup for AVX04 Advantage on a tri-pod with bright lighting.

Figure 22 (A) shows how the image was captured on the video-extensometer monitor on the MTS TestWorks. Numbered "Targets" were assigned to each of the strain gauges on the specimen for the controller to recognize the strain gauges in order to process and calculate data as shown in Figure 22 (B).

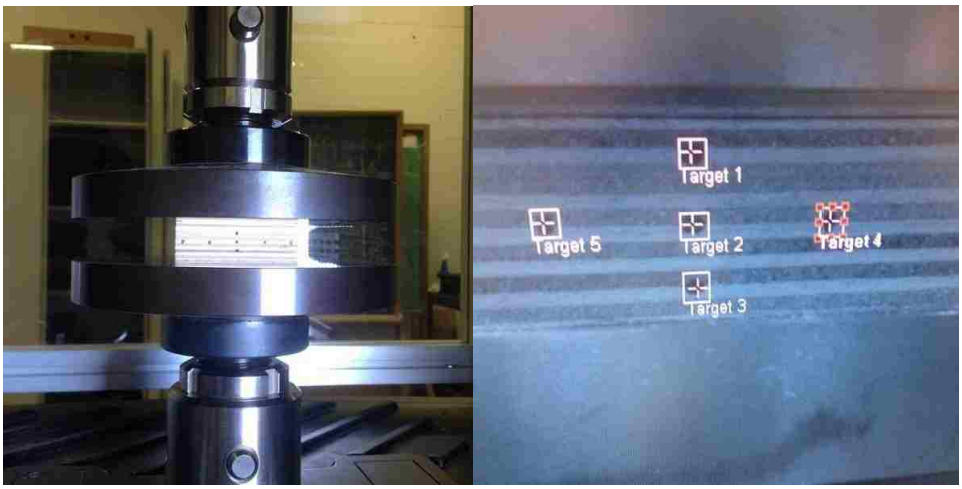

A **B**

Figure 22. Specimen with marked strain gauges (A) and captured strain gauges on the controller (B).

5.3 Test Setup

5.3.1 Tensile Testing In the Parallel Direction of the Wood Fibre

The test setup was completed in accordance to ASTM Standard D143-94 [20] as shown in Figure 23. The specimen was clamped between the crossheads on the MTS C45-305. The deformation was measured over a 50 mm central gage length of the specimen. The test commenced with a crosshead speed of 4 mm/min and automatically stopped when the specimen showed sign of separation or crack. Eight tests were performed for this configuration.

Figure 23. Tensile test setup in parallel to fibre direction with specimen placed in grip crosshead.

5.3.2 Tensile Testing In the Perpendicular Direction of the Wood Fibre

The specimen was clamped between crossheads as shown in Figure 24 in a similar configuration as the tensile test in the parallel direction of the wood fibre (Section 5.3.1). Eight tests were completed in this configuration. The nominal crosshead speed was 2.5 mm/min according to ASTM standards D143 - 94 [20].

Figure 24. Tensile test setup for the perpendicular to fibre direction configuration.

5.3.3 Compression Testing In the Parallel Direction of the Wood Fibre

Crosshead compression plates were installed on the MTS C43-504 for this testing configuration. Each specimen was placed between the crosshead plates and located centrally in the platens as presented in Figure 25. The bottom compression plate was fixed where as the top compression plate lowered and applied load to the specimen. The MTS AVX04 Advantage was used to acquire strain information. The specimen was carefully crafted and squared at end-faces to be perfectly aligned to the compression plates so that its parallelism to the loading direction was ensured.

Since the specimen was not clamped in place, the crosshead plates were manually adjusted to be as close to the specimen as possible. If there was a gap between specimen and plate, it could cause instability at the moment that the top plate touches the specimen. Such instantaneous instability could potentially cause alignment to go off and jeopardize the results through the rest of the test. Therefore,

a very small amount of preload (5N) was applied to the specimen by the top compression plate before the test started so that risk of misalignment was minimized. Such preload was achieved by manually lowering the top compression plate by the controller and until contact was achieved and a 5N preload was applied to the specimen.

The testing speed for this event was 0.12mm/min. Each test was terminated when material failure was detected which occurred automatically through the controller of the MTS C43-504.

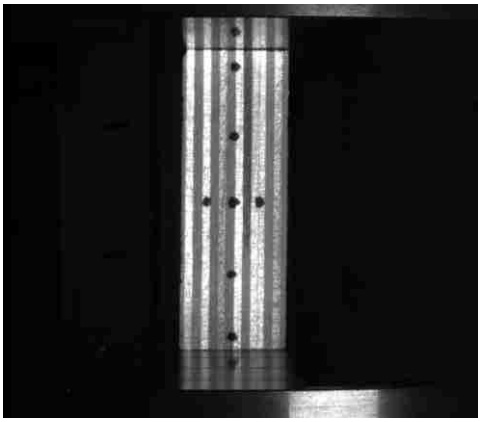

Figure 25. The specimen for the compression testing in the parallel direction of the wood fibre placed between the compression plates.

5.3.4 Compression Testing In the Perpendicular Direction of the Wood Fibre

Concept for this test is similar to the previous section (Section 5.3.3) except for two details, namely, the specimen was placed horizontally with its surface parallel to the lower crosshead plate instead of being parallel to it as shown in Figure 26; the top compression plate from the parallel configuration was replaced by a steel plate that was clamped on top grip crosshead. The plate was selected according to ASTM Standard D143-94 [20] based on its material and thickness.

Figure 26. Test setup for the compression testing in the perpendicular direction to the wood fibre.

The testing speed for this event was 0.305 mm/min. Due to the orientation of the specimen in this test, the ply on the top surface of the specimen will fail when the top steel plate reaches the displacement that is equal to the thickness of the ply. Therefore, this test event had to be manually terminated when the top ply of the specimen was failed.

5.3.5 Shear Testing In the Parallel Direction of the Wood Fibre

The setup of shear test is shown in Figure 27. The shear testing fixture, namely, Tinius Olsen Fixture was seated on the bottom compression plate of the MTS C45-305. The top sliding part of Tinius Olsen fixture was clamped at the top grip crosshead of the MTS C45-305. The specimen was placed in the shearing section of Tinius Olsen fixture as shown in Figure 27. Therefore, the upper grip crosshead of the MTS C45-305 controlled the movement of upper sliding part of Tinius Olsen fixture and was configured in compression mode. Due to the small size of the

specimen, namely 19.05 mm × 19.05 mm × 23.81 mm, only 5 N of preload was applied to the specimen to ensure secure seating of the specimen because a greater amount of preload may damage the specimen prematurely. However, such small amount of preload was insufficient to restrain all the allowance for the specimen to move. As a result, a short period of non-linear behaviour is present in the stress-strain response as the break-in period of loading the specimen.

Figure 27. The setup of the specimen on the Tinius Olsen Shear Test Apparatus.

The test testing speed of this test event was set to 0.61 mm/min according to ASTM Standard D143-94 [20]. The tests were terminated automatically when material failure was detected by the MTS C43-504, in which case the specimens failed in rapid motion.

5.3.6 Shear Testing In the Perpendicular Direction of the Wood Fibre

The set-up is identical to the previous section (Section 5.3.5) as shown in Figure 27 except for the difference on the wood fibre orientation of the specimen.

The testing speed of this testing event was also 0.61 mm/min. Test was terminated automatically when the specimen was failed.

5.3.7 Three-point Bending Testing

The MTS C45-305 is equipped with special adapters for the three-point bending testing as shown in Figure 28. Supportive cylinders were selected in recommended sizes according to ASTM Standard D1037-99 [24]. The upper loading cylinder was centered to the specimen and verified by measuring the distances from each end of the specimen to the midpoint of the specimen.

The testing speed for this test event was 9 mm/min. The specimen was loaded by the upper loading cylinder driven by the top crosshead of the MTS C45-305. The tests were terminated automatically when specimen failure was detected. Since the purpose of the three-point bending testing was to validate the material model, only the load and displacement data was required and collected. Therefore, no extensometer was used in this test event to generate strain data.

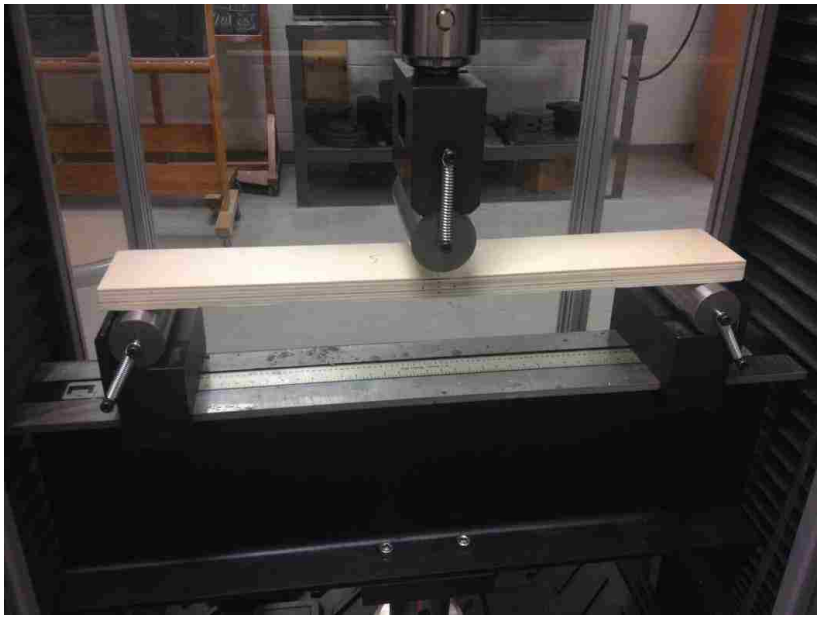

Figure 28. Test setup for three-point bending test.

6 Test Results

6.1 Experimental Data Processing

The representative stress-strain response for each testing event is presented for analysis purpose in the following sections. All eight response plots for each testing event are presented as raw data in Appendix B. The yield stress, derived by proportionality linear analysis as mentioned in Section 5.1.1, is marked as circle in all stress/strain response plots. The ultimate stress locations are marked as square in all stress/strain response plots. The linearity proportional line to determine yield strength is shown as a red straight line in all stress-strain response plots.

Noise on the stress-strain response plots for the tensile testing in the parallel direction of the wood fibre and the compression parallel to the direction of wood fibre was noted and caused by disturbance during video-capturing process of the MTS AVX04 Advantage. The processing on the image-based strain gauges was dependent on real time video-recording of the movement of the specimen. Any ambient light change or system vibration could cause image processing to generate an inappropriate measurement. Noise from the raw data was filtered by turning on the "Ignoring missing values" and "Ignoring out-of-range values" filters in SigmaPlot during the curve-plotting process to improve overall smoothness and readability of the curves. For some noisy portions of the response curve, averaging approach, namely, "Show Mean" was used to further reduce the noise. The noisy portions from low stress-level testing events (under 1 MPa) such as the shear testing were not filtered in order to maintain authenticity of the material response.

6.2 Tensile Testing In the Parallel Direction of the Wood Fibre

As mentioned in Section 6.1, a representative stress/strain response plot was selected and shown in Figure 29. The yield strength was identified to be 14.98 MPa. The plastic deformation occurred at the strain of 0.201% till the ultimate stress was

reached at 31.021 MPa at the strain of 0.619%. The material failure occurred right after the ultimate strength was reached.

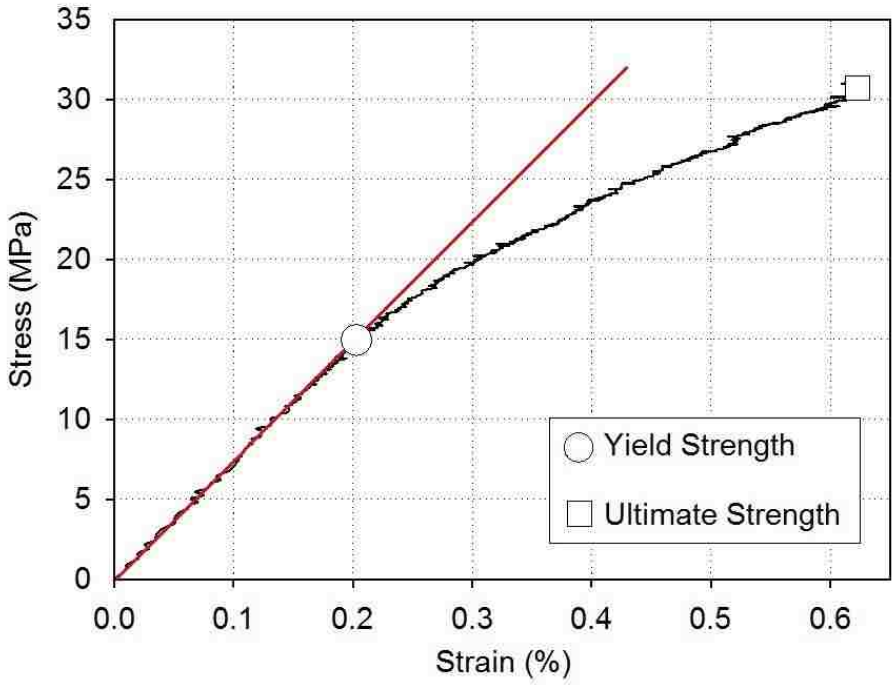

Figure 29. The representative stress versus strain response for the tensile test in the parallel direction of the wood fibre.

Poisson's ratio of the material was acquired from this testing event by calculating the average ratio of the vertical and horizontal strains from strain response data from the MTS TestWorks. The representative strain gauge data was sampled from the strain gauges "2" and "4" (vertical) and the strain gauges "6" and "7" (horizontal) from Figure 20 in Section 5.2.3. Due to the noise at the beginning of the response, the data from the first 4 seconds of the test was ignored in the calculation for the Poisson's ratio as shown in Figure 30. The average value of the Poisson's ratio was calculated to be 0.23.

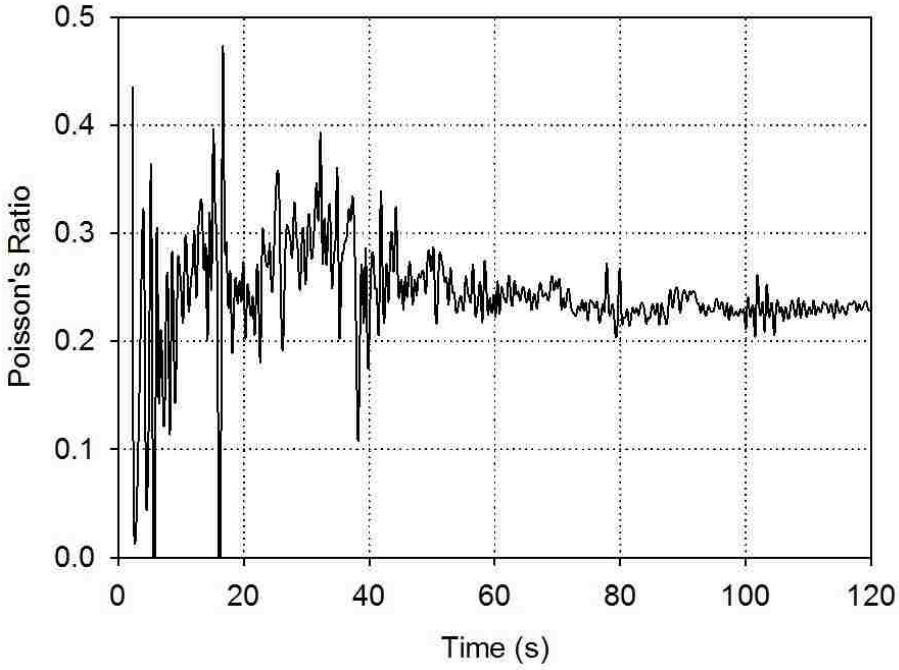

Figure 30. Poisson's ratio (horizontal strain/vertical strain) versus time.

6.3 Tensile Testing In the Perpendicular Direction of the Wood Fibre

In this testing event, the wood material was tested for its resistance to deformation in a direction perpendicular to the material fibres, which was associated with the strength the bonding layers (glue lines) of the specimen. However, specimens in this test all failed at location very close to the bonding layer but not at the bonding layer itself. Glue in the specimens was proven to be stronger than the material itself in the perpendicular direction of the wood fibre.

Stress-strain material response is presented in Figure 31. The yield strength and ultimate strength of this testing event were identified to be 0.127 MPa at the strain of 0.0012% and 0.201 MPa at the strain of 0.0029% respectively. The overall stress level in this testing event was low compared to the tensile test in the loading direction parallel to the wood fibre. The ultimate tensile strength occurred at 0.037 kN on the MTS 45-305 crosshead, which is low on the load cell range (0-150 kN).

As a result, fluctuation on the stress-strain response curve is present due to the resolution of the load cell. However, loading speed was set to as low as 2.5 mm/min throughout the test span in order to minimize the error due to low loading level.

The material showed more rigidity in its direction perpendicular to fibre orientation rather than in a direction parallel to the fibre. Failure occurred right after ultimate tensile strength was reached. The overall tensile strength is weaker and more brittle in its direction perpendicular to the wood fibre compared to the direction parallel to the wood fibre.

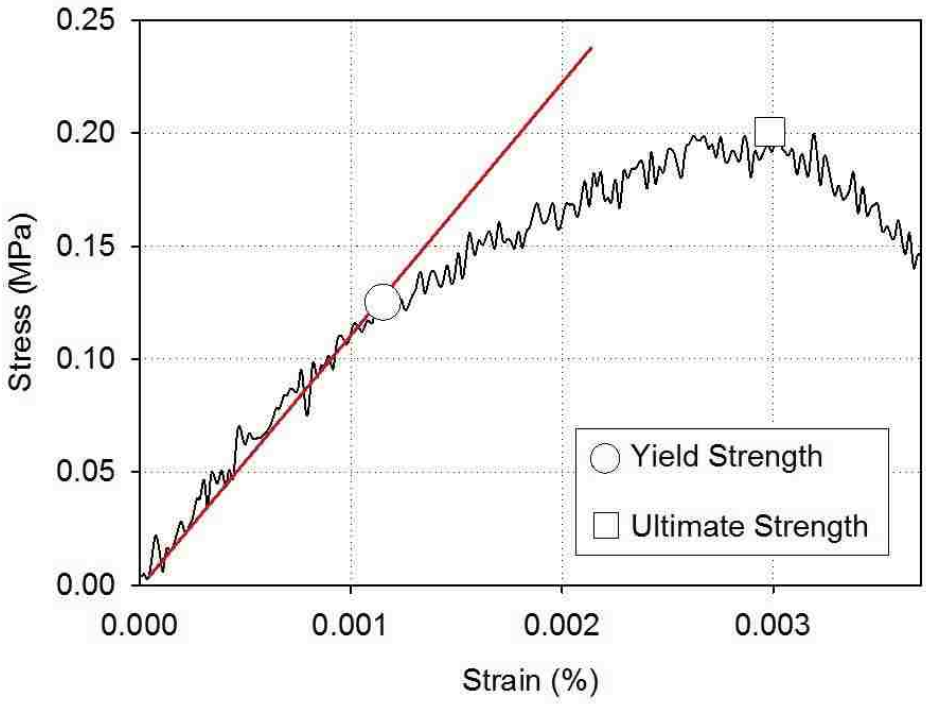

Figure 31. The representative stress versus strain response for the tensile test in the perpendicular direction of the wood fibre.

6.4 Compression Testing In the Parallel Direction of the Wood Fibre

The material showed a high strength level in this test as shown in Figure 32. The yield strength and ultimate strength in this testing event were identified to be

29.818 MPa at the strain of -0.39% and 46.001 MPa at the strain of -0.76% respectively. Due to the orientation of the specimen, material behavior under compression is very similar to the tensile test in parallel direction of the wood fibre such as the proportions of elastic and plastic regions. The major difference between tensile and compression tests in the parallel configuration is that stress level is higher in the compression test, which indicated the material is overall stronger under compression in its parallel fibre direction when compared to tensile loading.

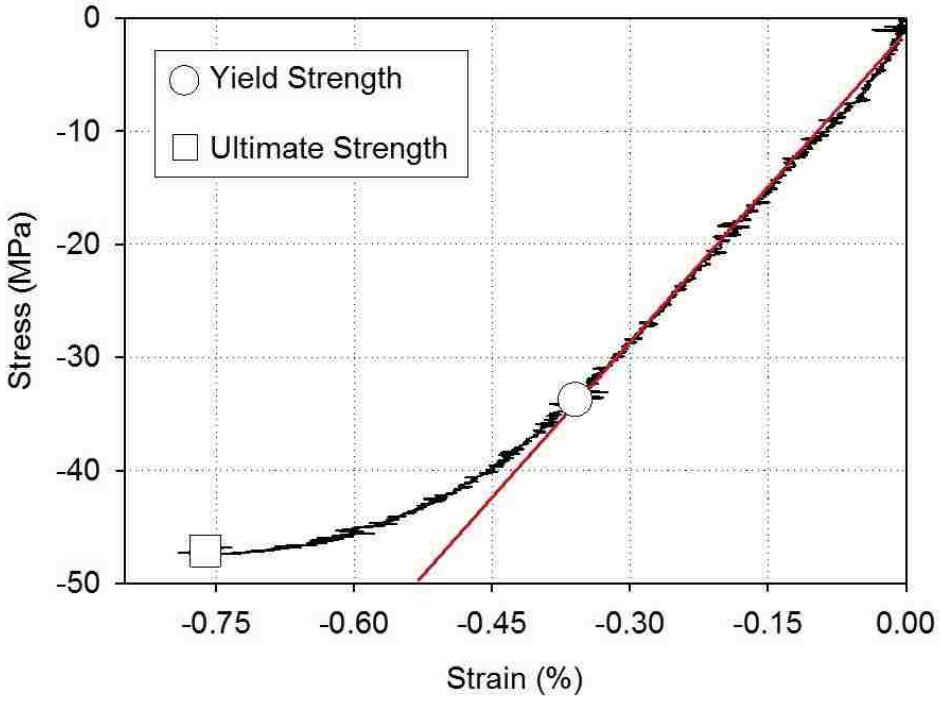

Figure 32. The representative stress versus strain response for the compression test in the parallel direction of the wood fibre.

6.5 Compression Testing In the Perpendicular Direction of the Wood Fibre

In the first two trials of test, it was observed that material would not reach fracture point within the full loading capacity of the MTS C43-504. As the specimen was being compressed, the thickness of compressed region became

thinner but the specimen showed no sign of crack. To address such issue and avoid damage to the testing equipment, the justification of the material failure point had to be changed for this test from observing the sign of first crack of the specimen to the sign of fracture at top ply of the specimen. From engineering point of view, this approach is realistic since failure of the out-most layer of the material can be considered as failure of the material. The failed specimen was shown in Section Appendix B that only the top layer was cracked and buckled.

The yield strength in this testing event was identified to be 11.546 MPa at the strain of -0.018% as shown in Figure 33. The pre-peak plastic deformation was more linear and long lasting before the ultimate compressive strength was reached. The material fracture occurred rapidly after the ultimate compressive strength at 22.501 MPa at the strain of -0.089%, which occurred at the top layer of the specimen.

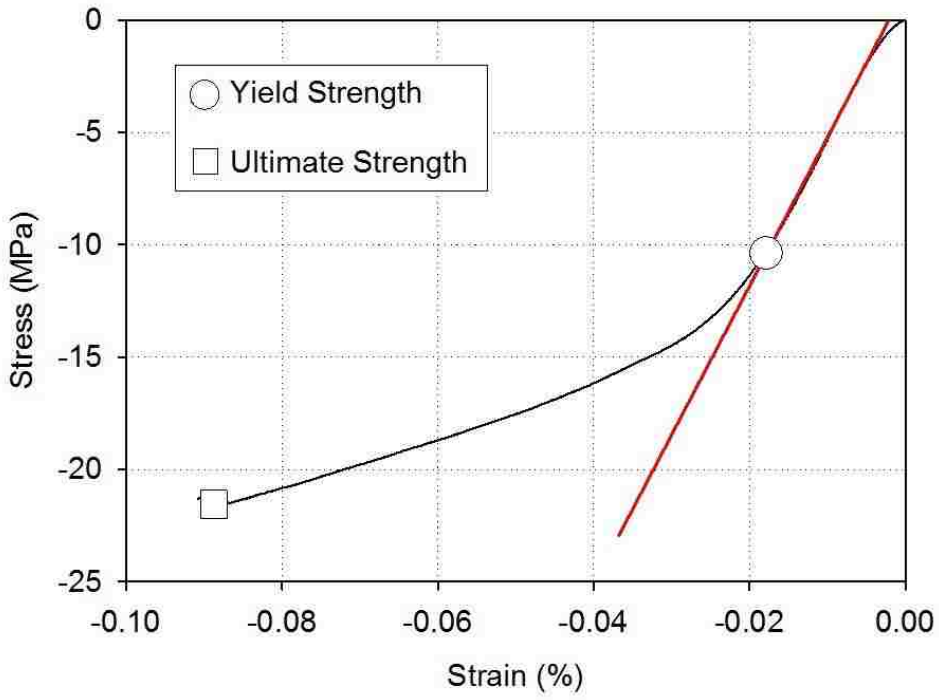

Figure 33. The representative stress versus strain response for the compression test in the perpendicular direction of the wood fibre.

6.6 Shear Testing In the Parallel Direction of the Wood Fibre

As expected, the specimens in this testing event all failed at their shear planes as shown in the failed specimen section in Section Appendix B. The yield strength of this testing event was identified to be 5.49 MPa at the strain of 0.03% as shown in Figure 34. The non-linear behaviour as mentioned in Section 5.3.5 is present in the strain range from 0 to 0.015%, which was excluded for identifying the yield point by linearity proportional analysis. The ultimate shear strength is 5.925 MPa at the strain of 0.037%.

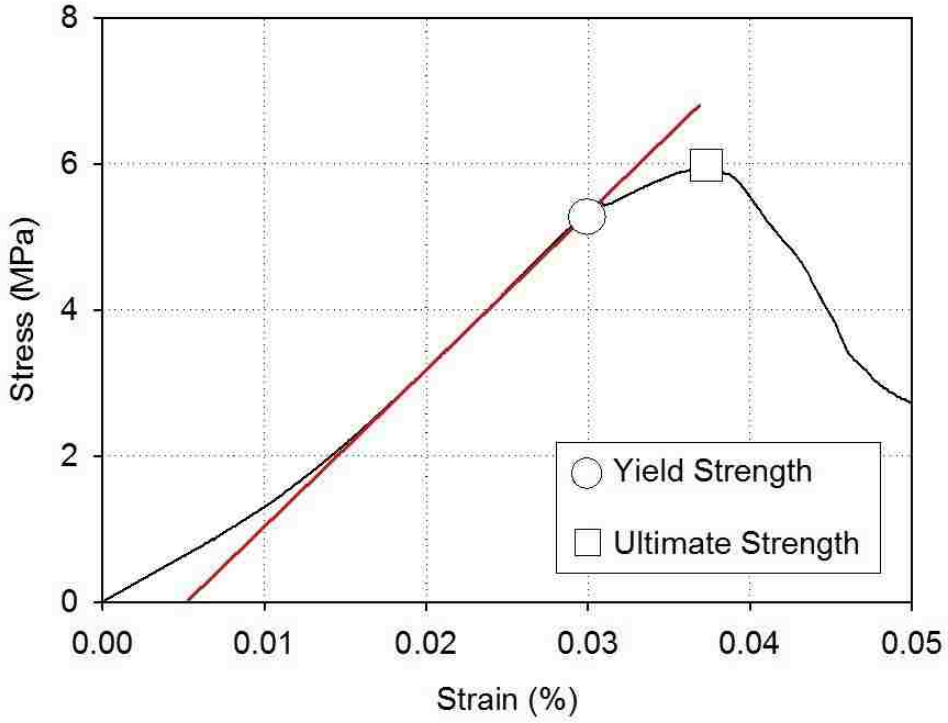

Figure 34. The representative stress versus strain response for the shear test in the parallel direction of the wood fibre.

6.7 Shear Testing In the Perpendicular Direction of the Wood Fibre

The material loading behaviour in the perpendicular direction of the wood fibre in Figure 35 was completely different from the testing in the parallel direction of the wood fibre even with the identical test setup. The material failure occurred right after ultimate shear strength was reached where as the post-peak plastic deformation last longer in the testing in the parallel direction of the wood fibre. It was indicative that material is more ductile in parallel orientation of the wood fibre than perpendicular orientation of the wood fibre under shear loading conditions. The yield strength and ultimate strength in this testing event were identified to be 3.137 MPa at the strain of 0.055% and 6.812 MPa at the strain of 0.172% respectively.

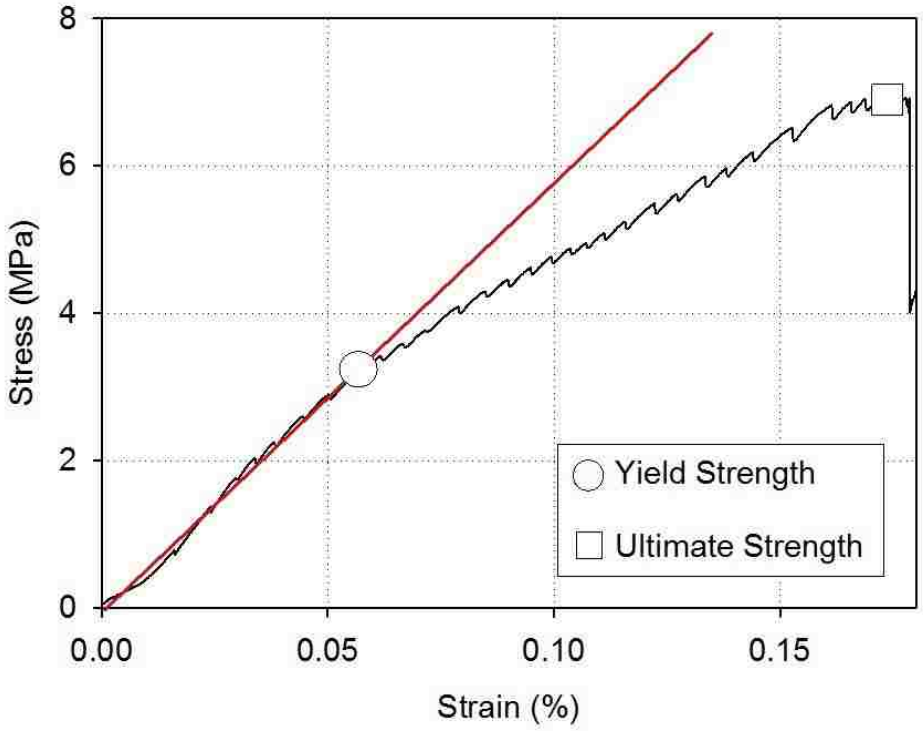

Figure 35. The representative stress versus strain response for the shear test in the perpendicular direction of the wood fibre.

6.8 Three-point Bending Testing

The load-displacement response plots of this testing event have showed good consistency with overall 90% of convergence as shown in Figure Q in Section Appendix C, which proved this test setup as an appropriate approach to quantitatively validate the testing results as recommended by ASTM Standard D143-94 [20]. The representative load-displacement response was chosen and shown as Figure 36.

The specimen failure occurred immediately after ultimate load was reached with minimum post-peak plastic deformation, which indicated the rigidity of the material that suits the preference for designing the CRSIAD.

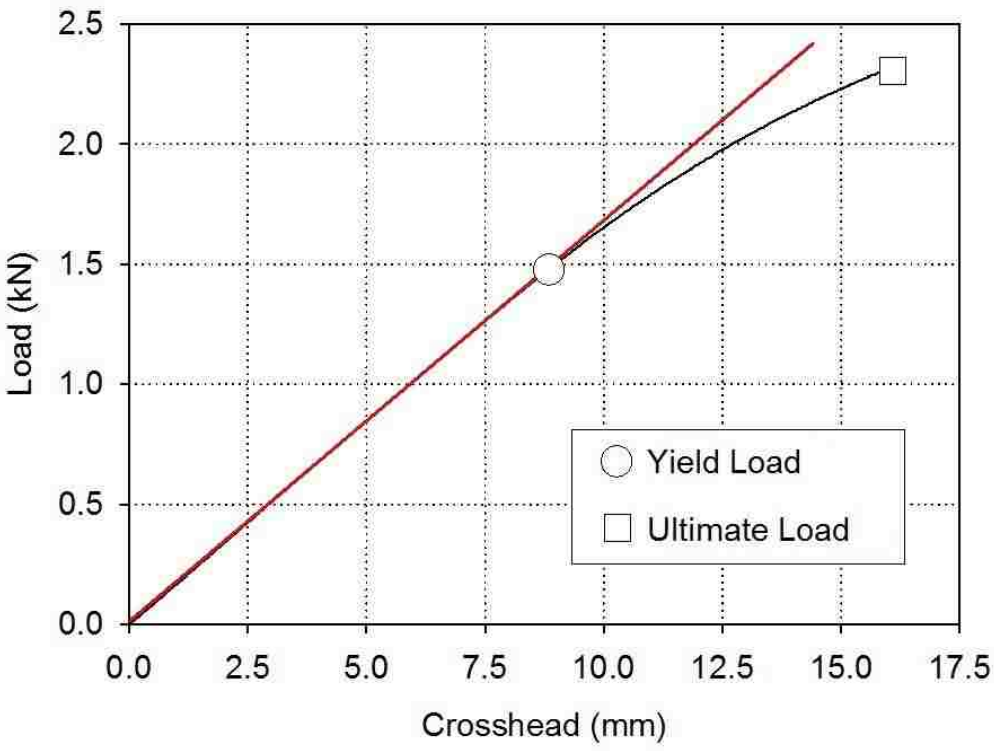

Figure 36. The load versus crosshead displacement response for the three-point bending testing.

6.9 Material Property Summary

A list of acquired material yield strengths is shown in Table 1 below. Poisson's Ratio is 0.23.

Yield Stress (MPa)					
Tensile Parallel	Tensile Perpendicular	Compression Parallel	Compressing Perpendicular	Shear Parallel	Shear Perpendicular
17.638	0.127	29.818	11.546	5.490	3.137

Table 4. Yield strengths list for all six wood orientation for selected plywood.

Ultimate Stress (MPa)					
Tensile Parallel	Tensile Perpendicular	Compression Parallel	Compressing Perpendicular	Shear Parallel	Shear Perpendicular
31.021	0.201	46.001	22.501	5.925	6.812

Table 5. Ultimate strengths list for all six wood orientation for selected plywood.

7 Material Model Generation For the CRSIAD

7.1 Scope of Developing the Material Model

7.1.1 Completion of the Material Model

The parameters of the strength section of the material model (MAT_WOOD) have been acquired from the previous section. In this section, the remaining sections of the material model, namely, the stiffness, hardening, damage and rate effect sections are to be acquired for completing the material model.

The stiffness parameters (elastic modulii) of the material model were simply attainable by calculating the stress/strain ratio of the elastic portions of the stress-strain response plots derived from the previous section. With the stiffness and strength sections of the material model acquired inserted into MAT_WOOD, MAT_WOOD was now ready to be used for simulation in LS-DYNA with the program-default values of the hardening, damage and rate effect parameters. Such temporary material model was used as a foundation of MAT_WOOD for further generating the material model.

The test specimens were constructed in LS-PrePost to the identical geometries as the specimens tested in the lab. Meshing for the specimens was completed in LS-PrePost. The mesh quality of each specimen was checked by the Element Quality Check within LS-DYNA to ensure the consistency of the mesh all across the specimen. The standards are listed in Table 6 below.

Quality Check Items	Allowable Value	Ideal Value	Worst Value
Characteristic Length (mm)	1	N/A	N/A
Aspect Ratio	10	0	$+\infty$
Skew (deg)	45	0	90
Warpage (deg)	10	0	90
Jacobian	0.6	1	-1
Minimum Triangular Angle (deg)	30	60	0
Maximum Triangular Angle (deg)	120	60	180
Minimum Quadratic Angle (deg)	45	90	0
Maximum Quadratic Angle (deg)	135	90	180

Table 6. Mesh quality check standard by LSTC.

The characteristic length, namely, L_e is an important dimension that defines the scale of an element so that appropriate time step can be created in the simulation. Since this investigation only involved Element Formulation (ELFORM) type 1 and 2, L_e is determined by the following equation,

$$L_e = V_{element} / A_{max}$$

The aspect ratio is calculated by dividing the maximum length side of an element by the minimum length side of the element. It is calculated in the same fashion for all faces of three-dimensional elements.

The skew is calculated by finding the minimum angle between the vector from each node to the opposing mid-side and the vector between the two adjacent mid-sides at each node of the element.

The warpage is calculated by splitting a quad into two trias and finding the angle between the two planes which the trias form. The quad is then split again, this time using the opposite corners and forming the second set of trias. The angle between the two planes which the trias form is then found. The maximum angle found between the planes is the warpage of the element.

The Jacobian is a measure of the deviation of a given element from an ideally shaped element. The Jacobian value ranges from -1 to 1, where 1 represents a perfectly shaped element. Since most elements involved in the investigation are quadratic elements, the check is performed by mapping an ideal quadratic element coordinates onto the actual elements in the global coordinates (-1,-1), (1,-1), (1,1) and (-1,1).

The minimum triangular angle and maximum triangular angle apply to all the triangular shell and solid elements, where as the minimum quadratic angle and maximum quadratic angle apply to all the quadratic shell and solid elements. These angles should be kept within the allowable limits to avoid sharp corners of the elements that may lead to stress concentration or instability.

The actual mesh quality check items for each specimen was compared with the allowable value from Table 6 and quantity of violated elements was reported as a measure of mesh quality. Mesh-sensitivity study was completed to ensure appropriate mesh sizing to maintain all the material testing details with minimum computational time. The constructed specimens in LS-PrePost were then tested in the identical boundary conditions as the testing conditions from the original experiments with the given material foundation of MAT_WOOD described earlier in this section. Discrepancies between the simulated data and experimental data were expected due to the hardening, damage and rate effect sections of the material model being left to default. While comparing the simulated data with the experimental data, the discrepancies had become opportunity for these particular default parameters to be appropriately tuned to match the simulated data to the

experimental data. Once the hardening, damage and rate effect sections of the material model were tuned and optimized, the material model was complete and ready to be validated both qualitatively and quantitatively. The material model was then safe to be implemented into the design of the CRSIAD with satisfying validation results.

7.1.2 Qualitative Validation of the Material Model

Three-point-bending test is a proven approach to validate material properties according to ASTM Standard D143-94 [20]. The complete material model described in the previous section was implemented into a virtual three-point bending test in the identical configuration as the lab test in LS-DYNA. The load-displacement data of the simulated results was then extracted and compared with the experimental results. The simulated results were qualitatively validated by the convergence between the simulated results and experimental results.

7.1.3 Quantitative Validation of the Material Model

A validation criterion was needed for quantitatively validating the simulated data with the experimental data from all the testing events in order to ensure the validity of the material model. Equation (1) was used to calculate validation metrics, where V is the validation metric, L is the crosshead displacement, L_1, L_2 are the initial and final values of crosshead displacement., $R_{\text{Exp}}(L)$ is the experimental load value, and $R_{\text{Theory}}(L)$ is simulation load value [26].

$$V = 1 - \frac{1}{L_2 - L_1} \int_{L_1}^{L_2} \tanh\left(\left|\frac{R_{Exp}(L) - R_{Theory}(L)}{R_{Theory}(L)}\right|\right) dL \quad (1)$$

Accumulated error has been calculated by equation (2).

$$E\ (Error) = \frac{1}{L_2\text{-}L_1} \int_{L_1}^{L_2} \left| \frac{R_{Exp}(L)\text{-}R_{Theory}(L)}{R_{Theory}(L)} \right| dL \quad (2)$$

Two conditions associated with the amount of deformation were used to calculate the validation metrics and accumulated error; validation metrics for the entire range of data (from test start to material failure) and validation metrics prior to material yielding. For our specific application, the latter criterion is more appropriate since deformation prior to yielding is expected during service.

7.2 Preliminary Material Model Overview

This section is a review of the acquired key parameters and the remaining parameters to be acquired for completing the material model. Referring back to Section 7.1.1, the material model (MAT_WOOD) consists of five main sections.

1. The stiffness parameters were developed from the original experimental results as mentioned in 7.1.1. The parallel elastic modulus, namely, E_L for the tensile and compression tests were calculated to be 8.050 GPa and 9.810 GPa respectively. The perpendicular elastic modulus, namely, E_T for the tensile and compression tests are 0.0915 GPa and 0.462 GPa. However, MAT_WOOD only contains one elastic modulus for both tensile and compression testing events in the same wood fibre direction. For example, E_L is defined for both tension and compression testing events in the parallel direction of the wood fibre in MAT_WOOD despite the fact that the experimental results yielded different elastic modulii between the tensile and compression tests. According to ASTM standards D143-94 [20], the greater value between the two should be chosen as the value of E_L. Therefore, the compressive elastic modulii for both the parallel and perpendicular directions were chosen to be E_L and E_T for the material model, namely, 9.810GPa and 0.462GPa respectively due to their greater values compared to the values from the tensile tests.

2. The strength parameters of the material model were also identified from the stress-strain response plots extracted from experimental results. The ultimate tensile strength in parallel direction of the wood fibre is 0.034 GPa; the ultimate tensile strength in perpendicular direction of the wood fibre is 0.0002 GPa; the ultimate compressive stress in parallel direction of the wood fibre is 0.046; the ultimate compressive strength in perpendicular direction of the wood fibre is 0.096 GPa; the ultimate shear strength in parallel direction of the wood fibre is 0.004 GPa; the ultimate shear strength in perpendicular direction of the wood fibre is 0.0002 GPa.

3. The hardening parameters of the material model were acquired by tuning. As an example for $N\|$ and $N\perp$(Hardening Initiation Rates), a value of 0.3 (for 30%) means the pre-peak plastic deformation occurs at 30% of the loading span before the ultimate strength; For $c\|$, $c\perp$(Hardening Rate), a value of the range 100 and 1000 (unitless) was selected based on the amount of nonlinearity, with lower value being gradual hardening and higher value being rapid hardening. The hardening section of the material model does not apply to tension and shear testing events so that it was only used for compression test events.

4. The softening parameters of the material model were acquired by tuning. These parameters were also tuned to match the simulated load-displacement data to the experimental data. The post-peak softening parameters, namely, B and D as mentioned in Section 5.1.2 are valued between 10 and 50 (unitless) with the smaller value to represent gradual initial softening and higher value to represent rapid initial softening. The best-suited values were chosen when the convergence between the simulated results and experimental results was satisfied. Since compression testing events do not have these parameters available in MAT_WOOD by design, this section of the material model was only used for all tensile and shear testing events.

5. Rate Effect section of the material model was not applicable in this investigation because the CRSIAD was designed to be operated by hands under non-high speed conditions. All rate effect parameters were set to zero.

7.3 Tensile Testing In the Parallel Direction of the Wood Fibre

7.3.1 Specimen Construction

The geometry of the virtual specimen for this test was constructed and modeled to be the middle section of the original specimen that was tested in the lab as shown in Figure 37 (A). The dimensions of the virtual specimen (Figure 37 (A)) were created based on the dimensions of the original specimen (Figure 37 (B)). By simplifying the geometry of the virtual specimen from the original specimen, the simulation of the testing was focused on only the testing region of the specimen so that computational time and error were reduced. The mesh details are shown in Table 7 below.

Quality Check Items	Minimum Value	Maximum Value	Number of Violated Elements (%)
Characteristic Length (mm)	1.88	2.47	0
Aspect Ratio	1.01	1.33	0
Skew (deg)	0	21.7	0
Warpage (deg)	0	0	0
Jacobian	0.912	1	0
Minimum Quadratic Angle (deg)	67.3	90	0
Maximum Quadratic Angle (deg)	90	113	0

Table 7. Mesh quality check for the testing.

The previously developed material model foundation was applied to this virtual specimen with AOPT being set to 2. The parallel direction was defined to be in the direction of the z-axis (0,0,1) and the perpendicular direction was defined to be in the direction of the x-axis (1,0,0) according to the coordinate system shown in Figure 37 (A).

(A) (B)

Figure 37. Specimen for tensile test parallel to fibre direction in FEA geometry (A) compared to lab test specimen (B).

7.3.2 Virtual Test Setup

The boundary conditions of this testing event are set to allow the bottom face of the specimen (Figure 37 (A)) to be constrained and the top face of the specimen being pulled in the positive z-axis direction in order to match the original experiment setup. The bottom face of the geometry of the specimen in Figure 37 (A) was constrained in all degree of freedoms, which imitated the actual specimen being clamped at the bottom grip crosshead of the MTS C45-305 (as mentioned in Section 5.2.3). Translational z-axis degree of freedom was assigned to all the nodes on the top face of the specimen in Figure 37 (A), which allows a translational motion to be only applied to these nodes in the positive z-axis direction.

BOUNDARY_PRESCRIBED_MOTION_SET was applied to the node set of all the nodes on the top face of the specimen with displacement control. The prescribed motion was applied to the virtual specimen until the specimen failure was achieved. The mid-span resultant force of the specimen (in z-axis direction) was recorded and plotted as load-displacement response for the relevant parameters in this testing event to be tuned to match the original experimental data. The load data output (RCFORC) was assigned to the node set on the top face of the specimen in order to export the load data. The displacement data was collected at the same node set to match the load data so that load-displacement response can be plotted.

7.3.3 Results and Parameter Tuning

As specified in Section 5.1.2, only parameters in the softening section of the material model need to be tuned in the tensile testing event. In this test, the main objective was to tune the value of *B* (Parallel Softening Parameter). Since the specimen failure of this testing event occurred in a rapid fashion after the ultimate strength according to the experimental data as shown in Figure 38, the value of *B* was set to the greater side of its range to begin with. Since *B* is also used in the shear testing event, the value of it was later optimized for both the tensile and shear testing events. The closest matching load-displacement response was achieved as shown in Figure 38. The value of *B* was tuned to 2.100E+01.

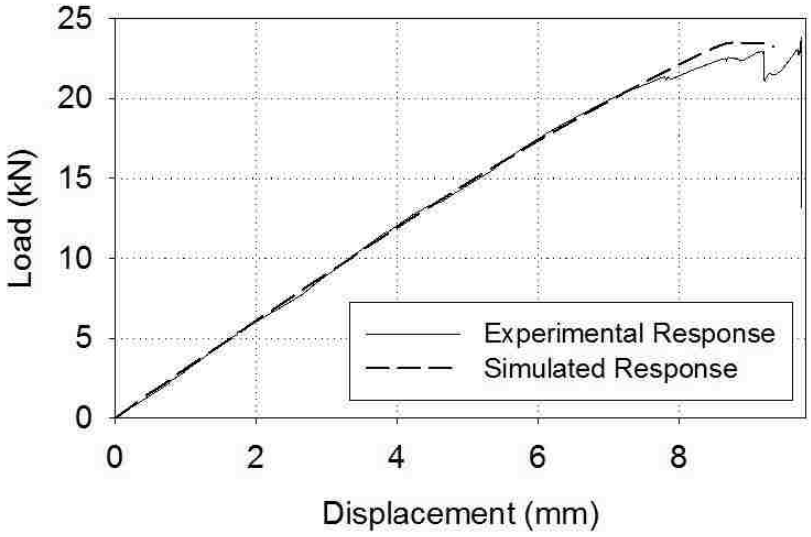

Figure 38. Tension parallel to fibre direction load versus displacement comparison.

With the tuned parallel softening parameter *B* added to the previously developed material model foundation, both the elastic and plastic material characteristics are well-matched to the experimental data as shown in Figure 38. Due to the lack of ability to tune the pre-peak plastic deformation portion of the material model by design, the overall prediction of the material load-displacement response solely relied on the elastic and post-peak plastic portions of the material characteristics. The simulated and experimental load-displacement response plots started to separate slightly before the ultimate tensile strength at 7.65 mm on displacement axis and 20.92 kN on load axis. Despite such small discrepancy between the two curves, peak load values are very close - 22.94 kN for the experimental data and 23.49 kN for the simulated data. More importantly, the convergence of the elastic portions between the simulated data and experimental data is virtually good which was later verified in the validation metrics in Section Appendix E, which ensures accurate prediction of the material model for the yield strength during the design phase of the CRSIAD.

7.4 Tensile Testing In the Perpendicular Direction of the Wood Fibre

7.4.1 Specimen Construction

Unlike the specimen described in Section 7.3.1, the specimen in this testing event was constructed as an exact replica of the original specimen tested in the lab due to the simplicity of the specimen geometry as shown in Figure 39 (A). The mesh details are shown in Table 8.

Quality Check Items	Minimum Value	Maximum Value	Number of Violated Elements (%)
Characteristic Length (mm)	0.923	0.923	0
Aspect Ratio	1.06	1.06	0
Skew (deg)	0	0	0
Warpage (deg)	0	0	0
Jacobian	0.999	0.999	0
Minimum Quadratic Angle (deg)	90	90	0
Maximum Quadratic Angle (deg)	90	90	0

Table 8. Mesh quality check for the testing.

The previously developed material model foundation was applied to this virtual specimen with AOPT being set to 2. The parallel direction was defined to be in the direction of the x-axis (1,0,0) and the perpendicular direction was defined to be in the direction of the z-axis (0,0,1) according to the coordinate system in Figure 39 (A).

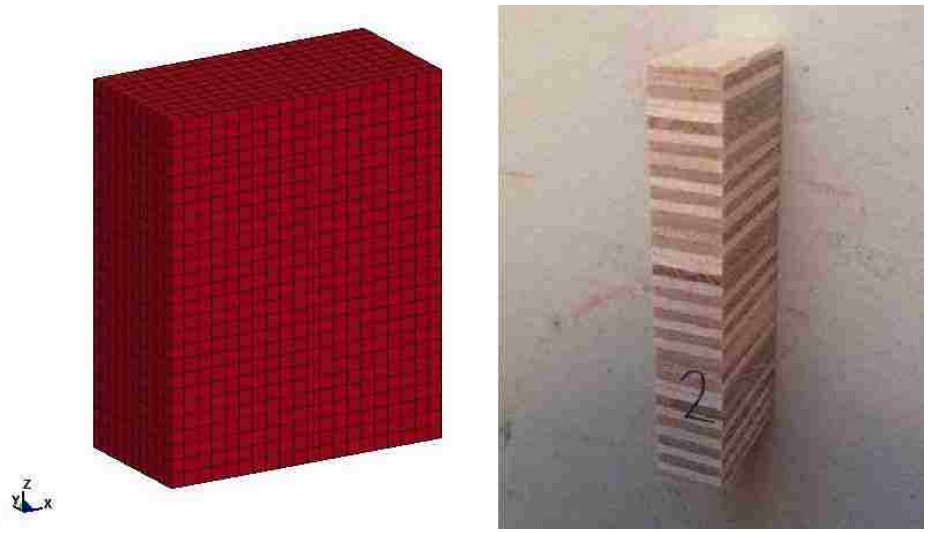

(A) **(B)**

Figure 39. Specimen for tensile test perpendicular to fibre direction in FEA geometry (left) compared to lab test specimen (right).

7.4.2 Virtual Test Setup

Similar to the previous tensile test simulation event (Section 6.2.2), the bottom face of the specimen geometry section was constrained in all degree of freedoms, which imitated the original specimen being clamped at the bottom grip crosshead on the MTS C45-305. Translational z-axis degree of freedom was assigned to all the nodes on the top face of the specimen, which simulated the pulling motion of the specimen during the loading process. All the boundary conditions are identical to the previous testing event in Section 7.3.2.

7.4.3 Results and Parameter Tuning

Similar to Section 7.3.3, only the softening parameter of the material model were to be tuned in this testing event, namely, *D* (Perpendicular Softening Parameter). Like *B*, *D* is also correlated to the shear testing event in the same wood

orientation. *D* only dictates the shape of post-peak softening portion of the material loading characteristics and ability of tuning pre-peak hardening portion was unavailable. With the numbers of iterations of tuning *D*, the best-matching load-displacement response from the simulation is shown in Figure 40. Although the predicted response of the pre-peak hardening portion of the loading characteristics in this testing event is not matching well to the experimental result due to the lack of ability to tune, the elastic modulus and peak strength were well predicted. The value of *D* was tuned to be 1.800E+01.

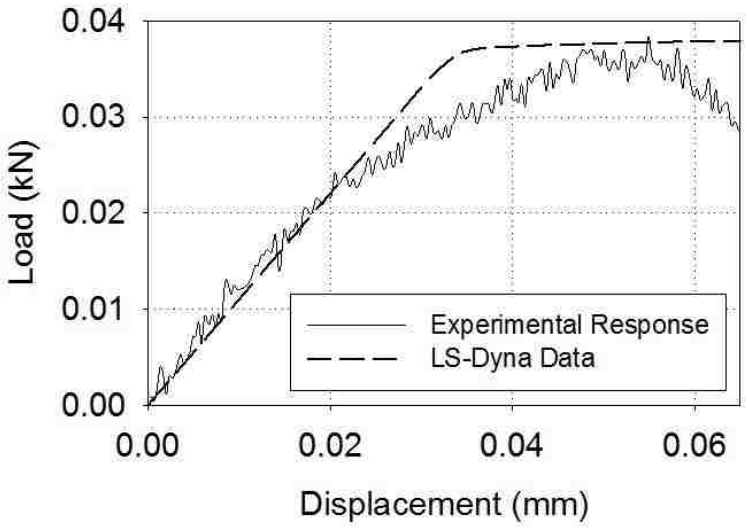

Figure 40. Tension Perpendicular to fibre direction load versus displacement comparison.

The low ultimate tensile load (0.036 kN) in this testing event has indicated that main loading forces of the CRSIAD should not be applied to the perpendicular direction of the wood fibre. The design should allow majority of loading to be applied to the parallel direction of the wood fibre.

7.5 Compression In the Parallel Direction of the Wood Fibre

7.5.1 Simulation Specimen

The geometry of the virtual specimen for this test (Figure 41 (A)) was modeled as exact duplicate of the original specimen (Figure 41 (B)). The mesh details are listed in Table 9 below.

Quality Check Items	Minimum Value	Maximum Value	Number of Violated Elements (%)
Characteristic Length (mm)	1.23	1.23	0
Aspect Ratio	1.03	1.03	0
Skew (deg)	0	0	0
Warpage (deg)	0	0	0
Jacobian	1	1	0
Minimum Quadratic Angle (deg)	90	90	0
Maximum Quadratic Angle (deg)	90	90	0

Table 9. Mesh quality check for the testing.

The previously developed material model foundation was applied to this virtual specimen with AOPT being set to 2. The parallel direction was defined to be in the direction of the z-axis (0,0,1) and the perpendicular direction was defined to be in the direction of the y-axis (0,1,0) according to the coordinate system in Figure 41 (A).

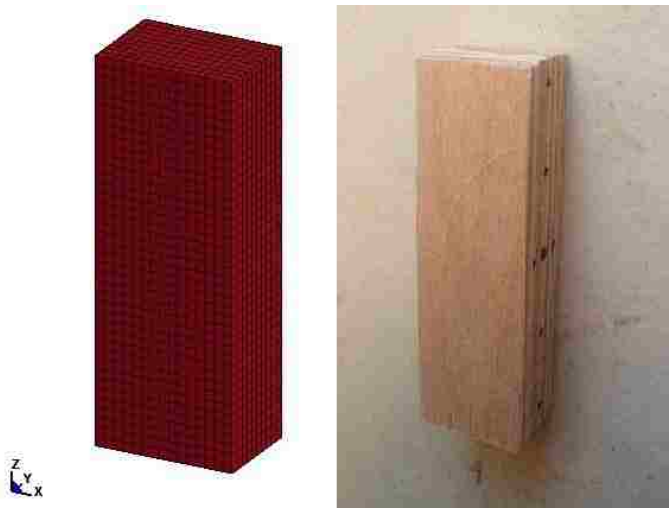

(A) (B)

Figure 41. Specimen for compression test parallel to fibre direction in FEA geometry (A) compared to lab test specimen (B).

7.5.2 Virtual Test Setup

With the specimen positioned in the orientation of Figure 41 (A), the bottom face of the specimen was seated flatly on a virtual rigid wall (RIGIDWALL_GEOMETRIC_FLAT) that was created in x-y plane. The setup of the virtual specimen is a imitation of the original specimen being placed on the bottom compression plate on MTS 43-504. The top portion of the specimen was configured in a similar fashion to the tensile test simulation, in which a node set was created on the top face of the specimen and assigned a negative z-axis translational motion (BOUNDARY_PRESCRIBED_MOTION_ SET) in order to simulate the compression motion.

The specimen was loaded until its failure point. Load data output (RCFORC) was assigned to the created node set to provide load data. Displacement data was also collected at the top surface so that a load-displacement response was plotted.

7.5.3 Results and Parameter Tuning

As mentioned in Section 7.2, the main objective of this test simulation event was to appropriately tune the hardening section of the material model. These parameters, namely, *N*|| (Parallel hardening initiation) and *c*|| (Parallel hardening rate) were to be tuned for the simulated load-displacement response to match the experimental load-displacement response.

These two parameters dictate the shape of pre-peak hardening portion of the loading characteristics of the material model while the ability of tuning the post-peak hardening characteristics was unavailable. With the ability to only tune the pre-peak plastic deformation zone, convergence between the simulated data and experimental data was improved over the tensile testing simulation events as shown in Figure 42. By tuning the value of *N*||, the yield point of the simulated response was matched to converge with the yield point of the experimental response. By tuning the value of *c*||, the pre-peak hardening portion of the simulated response was closely matched to the portion of the experimental data. The value and location of the simulated ultimate load (10.577 kN at 0.99 mm) are very close to the ones from the experimental response (10.538 kN at 0.91 mm). As a result, the resultant tuned values of the two hardening parameters are *N*|| = 4.000E-01 and *c*|| = 2.000E+02 respectively.

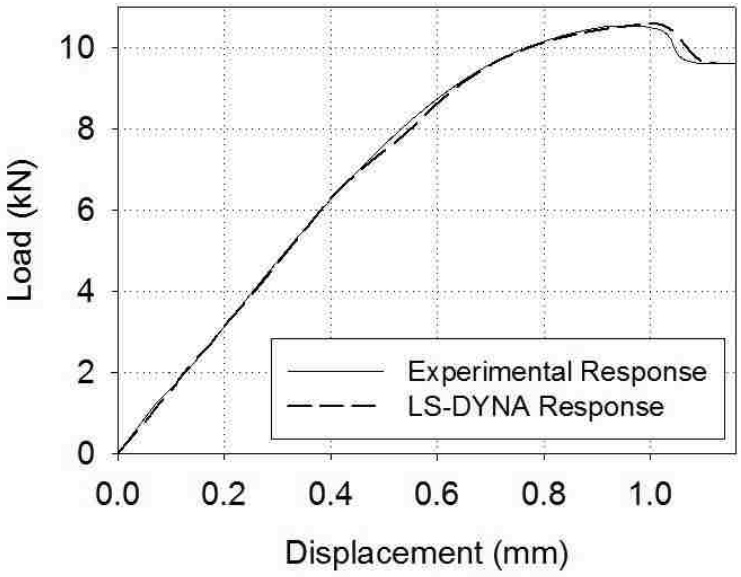

Figure 42. Compression Parallel to fibre direction load versus displacement comparison.

7.6 Compression In the Perpendicular Direction of the Wood Fibre

7.6.1 Simulation Specimen

The geometry of the virtual specimen for this test was modeled as exact duplicate of the actual specimen, namely, Part 1 in Figure 43 (A). The mesh details are listed in Table 10 below.

Quality Check Items	Minimum Value	Maximum Value	Number of Violated Elements (%)
Characteristic Length (mm)	1.85	1.85	0
Aspect Ratio	1.03	1.03	0
Skew (deg)	0	0	0
Warpage (deg)	0	0	0
Jacobian	1	1	0
Minimum Quadratic Angle (deg)	90	90	0
Maximum Quadratic Angle (deg)	90	90	0

Table 10. Mesh quality check for the testing.

The previously developed material model foundation was applied to this virtual specimen with AOPT being set to 2. The parallel direction was defined to be in the direction of the x-axis (1,0,0) and the perpendicular direction was defined to be in the direction of the z-axis (0,0,1) according to the coordinate system in Figure 43 (A).

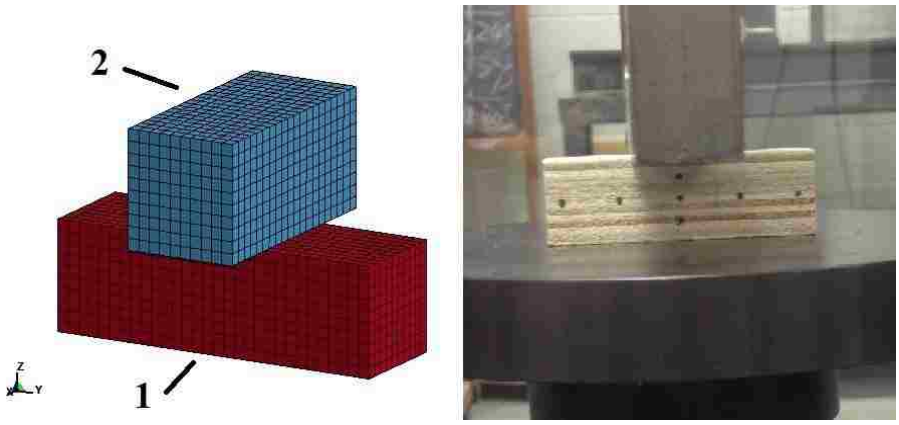

A B

Figure 43. Specimen for compression test perpendicular to fibre direction in FEA geometry (A) compared to lab test specimen (B).

7.6.2 Virtual Test Setup

The bottom face of the specimen (Part 1) was seated flatly on a virtual horizontal rigid wall (RIGIDWALL_GEOMETRIC_FLAT) that was created in x-y plane. The setup for the top face of the specimen was configured differently from the previous testing event (Section 7.5.2) due to the addition of a compression plate in the original experiment. Therefore, an additional entity (Part 2 in blue) was created to replicate the compression plate as shown in Figure 43 (B). MAT_RIGID was assigned to Part 2 as the plate is part of the testing equipment and considered as rigid body. The contact between Part 1 and Part 2 was defined as CONTACT_AUTOMATIC_SURFACE_TO_SURFACE. A translational motion, namely, BOUNDARY_PRESCRIBED_MOTION_SET was applied to Part 2 in the negative direction of z-axis to simulate the compressing motion to the specimen. The load measurement was acquired from the sensor DATABASE_RCFORC based on the contact interface between Part 1 and Part 2. The displacement measurement was acquired from the sensor DATABASE_RBDOUT rigid body movement from Part 2. The load and displacement data were correlated to produce load-displacement response for the specimen.

7.6.3 Results and Parameter Tuning

Similar to Section 7.6.3, only parameters from hardening section of the material model were tunable in this testing event. The main objective of simulating this testing event was to tune these parameters, namely, $N\perp$ and $c\perp$.

These two parameters dictate the shape of pre-peak hardening portion of the load-displacement response. With appropriate tuning, the similar hardening parameters in the parallel direction were proved to be effective on achieving good convergence on the yield strength and location of the simulated and experiment loading response plots as discussed in Section 7.6.3. Similarly, the yield loading value and location are well-converged in this testing event as shown in Figure 44. The values of the two parameters were tuned to be $N\perp$ = 8.500E-01 and $c\perp$ = 7.000. The prediction of the ultimate compressive load from the simulation is close to the experimental result with simulated peak load being 7.865 kN at 1.67 mm and experimental peak load being 7.960 kN at 1.62 mm.

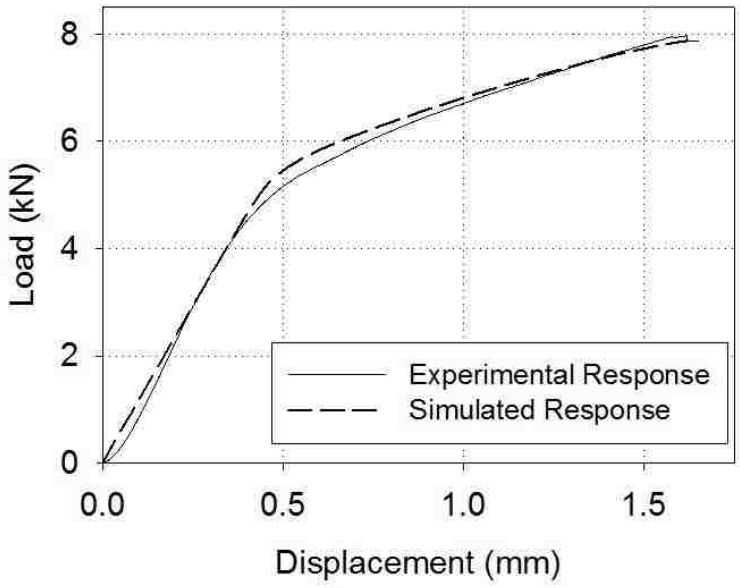

Figure 44. Compression perpendicular to fibre direction load versus displacement comparison.

7.7 Shear In the Parallel Direction of the Wood Fibre

7.7.1 Simulation Specimen

The geometry of the virtual specimen for this test was modeled as exact duplicate of the original specimen, namely, Part 1 in Figure 45 (A). The mesh details are listed in Table 11 below.

Quality Check Items	Minimum Value	Maximum Value	Number of Violated Elements (%)
Characteristic Length (mm)	2.38	2.38	0
Aspect Ratio	1	1	0
Skew (deg)	0	0	0
Warpage (deg)	0	0	0
Jacobian	1	1	0
Minimum Quadratic Angle (deg)	90	90	0
Maximum Quadratic Angle (deg)	90	90	0

Table 11. Mesh quality check for the testing.

The previously developed material model foundation was applied to this virtual specimen with AOPT being set to 2. The parallel direction was defined to be in the direction of the z-axis (0,0,1) and the perpendicular direction was defined to be in the direction of the x-axis (1,0,0) according to the coordinate system in Figure 45 (A).

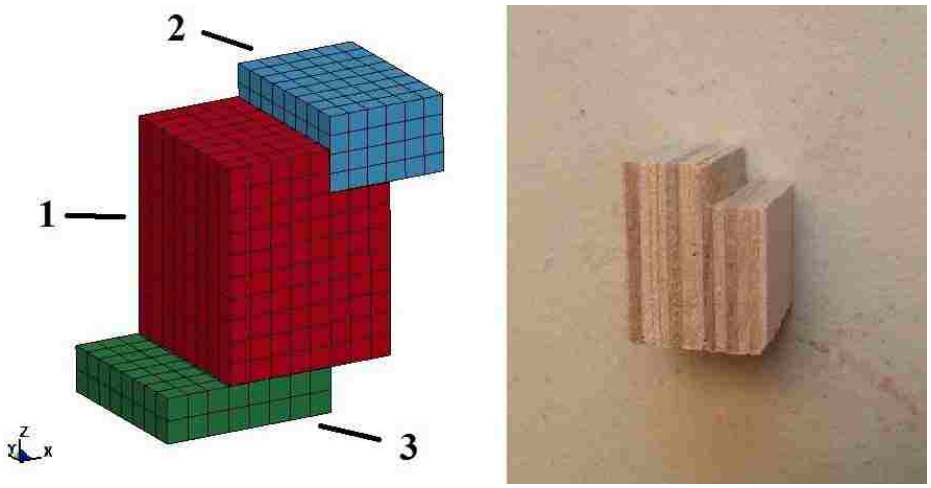

A **B**

Figure 45. Specimen for shear test parallel to fibre direction in FEA geometry (A) compared to lab test specimen (B).

7.7.2 Virtual Test Setup

To virtually create the shear test setup from the original experiment, three parts had to be created in LS-PrePost to model this testing event. As specified in the previous section, Part 1 is the specimen from Figure 45 (A). Part 2 represents the top shear plate of the Tinius Olsen Fixture and Part 3 represents the bottom seating plate of the Tinius Olsen Fixture. Parts 2 and 3 were modeled in rigid material (MAT_RIGID) because they are part of the testing fixture which are considered to be rigid. BOUNDARY_PRESCRIBED_MOTION_RIGID was applied to Part 2 with displacement control (VAD = 2) in the direction of z-axis (DOF = 3) in order to simulate the shear movement. Part 3 was constrained in all degrees of freedom (CMO = 1, CON1 = 7 and CON2 = 7) as it represents the base of the testing fixture. Part 2 was driven until failure of Part 1 occurred. The load data output (RCFORC) was assigned to contact interface between Part 1 and Part 2 to export load data in the direction of the z-axis to represent crosshead load data of the MTS-43-504. The rigid body movement sensor (DATABASE_RBDOUT) was included to acquire the

displacement data of Part 2. Combining the load and displacement data, the load-displacement response was plotted as shown in Figure 46.

7.7.3 Results and Parameter Tuning

As mentioned in Section 7.2, only the parameters from the softening section of the material model were tunable in this testing event. The main objective of the tuning in this testing event was to tune *B*. Since the value of this parameter was determined earlier in Section 7.3.3, the same value was used in this test simulation as a starting point.

With the same value of this parameter being inserted into the material model for shear test, there was small discrepancy present. The value suited for tensile test did not best suit shear test. The value was then tuned to achieve the best balance in terms of convergence between the simulated response and experimental response for both the tensile and shear test (B = 2.100E+01). The resultant load-displacement response plot is shown in Figure 46 for this testing event.

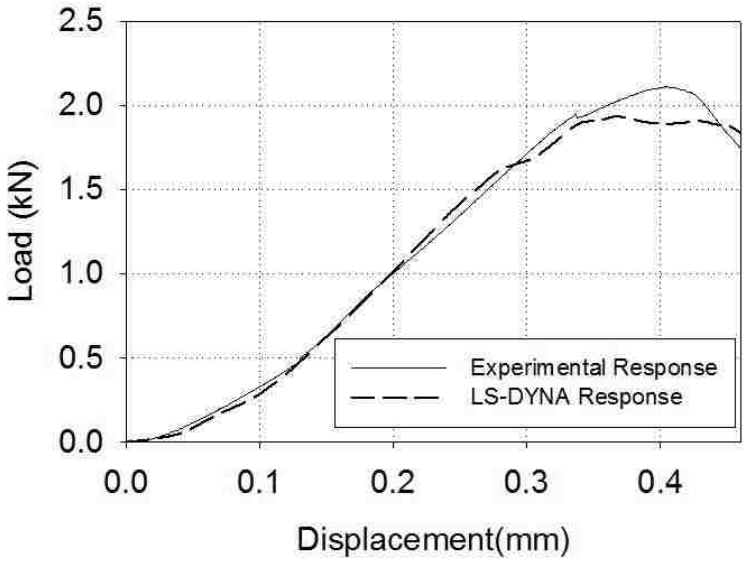

Figure 46. Shear Parallel to fibre direction load versus displacement comparison.

7.8 Shear In the Perpendicular Direction of the Wood Fibre

7.8.1 Simulation Specimen

Due to the fact that the original specimen in this testing event is linearly proportional to the specimen used in the previous testing event (Section 7.7.1) in terms of its dimensions, the geometry model of the previously testing event was used for this testing event. The mesh details are identical to the list in Table 11 in Section 7.1.1. The same material model was also applied to the virtual specimen except for the orientation of AOPT, in which the parallel direction was defined to be in the direction of the x-axis (1,0,0) and the perpendicular direction was defined to be in the direction of the z-axis (0,0,1) according to the coordinate system in Figure 47 (A).

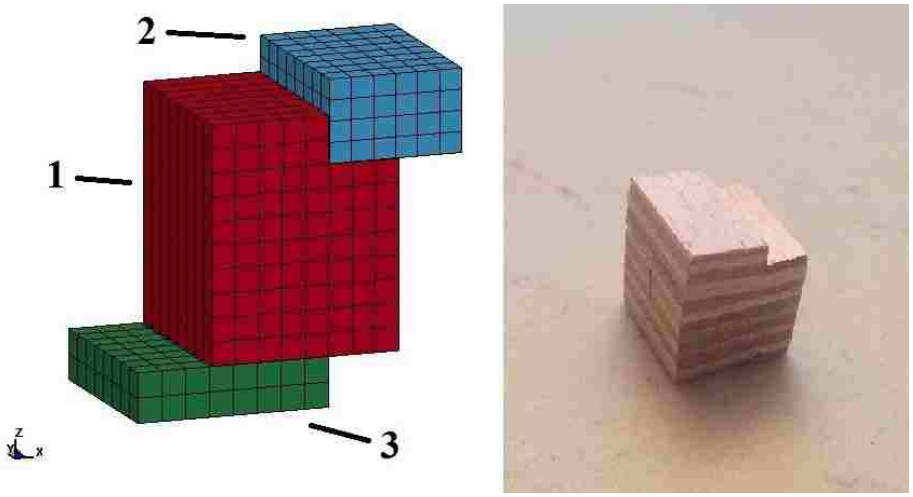

A **B**

Figure 47. Specimen for shear test perpendicular to fibre direction in FEA geometry (A) compared to lab test specimen (B).

7.8.2 Virtual Test Setup

The setup for this test event is identical to the previous test (Section 7.7.2).

7.8.3 Results and Parameter Tuning

The main objective of this simulation testing event is to determine the value of the parameter *D*. The tuning approach of *D* is identical to B as described in the Section 7.7.3. Therefore, the value of D was tuned in the same approach as Section 7.4.3, which is 1.8000E+01. The load-displacement data for this testing event is shown in Figure 48 with the implementation of *D*.

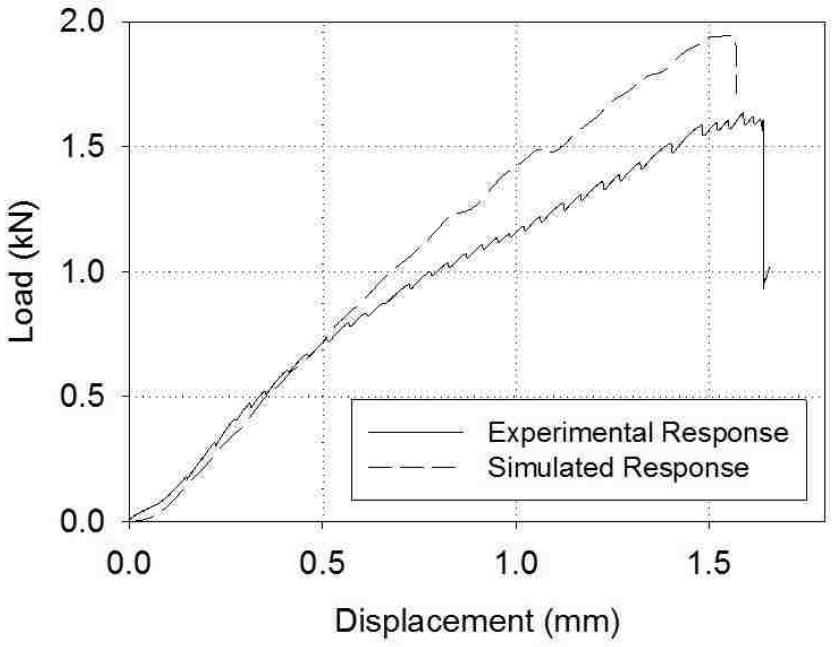

Figure 48. Shear Perpendicular to fibre direction load versus displacement comparison.

7.9 Qualitative Validation with Three-point Bending Test

By this point all the key parameters of the material model had been acquired and tuned and the material model was ready to be validated for further implementation. The key parameters are available in Section Appendix D.

7.9.1 Simulation Specimen

The geometry of the virtual specimen for this testing event, namely, Part 1 in Figure 49 was modeled as the exact duplicate of the original specimen with the direction of the wood fibre being parallel to the x-y plane. The mesh details are listed in Table 12 below.

Quality Check Items	Minimum Value	Maximum Value	Number of Violated Elements (%)
Characteristic Length (mm)	4.58	4.58	0
Aspect Ratio	1.04	1.04	0
Skew (deg)	0	0	0
Warpage (deg)	0	0	0
Jacobian	1	1	0
Minimum Quadratic Angle (deg)	90	90	0
Maximum Quadratic Angle (deg)	90	90	0

Table 12. Mesh quality check for the test.

The previously developed complete material model was applied to Part 1 with wood orientation being specified to match the experiment setup. AOPT was activated (set to 2) with parallel direction being defined in x-axis (1,0,0) and perpendicular direction being defined in z-axis (0,0,1).

7.9.2 Virtual Test Setup

The green and yellow cylinders, namely, Parts 3 and 4 respectively are the base support cylinders for the specimen in Figure 49. The top blue cylinder, namely, Part 2 was the loading cylinder that imitates the cylinder attachment to the crosshead of the MTS 45-305. All Parts 2, 3 and 4 were modeled in rigid material (MAT_RIGID) because they are simulated as part of the testing fixture which are considered as rigid bodies. BOUNDARY_PRESCRIBED_MOTION_RIGID was applied to Part 2, the loading cylinder, with displacement control (VAD = 2) in the direction of z-axis (DOF = 3) to simulate the loading motion. Part 3 and 4 were constrained in all degrees of freedom (CMO = 1, CON1 = 7 and CON2 = 7) as they are the fixed base support cylinders for the specimen as part of the testing fixture. The specimen was loaded until its failure point. The load data output (RCFORC) was assigned to contact interface between Part 1 and Part 2 to export load data in the direction of the z-axis to represent crosshead load data of the MTS C45-305. The contact loads of the two bottom cylinders were also recorded in the same fashion to verify the summation load from Part 3 and Part 4 is equal to the load from the top loading cylinder. The rigid body movement sensor (DATABASE_RBDOUT) was included to acquire the displacement data of Part 2. Combining the load and displacement data, the load-displacement response was plotted as shown in Figure 58.

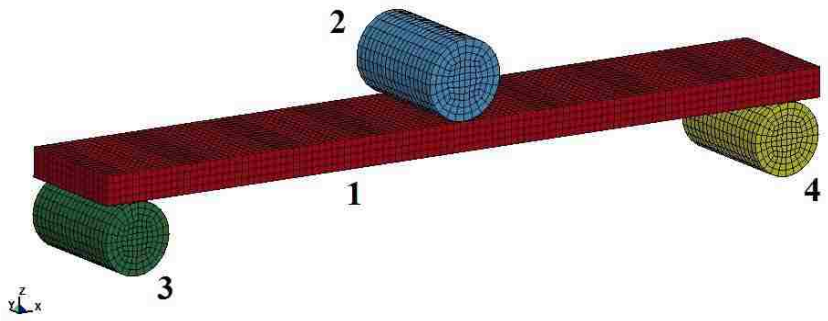

Figure 49. Three-point-bending test setup in LS-PrePost.

7.9.3 Results

The resultant load-displacement response was generated as shown in Figure 50 with no parameter tuning done. The prediction from the simulated response is generally satisfying due to good convergence with the experimental response for both the elastic and plastic material behaviours. The yield locations of both the simulated response and experimental responses occurred at 12.39 mm of the displacement. The simulated ultimate load value is only 0.1 kN lower than the experimental response, which is very close. Therefore qualitatively speaking, the developed material model for MAT_WOOD is a success in terms of accurately predicting the material loading behaviours for the selected plywood.

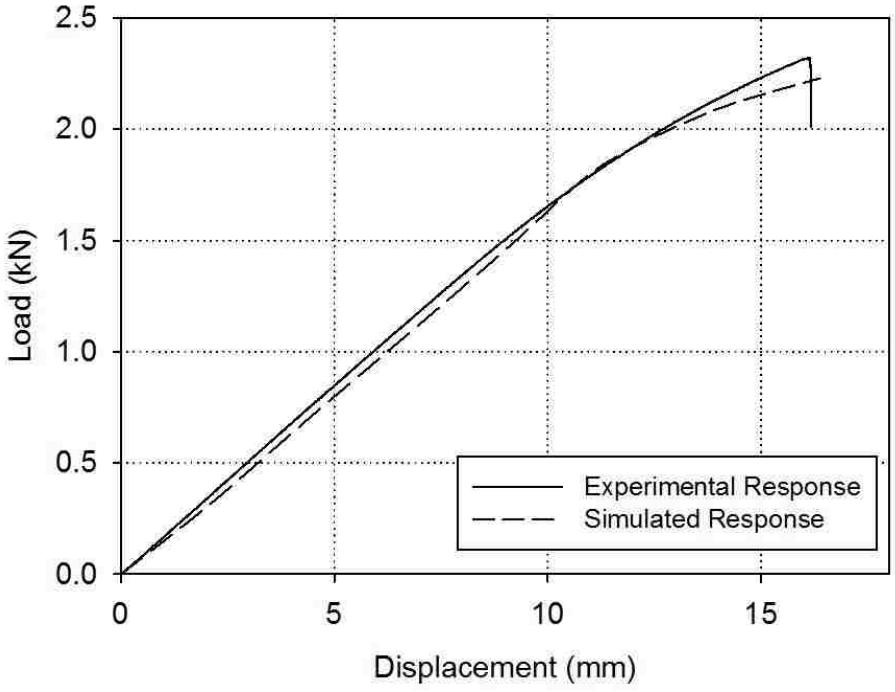

Figure 50. Three-point-bending load versus displacement comparison.

7.10 Quantitative Validation with Validation Metrics

With previously mentioned validation techniques from Section 7.1.3, validation metrics were calculated for the three-point bending test. The validation metric was calculated to be 0.974 for the entire loading range with accumulated error of 0.053. Values for the loading range prior to yielding were computed to be 0.975 and 0.052, for validation metric and accumulated error, respectively. The results reinforced the confidence of using the developed material model for MAT_WOOD. All validation metric data for the remaining test events is available in Appedix E.

8. CRSIAD FEA MODEL DEVELOPMENT

8.1 Geometry Model Development

With the previously developed assembly geometry from Section 4.4.5, the geometry was imported and constructed in LS-PrePost. The developed complete material model (MAT_WOOD) from Section 7 is adapted to the constructed geometry of the CRSIAD for further investigation.

8.1.1 Parts Description

The constructed parts within this simulation are listed as following:

The main device body, namely, Part 1 from Figure 53 is the main structure of the CRSIAD with the previously developed material model (MAT_WOOD) applied. This entity is the focus of load testing in the investigation. It is important that this entity needs to sustain a load that is equivalent to 400 lb of weight without yielding.

The loading Beam, namely, Part 2 from Figure 53 is the main loading mechanism that is firmly attached to the top section of Part 1. It is constructed by gluing three layers of the same plywood that Part 1 is made of. The loading beam is loaded equally at both of its ends with 400 lb of total weight in the direction towards the lower anchor points of the CRS. Part 2 is assigned the same material model (MAT_WOOD) that was previously developed.

The CRS seating surface, namely, Part 3 is the bottom part where Part 1 is seated on in Figure 53. Since this part is the base that supports both Part 1 and Part 2, it is modeled in rigid material (MAT_RIGID) while the same elastic modulus, density and mesh quality are maintained from the developed MAT_WOOD. Part 3 is fixed with all translational and rotational movements constrained (CMO = 1, CON1 = 7 and CON2 = 7).

8.1.2 Overall dimensions

Due to the irregular shape of the geometry of the CRSIAD, only a three-dimensional volume was specified to describe the dimensions of the device. These dimensions are shown as the following:

The Main Device Body (Part 1):

Length (x-direction): 320.08 mm

Width (y-direction): 190.05 mm

Height (z-direction): 313.85 mm

The Loading Beam (Part 2):

Length (x-direction): 57.15 mm

Width (y-direction): 550 mm

Height (z-direction): 76.23 mm

8.1.3 Mesh Constructing

The first step of constructing the geometry of Part 1 from Figure 53 was to start with its side profile, which was created in shell elements in LS-PrePost. Due to the symmetry of the geometry for the CRSIAD, the side profile was then appropriately extruded with solid elements in order to form a three-dimensional entity.

Following the above method, the outline of the side profile of Part 1 was imported from CATIA into LS-PrePost for mesh construction. To create mesh for this outline with shell elements, "N-line Meshing" was found to be suitable and adapted for this task. Due to the unique contour-shaped outline, "4-line Meshing" was conveniently selected.

In order to apply "4-line Mesh" to the outline of the profile, the profile needed to be appropriately divided into 4-line sections as shown in Figure 51. It was important to maintain the consistent shaping of the mesh in this two dimensional drawing because these shell elements were to be extruded to form solid elements in the next step. Therefore, quadratic shell elements were conveniently used for the "4-line Meshing".

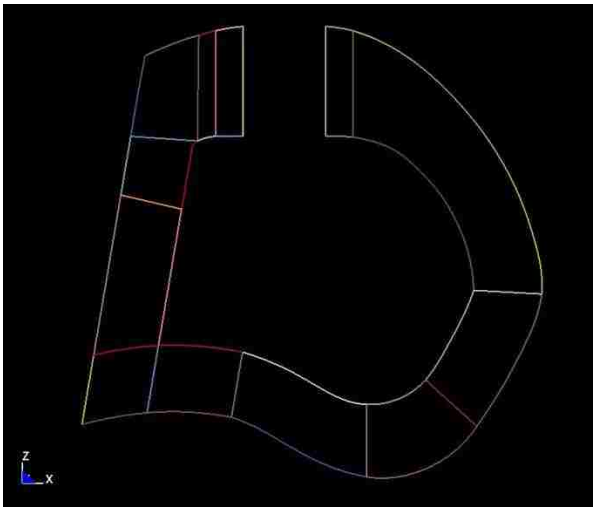

Figure 51. Device main frame side profile imported into LS-Prepost with 4-line sections.

As a 4-line section that consists of Lines 1, 2, 3 and 4 in a clockwise order, node quantities for Line 1 and Line 3, Line 2 and Line 4 were created identically so that all elements in this 4-line section contain four nodes (quadratic). With the 4-node element being extruded to form a solid element, that solid element would be guaranteed to contain eight nodes, therefore, a quadrahedral solid element.

All the mesh was constructed in a smooth-transitioning manner from section to section and corner to corner within the profile in Figure 52. The same mesh quality standards from all the previous material testing sections were applied to the meshing process here. After iterations of editing the mesh shaping and sizing, the resultant

side profile of Part 1 is shown in Figure 53, followed by mesh specifications in Table 13.

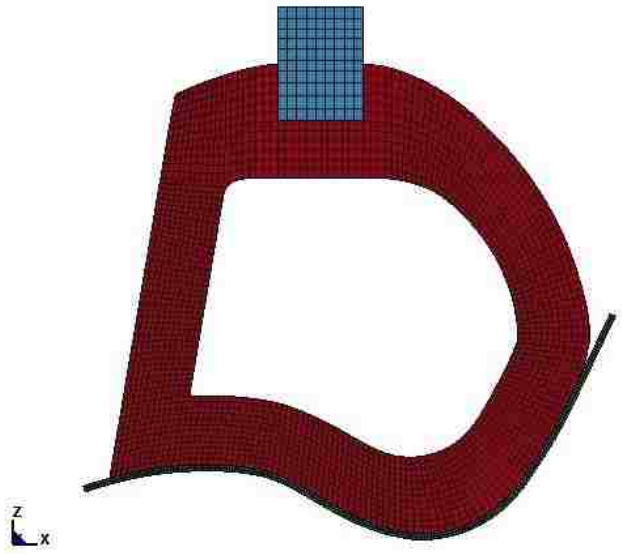

Figure 52. Side view of the CRSIAD geometry constructed in LS-PrePost.

Quality Check Items	Minimum Value	Maximum Value	Number of Violated Elements (%)
Characteristic Length (mm)	2.73	4.82	0
Aspect Ratio	1	1.89	0
Skew (deg)	0	34.2	0
Warpage (deg)	0	0	0
Jacobian	0.783	1	0
Minimum Quadratic Angle (deg)	55	90	0
Maximum Quadratic Angle (deg)	90	126	0

Table 13. Mesh quality check for the testing.

With the side profile (shell elements) selection, “Shell Offset” function was used to create through-thickness solid elements along y-axis. The thickness in this case is 38.1mm. Due to the symmetry of the device in y-direction, the solid section was duplicated to appropriate distance as a mirror image. Such duplication was implemented by first using “Project” function to project the shell-element profile onto a parallel plane from an appropriate distance according to CAD drawing. That projected shell-element profile was then padded into solid section like the first one.

Cross-structural beams were also converted from surface shell elements to solid elements across the middle span by “Shell Offset”. After deleting duplicated nodes and shell sections as well as communizing all solid sections into one part number, the entire device geometry model was created in three-dimensional coordinate system in LS-PrePost as shown in Figure 53.

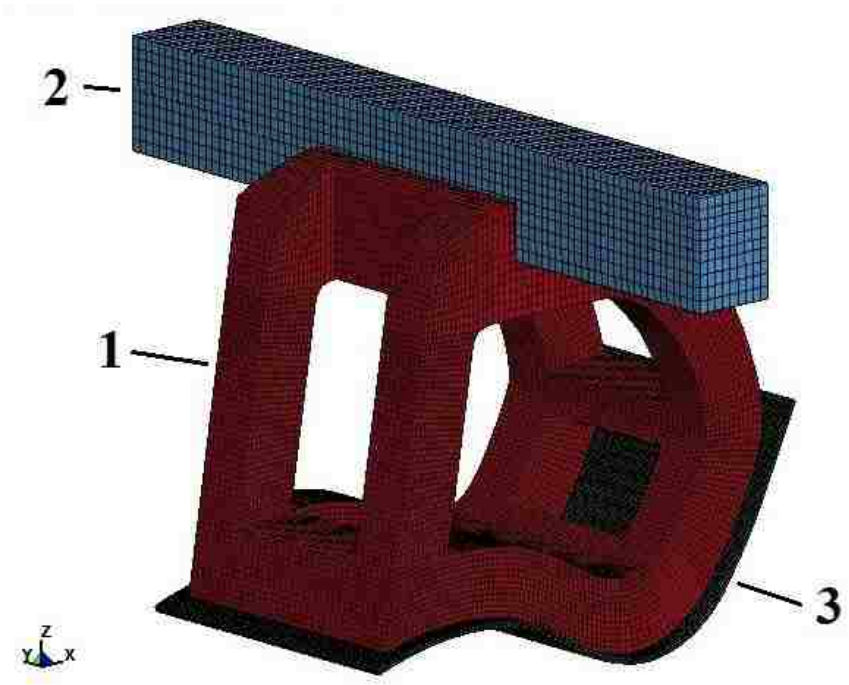

Figure 53. Fully constructed CRSIAD geometry in LS-DYNA ready for simulation.

With the measured density of the given Baltec Plywood, which is 6.774E-7 kg/mm^3, the weights of Parts 1 and 2 were measured to be 3.109 kg and 1.622 kg respectively in LS-PrePost. Overall weight is 4.731 kg without all attachments applied.

8.2 Simulation Procedure

The simulation consists of two loading conditions: A load of 1.78 kN (400 lbf) was applied to the loading beam (Part 2) at its end-faces towards the lower anchor locations of the CRS (1) when the CRS is in forward-facing configuration; (2) when the CRS is in rearward-facing configuration. One node set was created on each entire end-face of Part 2 as the loading points. With the aid of a local coordinate system with its origin being located at the center of the end-face of Part 2 and its x-axis being in the direction towards the lower anchor points of the CRS as shown in Figure 54 and Figure 55, "LOAD_NODE_SET" was then applied to the node sets to the x-axis of the created local coordinate system to achieve the loading motion.

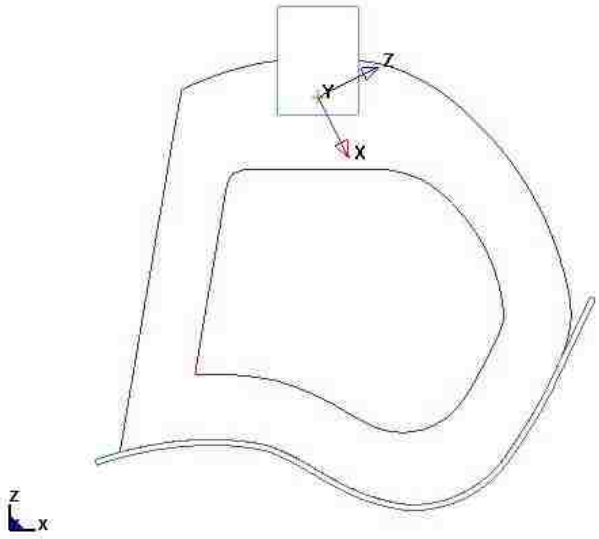

Figure 54. Local coordinate system created for the vector of loading direction (positive x vector as the loading direction).

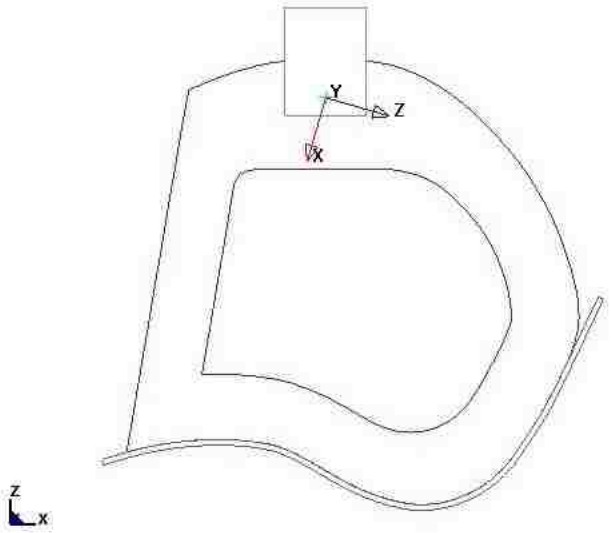

Figure 55. Local coordinate system created for the vector of loading direction (positive x vector as the loading direction).

The minimum simulation time was determined to be 100 ms with the simulation being proceeded in fully implicit mode. After numerous iterations of the simulation with both implicit and explicit solvers, the implicit solver was chosen due to its significant advantage on saving computational time without losing any detail of dynamic effect. The implicit mode allowed the simulation to run in larger time steps (0.5 ms) than that of the explicit mode (3.80E-04 ms) for the forward-facing loading condition. As a result, the simulation took 6300 seconds to complete for the implicit mode and 42600 seconds to complete for the explicit mode. "IMASS" was set to "1" in the simulation to include calculation for dynamic effect.

All contacts in this simulation, the contact between Part 1 and Part 2 as well as the contact between Part 1 and Part 3, are controlled by the segment-based surface to surface contact algorithm (CONTACT_SURFACE_TO_SURFACE) in LS-DYNA. This contact algorithm was chosen after testing all combinations of feasible contact algorithms due to its ability to allow the implicit solver to reach calculation

equilibrium at each time step which lead to the success of completing the simulation. Appropriate values of the static and dynamic coefficient of friction were determined to be 0.30 and 0.20, respectively, after iterations of contact testing.

The loading characteristics were defined by "DEFINE_CURVE" as a ramp that starts at 0 N and ends at 1.78 kN. The entire loading process was completed in 100 ms where as load ramp was applied from 0 to 90 ms. In the last 10 ms, load was held constant at the maximum value. There are two advantages of constant load in the last 10 ms. First, it can verify whether or not the device material has yielded. For example, if the peak load has caused the material to yield, the stress level will continue to increase in the last 10 ms even if the load is held constant. Secondly, the constant loading in the last 10 ms can verify the stability of the system, which means the stress level should not fluctuate within that period of time. Instability in the system can indicate slippage in the system, which should be avoided for the system.

8.3 Forward-facing Test Results

8.3.1 Energy Balance

It is important to evaluate energy balance for the simulation results to ensure all energy levels trended in a realistic ways compared to the graphical presentation in LS-DYNA. Figure 56 showed finalized energy balance for the forward-facing configuration.

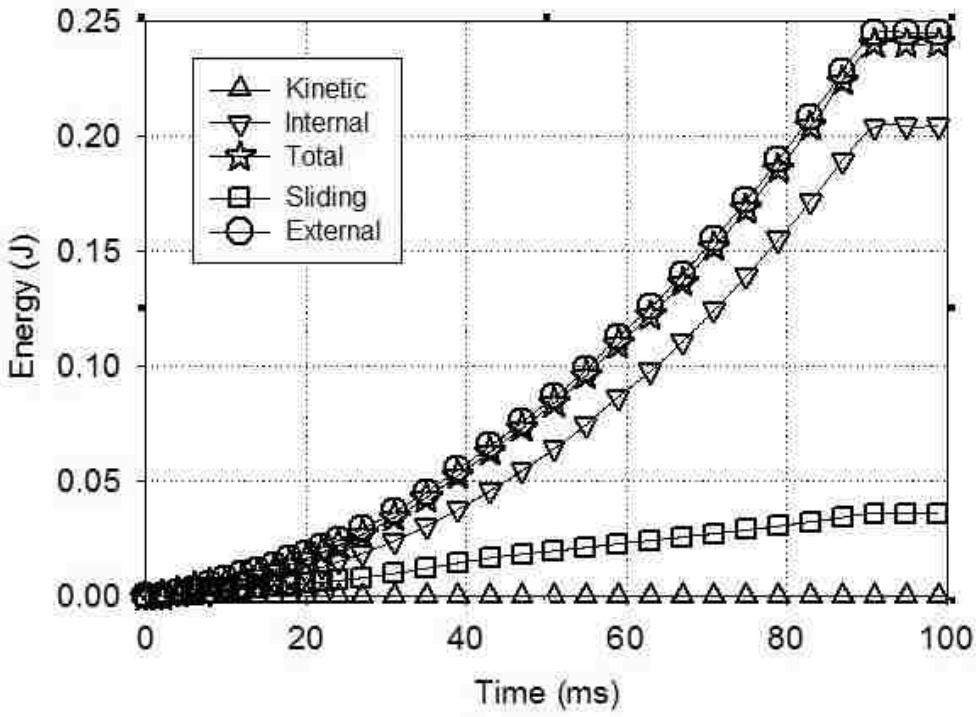

Figure 56. Energy balance for forward-facing configuration simulation (implicit approach).

Looking at the energy balance plot, majority of the total energy has been indicated as internal energy, which matched the actual loading situation. The sliding energy is also present in an increasing trend towards the 90 ms point where load was held constantly. No negative sliding energy was found in the simulation, which indicated good contact among all the entities in the simulation.

Rate of increasing of energy level starts to decrease at 90 ms time because the load was held constant from that point. From the 90 ms point on, there was increase in the energy level which indicates the material did not yield. The kinetic energy level is not significant from Figure 56 so that minimum dynamic effect was present to the simulation as expected earlier. The low kinetic energy level is a good indication of the simulation being quasi-static.

Looking at results from the explicit approach, which is shown in Figure 57, the energy level of the internal energy is similar to the implicit approach (Figure 56) but the total energy is not as close to the external work compared to the implicit energy results. With the better energy ratio and tremendous advantage on the computational time, the implicit approach had become the obvious choice to process all further virtual testing events from this point.

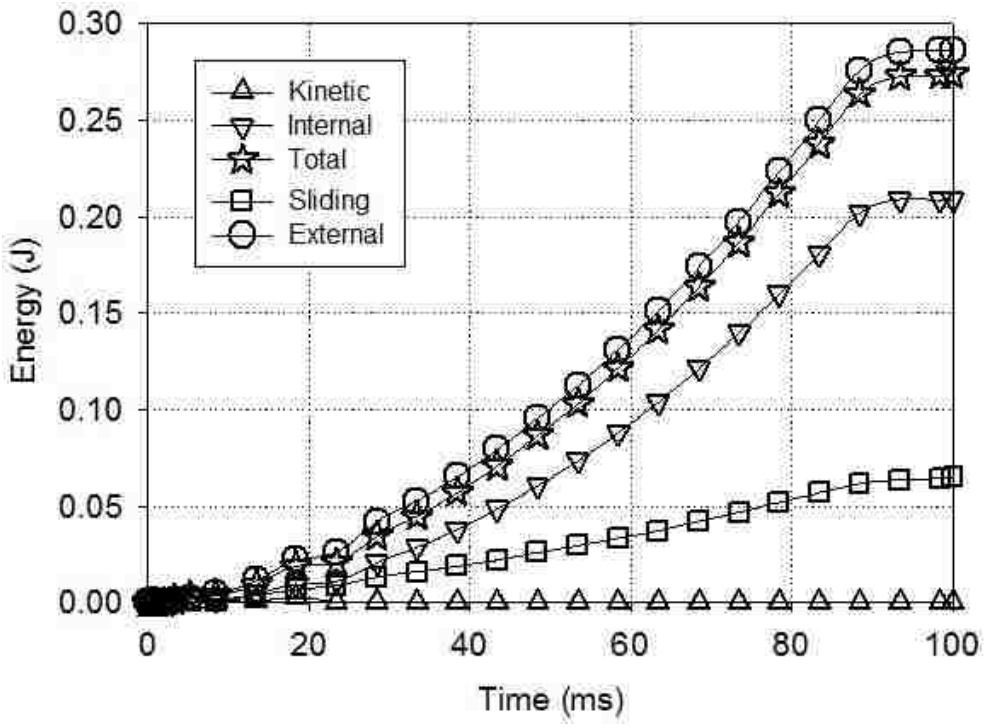

Figure 57. Energy balance for forward-facing configuration simulation (explicit approach).

8.3.2 Contact Interface Forces

Contact interface forces for the contact interfaces were plotted as shown in Figure 58 below. Both the resultant forces for contact 1 and 2 are matching with a

maximum loading value of 1.78 kN, which satisfied the design loading specification.

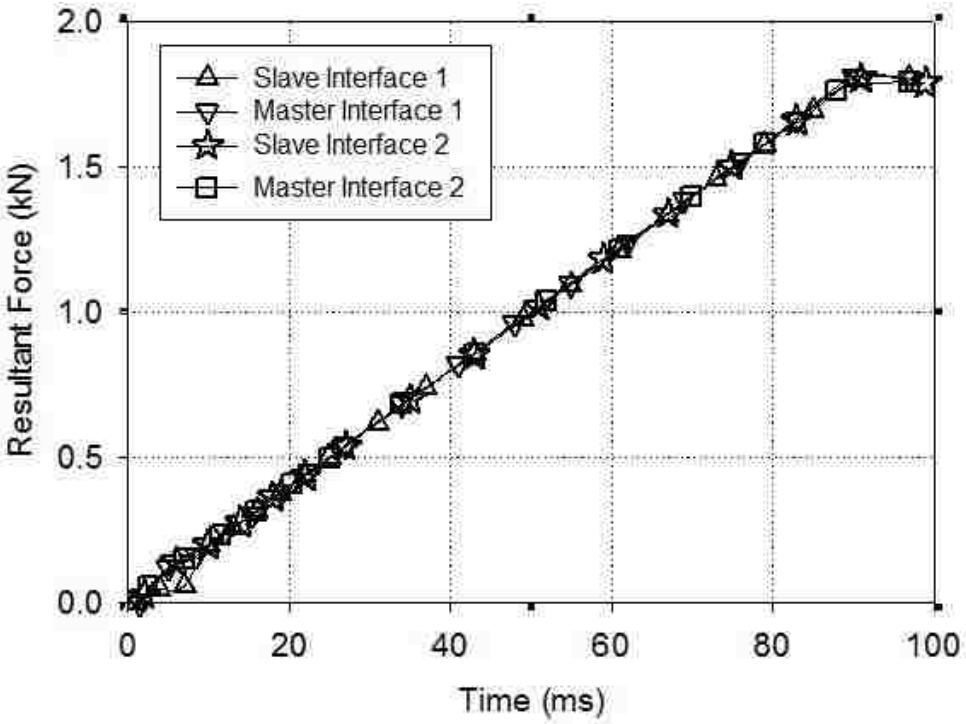

Figure 58. Force summary of the contact interfaces.

8.3.3 Stress Comparison

Since the wood orientation coordinate system was defined, stressed in different directions can be clearly identified by Von Misses Criterion in LS-PrePost. For example, the parallel wood fibre orientation is laid in x and z axis direction in the global coordinate system in the simulation. The perpendicular wood fibre orientation is laid along y-axis.

The maximum tensile and compression stresses in parallel wood orientation can be identified in 1st and 3rd principal stresses, which laid in in x-axis and z-axis in the global coordinate system in the simulation. Similarly, the maximum tensile and compression stresses in perpendicular wood orientation can be identified in 2nd

principal stress, which laid in y-axis in the same coordinate system. The shear stresses were identified in x-z and y-z planes.

From the above observation approach, all stresses at maximum load (1.78 kN) were found to be below their corresponding yield strengths as shown in Table 14. In some directions, the stress levels were well below the yield strengths.

Test Type and Direction to Fibre	Stress at Max Loading (MPa)	Yield Strength (MPa)
Tensile In Parallel	3.576	17.638
Compression In Parallel	3.135	29.818
Tensile In Perpendicular	0.218	0.327
Compression In Perpendicular	1.537	11.546
Shear In Parallel	0.952	5.490
Shear In Perpendicular	0.813	3.137

Table 14. Stress levels for forward-facing configuration simulation compared to yield strengths.

8.4 Rearward Facing Configuration

The rearward facing configuration simulation was conducted with the all the same conditions as the forward facing configuration except for the loading direction to the loading beam.

8.4.1 Energy Balance

Overall, energy levels in rearward configuration appeared to be higher than forward configuration as shown in Figure 59. The majority of the total energy

appeared to be internal energy, which is consistent as the results from 8.3.1. The sliding energy is also present in an increasing fashion towards the 90 ms point of simulation, which indicates no negative sliding energy was found.

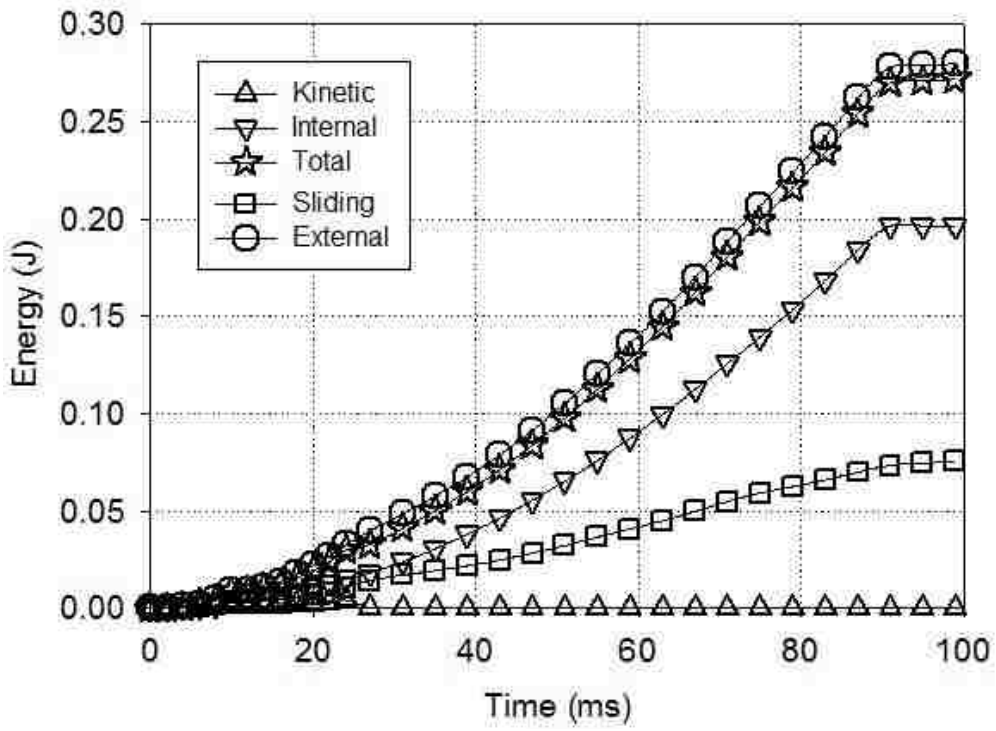

Figure 59. Energy balance for rearward-facing configuration simulation (implicit approach).

No rate of energy increasing was found after 90 ms point, which indicated that the material on the CRSIAD did not yield. The kinetic energy is not significant in rearward-facing configuration just like the forward-facing configuration.

8.4.2 Contact Interface Forces

Contact interface forces are consistent to the results from Section 8.3.2 with a maximum load of 1.78 kN, which meets the design loading specification.

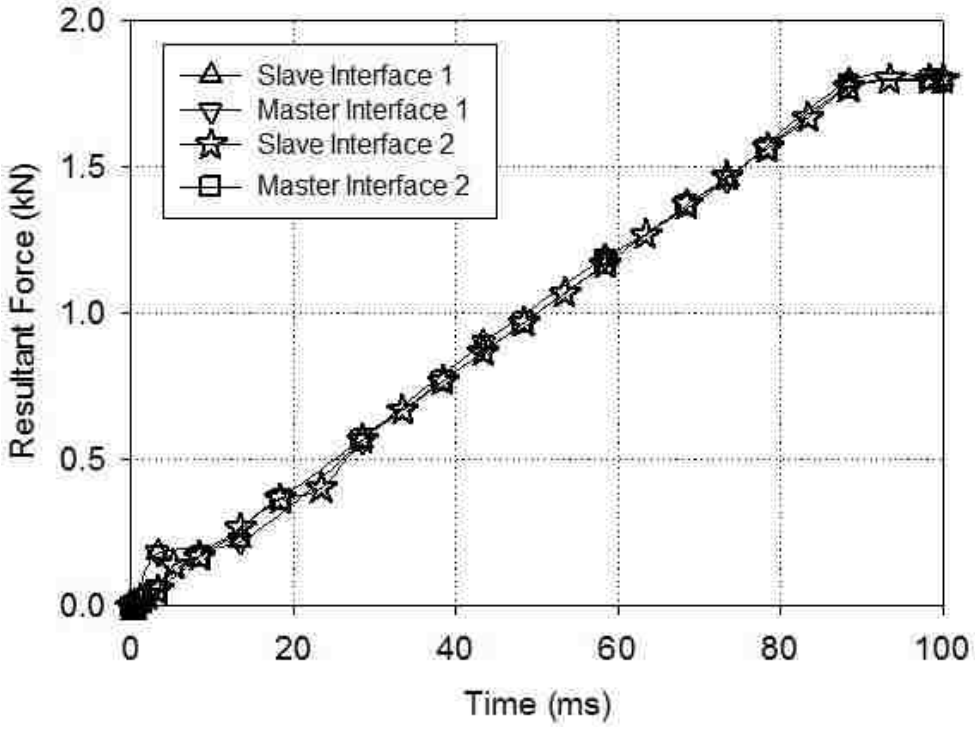

Figure 60. Force summary of the contact interfaces

8.4.3 Stress Comparison

Since the geometry and material properties did not change from forward-facing configuration scenario, stress levels are identified in the same fashion as Section 8.3.3.

From the observation for rearward facing configuration simulation results, all stresses at maximum load (1.78 kN) were found to be below their corresponding yield strengths as shown in Table 15. These results have ensured that the device main body would not yield under the maximum loading condition.

Test Type and Direction to the Fibre	Stress at Max Loading (MPa)	Yield Strength (MPa)
Tensile In Parallel	3.368	17.638
Compression In Parallel	1.553	29.818
Tensile In Perpendicular	0.279	0.327
Compression In Perpendicular	1.556	11.546
Shear In Parallel	1.152	5.490
Shear In Perpendicular	0.931	3.137

Table 15. Stress levels for rearward-facing configuration simulation compared to yield strengths.

9 CRSIAD MANUFACTURING

9.1 Device Assembly Design

The simulation results from the previous section have suggested that the geometry developed from Section 4.4.5 is ready to be manufactured with the given material. The manufacturing process of the entire CRSIAD assembly is covered in this section.

9.1.1 Device Main Frame Packaging

The main body of the CRSIAD as shown in Figure 61 was constructed in CATIA as an assembly of Parts A to F. Due to orthotropic characteristics of the material, this assembly needed to be fabricated according to the local coordinate system (AOPT) defined from the simulation in Section 8.2. By breaking up the main body of the CRSIAD into smaller parts (Parts A to F), it was feasible and versatile to fabricate each individual part to match the specific orientation.

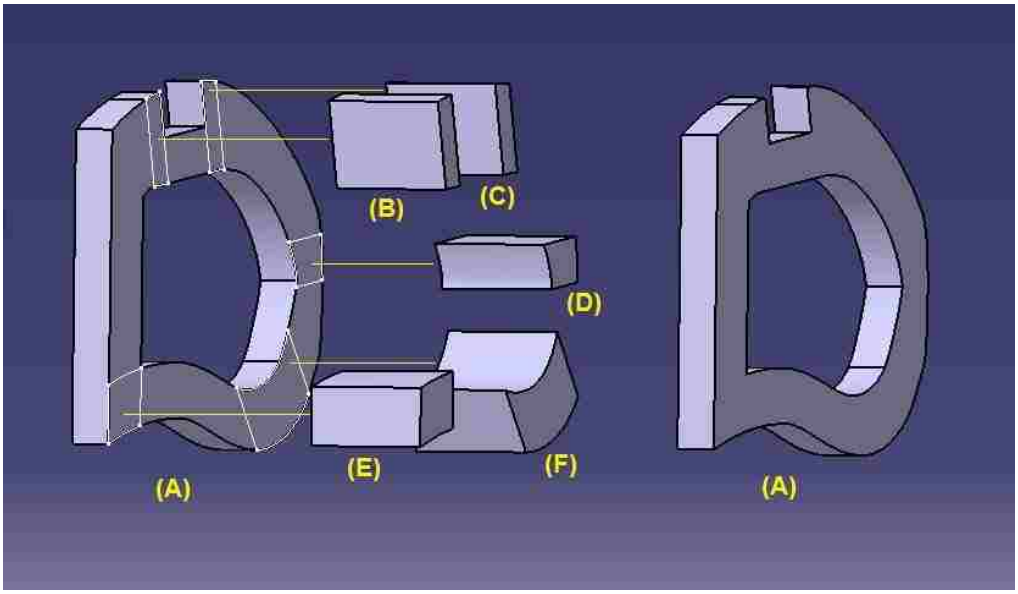

Figure 61. Assembly diagram for the main body of the CRSIAD.

9.1.2 Upper Loading Beam Design

The loading beam as shown in Figure 62 was easily constructed in CATIA with its parallel wood fibre orientation in the vertical direction.

To install the D-rings to the end-face of the beam, an aluminum plate were used as a media between the D ring and the beam as shown in Figure 62. Since the loading motion of the beam was simulated at the maximum load of 1.78 kN, aluminum plates with a thickness of 3.175 mm were considered to be sufficient for this application, which was verified in the further testing.

The force acting on the D-rings should transfer minimum to none rotational motion to the loading beam because the beam must press the CRSIAD appropriately in a linear motion towards the lower anchor locations of the CRS. Therefore, it was important to apply a method of mounting the plates to the beam that would not potentially create moment on the beam. Gluing the aluminum plates to the wood beam would not create excessive moment on the beam but the glue will not sustain so many loading cycles on the beam during the service life of the CRSIAD. Therefore, additional reinforcement was needed from external hardware kit to the system. After exhausting attainable options of hardware kits in the market, a barrel nut (Part J) as shown in Figure 62 was found useful to help mounting the side plate with two fasteners to secure it, which has minimum effect of adding extra moment to the existing system.

The bottom hole on the side plate (Part H) is the mounting hole for the D-ring (Part I), which is the pivot points of the D-ring. To ensure smooth rotation of the D-ring, a metal sleeve (Part M) was inserted into the pivot point of the D-ring. The D-ring was then fastened onto the side plate by bolt (Part O), nut (Part L) and shims (Part N) with no slack or preload.

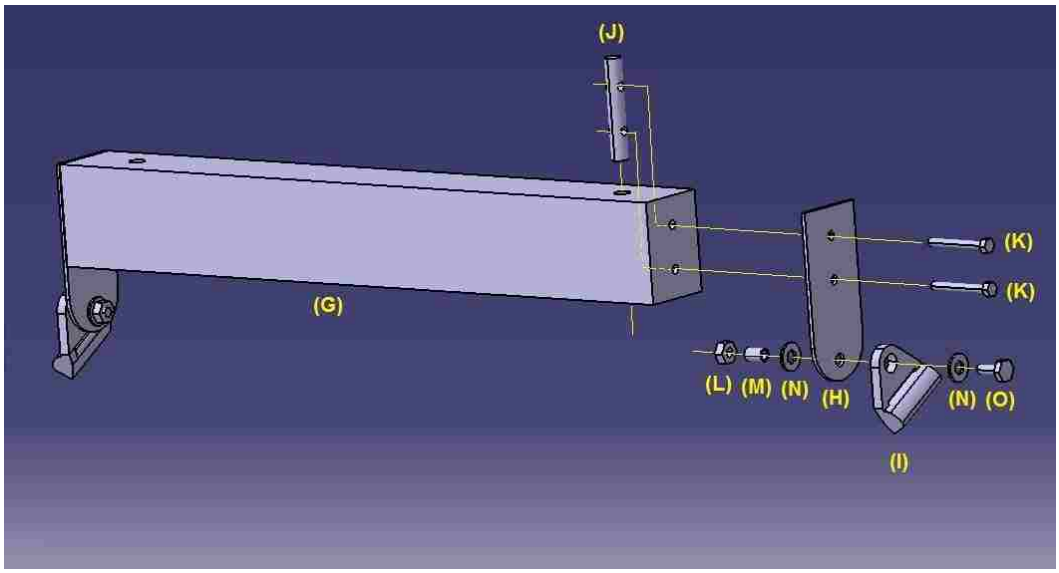

Figure 62. The loading beam assembly design of the CRSIAD.

9.1.3 Loading Mechanism

As discussed in Section 4.4.2, a ratchet strap with special attachments was used as the tightening mechanism for applying load to the D-rings on the loading beam. All the parts within this mechanism were purchased from the stores and car dealerships and no drawing is available for these components.

9.2 Component Fabrication

9.2.1 Fabrication of the Device Main Frame

Part A from Figure 61 was made by first gluing two sheets of the given plywood together to achieve the desired thickness. The glued sheet was then cut by computer numeric control (CNC) machine in a local machine shop. Two pieces of Part A were fabricated for this assembly with one on each side. Parts B and C were cut from one sheet of plywood with thickness of 19.05 mm then trimmed according to

the drawing on a milling machine. Parts E, F, and G were all made in similar fashion as Part A.

Parts A to F were then glued together with wood glue as shown in Figure 61. Each bonding surface in Figure 61 was reinforced by two wood nails.

9.2.2 Fabrication of the Loading Beam

The thickness of the loading beam was achieved by gluing three sheets of the given plywood together. The beam was then cut to its appropriate dimensions according to the drawing from CATIA. The beam was placed with its wood fibre direction being parallel to the vertical direction in order to match the wood fibre orientation described in Section 9.1.2.

Aluminum plates, having a thickness of 0.125 inch (Part H in Figure 62), were cut with a CNC machine in the machine shop on the campus (University of Windsor). Holes had to be drilled on the loading beam for the barrel nuts (Part M) to slide in place. The barrel nuts were then fastened by the bolts (Part O) to secure the side plate (Part H). The sleeve (Part M) was cut from an appropriately sized tubing to match the inner diameter of the eye of the D-ring, which is 14 mm. The bolts (Part K) were obtained according to the inner diameter of the sleeve, which is 9 mm. Bolts were hand-torqued with spring-locking washers applied in-between. Free movement of D-rings for rotation was checked and additionally ground to the sleeve insert to ensure smooth rotation of the D-ring.

9.2.3 Assembling the Loading Mechanism

The ratchet assembly and webbing were obtained from local hardware stores. The loading capacity of the strap is 2.2 kN whereas ratchet is rated at 6.7 kN respectively.

As described earlier in Section 4.4.4, the system design requires the end attachments of the webbing to be clipped into the existing car seatbelt system. Therefore, compatibility of end clips and buckles for the seatbelt system needed to be verified before acquiring the relevant components.

Unfortunately, seatbelt clips and buckles vary across different car manufacturers so that no universal part was available to be used for the design of the loading mechanism of the CRSIAD. Due to the variety of the clips and buckles, a survey was conducted to study the differences among the existing types of clips and buckles for majority of the production vehicles in the market.

After a preliminary inspection in five random vehicles from different manufacturers, two different types of clip and buckle combinations were identified. An assumption was made that the majority of cars in the market contain these two types of clip and buckle combinations (Combination "A" and "D" in Figure 63). Therefore, these two sets of clips and buckles were purchased from the local car dealers for further compatibility check.

Figure 63. Four seatbelt clip and buckle combination A, B, C and D.

The Types A and D clip and buckle combinations were tested on over 30 attainable vehicles in the city. A problem found during the compatibility check was that some of these clips did not fit into some buckles in the test cars even if they seemed to be in matching sizes. In fact, more than two types of clip and buckle combinations were identified in the tested vehicles. The results from the survey, which are available in Table 18 in Section Appendix A, have indicated that four different types of seatbelt clip and buckle combinations exist (as shown in Figure 63).

Attaching all four sets of clips and buckles onto the ratchet webbing of the CRSIAD is simple to implement on the production of the CRSIAD. However, the amount of clips and buckles will become confusing and redundant for the users to install the CRSIAD. With further investigation and testing on the four types of combinations, a solution was found to address this issue. Although the short male end ("D" male) did not match the long female end ("C" female), the long male ("C" male) end matched the short female end ("D" female). Since the short male end ("D" male) and the short female end ("D" female) were already a match, the short female end ("D" female) can serve the purpose of matching both short and long male ends. The same approach was applied to the male end that the long male end can match both the long and short female ends. Therefore, the quantity of the clip and buckle combinations was reduced to half of the originally required quantity. the long clip and the short buckle for each type of combination ("A" male with "B" female, "C" male with "D" female) were chosen to be installed on the tightening mechanism of the CRSIAD.

The selected clips and buckles were then attached to the ratchet webbing as shown in Figure 64. The webbing, originally served as car seatbelt webbing, has a maximum loading capacity of 4000 lb of weight which is ten times of the maximum load to be applied to the CRSIAD. The webbing was stitched and assembled as shown in Figure 64 based on the pattern in the assembly drawing from Figure 18 in

Section 4.4.5. The stitching was completed at Spartan Sling Manufacturing Inc. in Windsor, Ontario.

Figure 64. Stitched webbing with selected seatbelt attachments.

9.3 Complete Assembly

With all three main components assembled, the entire CRSIAD was assembled according to the assembly in Figure 20 from Section 4.4.5. The complete assembly of the CRSIAD is shown in Figure 65 from Section 10.1.2.

10. The CRSIAD TESTING AND FINALIZATION

10.1 Forward-facing Configuration Testing Setup

10.1.1 Test Equipment

The CRS model used in this testing event was Graco Comfort Convertible. The vehicle used for the test was a 2015 Dodge Grand Caravan. The specimen was the complete assembly of the CRSIAD.

10.1.2 Test Setup

The first test setup was completed in the following steps. Due to later design changes, there were subsequent changes made on the setup steps which are explained throughout Section 10.3 (Design Iterations). A finalized setup procedure is available in Section 10.3.5 for the final version of the CRSIAD.

1. Prepare the CRS according to standard CRS installation procedures [4]. Place the CRS on either side of the rear seat on the vehicle.

2. Attach the LATCH and top tether clips according to standard CRS installation procedures [4].

3. Apply H-clip to the vehicle seatbelt on the outboard side (as explained in Section 4.1.4). Ensure seatbelt clip is sitting at as low position as possible and yet unable to extend with any pulling force.

4. Prepare the CRSIAD into the configuration as shown in Figure 65.

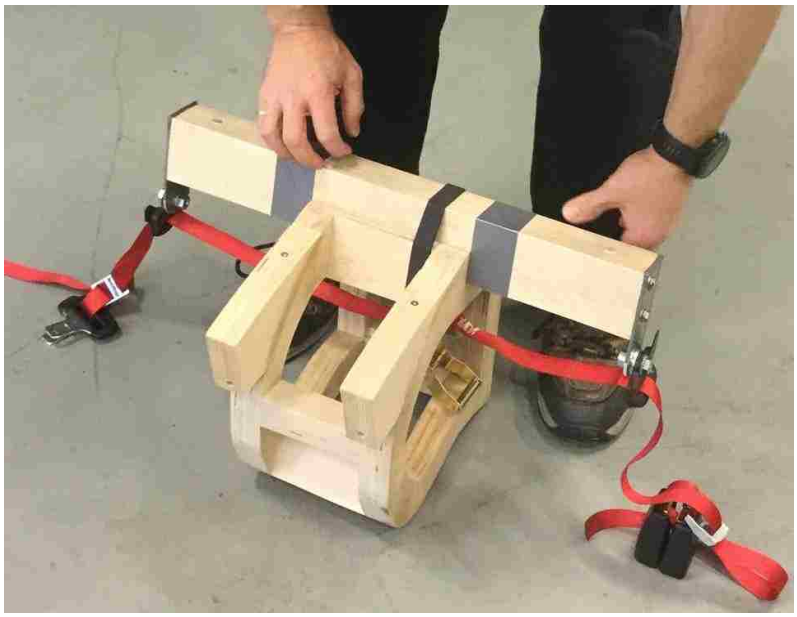

Figure 65. The preparation setup for the CRSIAD before it was loaded onto the CRS.

5. Set the clip and buckle from the ratchet webbing into a matching pattern as vehicle seatbelt system. Ensure the ratchet is in engaged position with no excessive webbing coils in it. If there is excessive coiling, disengage the ratchet and release coiling by pulling webbing out of the ratchet.

6. Place the CRSIAD on the top of the CRS with the side marked "FRONT" facing towards the installer.

7. Attach the clip and buckle of the ratchet webbing of the CRSIAD to the corresponding vehicle buckle and clip of the seatbelt system.

8. Complete the setup as shown in Figure 66. The CRSIAD is ready to be used by applying the ratchet.

9. Apply the ratchet to load the CRSIAD into the CRS while feeling the slack between the CRS and car seat cushion. Keep applying the ratchet until the slack is less than one inch in any direction between the CRS and the car seat.

10. With the CRS appropriately preloaded by the CRSIAD, tighten the CRS by pulling the lower anchor webbing until it can no longer extend.

11. Release the CRSIAD by disengaging the ratchet and release webbing.

12. Remove the CRSIAD out of the CRS and installation is now complete.

Figure 66. Forward-facing Configuration Preliminary Test Setup for the CRSIAD.

10.2 Rearward-facing Configuration Setup

10.2.1 Test Equipment

All the test equipment were identical to that listed in Section 10.1.1.

10.2.2 Test Setup

All the steps for setting up the CRSIAD are identical to those in Section 10.1.2 except for the orientation of placing the CRS. The CRS was placed in a rearward-facing configuration as shown in Figure 67 as opposed to the forward-facing configuration in Figure 66.

Figure 67. The Rearward-facing Configuration Preliminary Test Setup for the CRSIAD.

10.3 Design Iterations and Revision

There were in total five design iterations completed for the CRSIAD before the CRSIAD was further reviewed by child safety professionals. Details of all changes are described in the following sections.

10.3.1 Iteration One

The first test of the CRSIAD had proved its functionality and feasibility. The installer was able to preload the CRSIAD into the CRS by operating the ratchet to an extent. However, the goal of achieving the preload of the CRS was not achieved and therefore test was incomplete.

The first issue found during the test was the ratchet assembly size. The ratchet size was found to be too large and inconvenient for this application. Although the

ratchet was able to fit between the CRS and seatbelt buckle, operating it within the tight space was cumbersome. Setting and releasing the ratchet requires pivoting the ratchet handle and the handle was too large to be conveniently operated within the space. The ratchet in this size was also heavy for manipulation.

The second issue that arose was the clearance between the ratchet and D-ring. As the ratchet was operating, the CRSIAD was forced and loaded into the car seat. As the CRSIAD was being lowered, the distance between the D-ring and ratchet became shorter so that the ratchet was in contact with the D-ring before adequate tightening was completed.

The original reason for choosing the ratchet in this size was to match the provided webbing. However, such a high rate of loading capacity was not necessary for the application of the CRSIAD. After searching in the hardware stores, the size of 2.2 kN ratchet and webbing combination was found to be reasonable compared to the original 6.7 kN ratchet as shown in Figure 80. The new ratchet would allow significantly more space for the hand to operate the ratchet within the tight space. The new loading capacity, 2.2 kN, is still sufficient for the application of the CRSIAD (maximum load at 1.8 kN). The down-sized ratchet and webbing were then purchased from the store. The webbing was stitched in the same fashion as described in the previous section. The ratchet and webbing were then assembled for the next test.

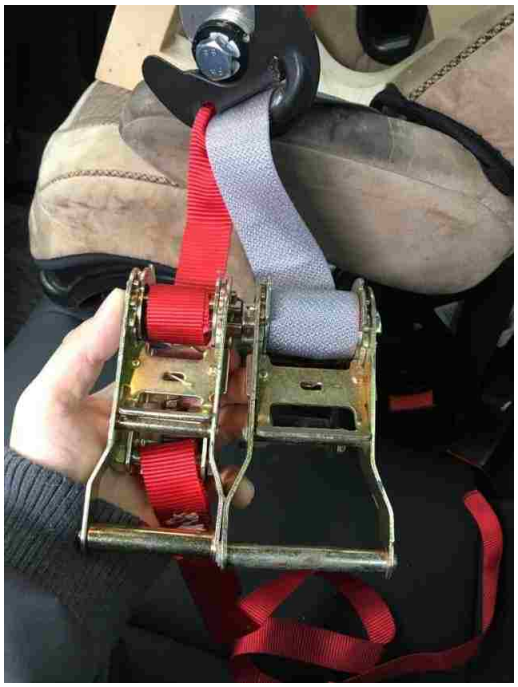

Figure 68. A comparison between the new ratchet (left) and the original ratchet (right) in terms of size and webbing.

10.3.2 Iteration Two

The down-sized ratchet and webbing assembly was found to be much more usable than the original size. Since the handle was smaller, operating the ratchet was a lot easier than the last test so that the tightening process was more efficient. The CRS was successfully preloaded with the aid of the CRSIAD.

With the comparatively smaller-sized webbing, a new issue arose with the D-ring: Since the D-ring was originally designed for car seatbelt webbing, which is wider in size, the smaller webbing was buckled up and stuck at the end of the D-ring slot during the installation as shown in Figure 69.

Figure 69. The downsized webbing stuck at the corner of D-ring slot while under tension.

D-rings are uniquely made parts for standard car seatbelt systems. It was not feasible to source a D-ring with a narrower slot than the standard size at the time. In order to address such an issue, the option was to modify the existing D-rings by shortening their slot width.

The D-ring slot ends were filled with heavy-duty outdoor silicon leaving the available width to match the width of the webbing as shown in Figure 70. The silicon was dried and cued overnight before the installation of the webbing. One main advantage of using silicon was that it is in solid state when dry and still soft enough to protect the fabric webbing from scoring.

A **B**

Figure 70. Webbing in the D-ring with slack (A) and with no slack after silicone stuffed at the slot ends (B).

An alignment issue during the loading process was identified in this test and needed to be addressed. Since the ratchet was located on one side of the CRS, the CRSIAD was leaning towards that side while the ratchet was operated. Although the D-rings are designed to minimize friction to the webbing that ran through them, the summation friction on the ratchet side had to be higher than the other side. The D-ring at the ratchet side sustained a locally downward pulling force of the ratchet . This caused more friction than in the D-ring without a ratchet on the opposite side. Therefore, the bias of the friction needed to be mitigated to prevent the CRSIAD from tilting during the installation.

The resolution was to install the ratchet on the centre location under the loading beam so that loads can be spread more evenly on both sides of the beam as shown in Figure 71. As a result, the ratchet webbing was modified and stitched again to cooperate with the change of the system.

Figure 71. The CRSIAD setup with center-mounted ratchet.

10.3.3 Iteration Three

The centre-mounted ratchet was effective in resolving the alignment predicament. While the ratchet was operated, both left and right sides of the CRSIAD were loaded into the CRS. Since no tilting of the main structure was found, the centralized ratchet design was successful and therefore remained for the rest of the testing process.

Inconvenience was identified on the loading beam when the beam had to be rotated for a vehicle with different seatbelt system configurations. Different vehicles have a different seatbelt clip and buckle setup. The seatbelt buckle can be located on the inboard or outboard side of the backseat. When the CRSIAD was configured in an opposite fashion so the male clip on the ratchet assembly was on the same side as the seatbelt male clip, the ratchet assembly and its end attachments had to be re-configured into an inverted setup for appropriate installation. This

would require either re-configuring the entire ratchet webbing or rotating the entire loading beam assembly by 180 degrees in order to match the correct clip and buckle pattern on the vehicle. Both of the methods require physical effort to implement.

After searching for solutions, a convenient resolution was to have detachable and adjustable ratchet webbing end attachments. If the male and female attachments could be removed from the ratchet assembly and switched directly, neither the ratchet assembly nor the loading beam assembly would need to be re-configured. The steel adjustable clips were found from a local hardware store as shown in Figure 72. These clips have the correct width for the ratchet webbing to run through and their loading capacity is 1.3 kN per unit. With two of the adjustable clips used in series, 2.6 kN was the theoretical loading capacity which exceeded the design target of 1.8 kN. Modifying the webbing end also required modifying the webbings so the webbings were modified and stitched again.

Figure 72. The steel adjustable clip applied to the ratchet webbing.

A complete assembly after applying detachable webbing end clips is shown in Figure 73. The adjustable clips were fitted next to the female seatbelt buckle (left) and male seatbelt clip (right) in Figure 73.

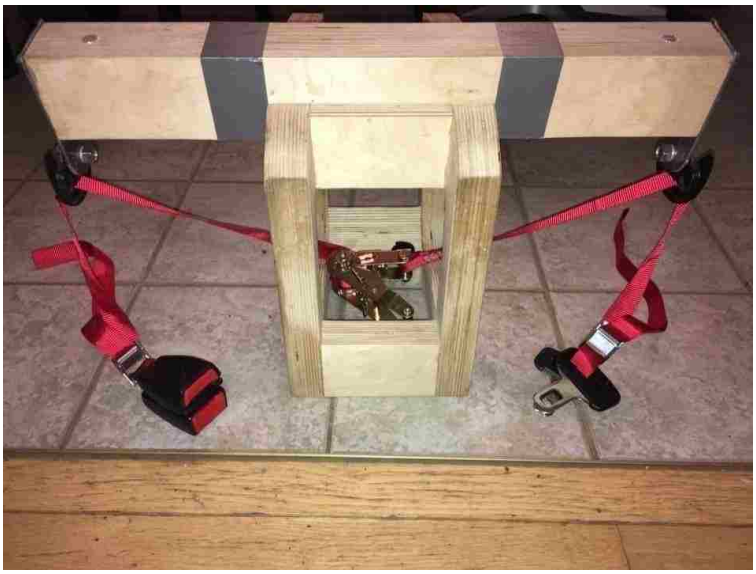

Figure 73. The complete assembly with adjustable clips installed on the ratchet webbing.

10.3.4 Iteration Four

In the last test, a major fitment issue was identified after testing the CRSIAD on a different model CRS, which had lead to further modification on the geometry of the CRSIAD.

The tested CRS was the Eddie Bauer Alpha Elite Convertible model. Although its functionalities are identical to the previously tested model of CRS (Graco Comfort Convertible), there is a key distinction in the routing of the lower anchor strap. The different loading locations for the lower anchor strap between the two CRSs are shown in Figure 74 below.

Figure 74. Difference on the lower anchor strap routing location between two CRSs (Graco Comfort Convertible on the left and Eddie Bauer Alpha Elite on the right) pointed with red arrows.

On the Graco Comfort Convertible model, the lower anchor strap runs off the edge that is located on a separate plane of seating structure. On the Eddie Bauer Alpha Elite model, the lower anchor strap is routed at the lower back location of the seating area behind the fabric. The only component that is separating the occupant or, in this case, the CRSIAD is the fabric. This means after the CRSIAD was set up and loaded into the CRS, the lower back section of CRSIAD was in contact with the lower back section of the CRS seating structure where the lower anchor strap is run across. Since the CRSIAD was securely loaded into the CRS, the jammed lower anchor strap of the CRS could not be further tightened by hand to complete the CRS installation. Such conflict zone on the CRSIAD geometry is shown in a close-up view in Figure 75 (A).

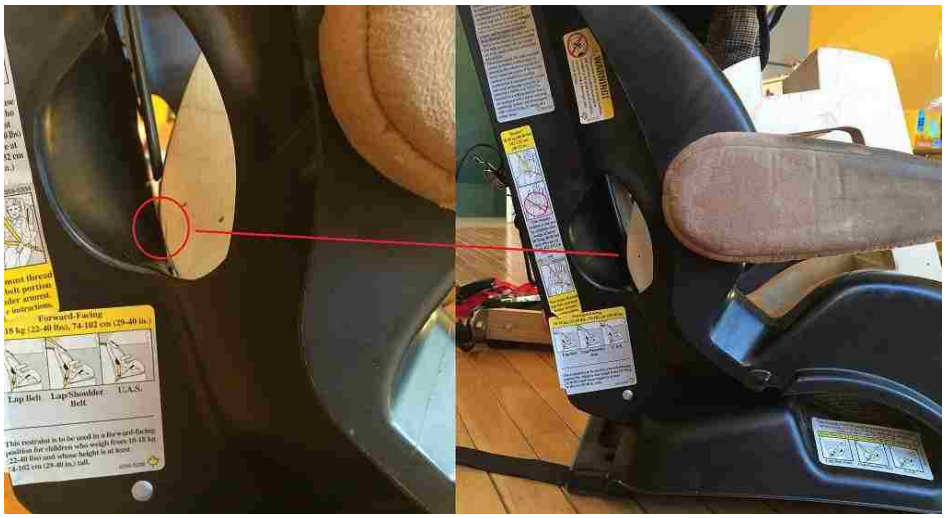

A **B**

Figure 75. The section on the CRS in contact (circled red) with the CRS (Eddie Bauer Alpha Elite) as geometry conflicted zone.

At this point, a survey for the existing CRSs in terms of the lower anchor strap routing location was needed to determine how many CRSs currently in the market have the identical setup as the one in question.

Another visit to Toys'R'Us had revealed sixteen out of twenty-four models of CRSs featured a geometry with lower anchor strap routing similar to the Eddie Bauer Alpha Elite model. Due to the great percentage of such CRSs exist in the market, a design change was necessary on the geometry of the CRSIAD.

The solution to this problem started with an idea of reducing material of the existing main frame of the CRSIAD to clear the conflict zone mentioned earlier in this section. A template that replicates the exact side profile of the main frame was made out of card board in order to troubleshoot the problem. The template was placed vertically onto the contour of the seating area of the Eddie Bauer Alpha Elite in the same orientation as how the CRSIAD was seated. As expected, the template

had the exact conflict zone as the CRSIAD with the CRS. The conflict zone on the template was then trimmed with trial and error until no contact was present at the conflict zone as shown in Figure 76 (A). A close up picture of the conflict zone when the template was appropriately seated on the Eddie Bauer Alpha Elite is shown in Figure 76 (B). The clearance between the template and the CRS at the conflict zone was measured to be 12.7 mm.

A **B**

Figure 76. Exact-traced template on the left with conflicted section trimmed out (pointed by red arrow); actual fitment on the CRS on the right to show clearance as a result of the trimming the conflicted section (pointed by red arrow).

The successful trial with the modified template has proved that removing material is a useful method to clear the conflict area between the CRSIAD and CRS as mentioned above. Two aspects of geometry modification were considered for addressing the issue: First, adequate amount of material had to be removed to clear the conflict area between the CRSIAD and CRS. Secondly, any potential issues associated with the removal of the material needed to be avoided.

The amount of material removed from of the template, subsequently the CRSIAD, seemed feasible for resolving the conflict issue with the Eddie Bauer Alpha Elite model of CRS but may not be sufficient for other CRS models in the market. Therefore, after trying the template with more CRS models in the store, further material from the template was removed to ensure the solution is universal.

The removal of the material on the CRSIAD would lead to less structural support on the lower back section of the CRSIAD from the CRS. Assume the CRSIAD was operated and loaded in a forward-facing configuration of CRS, the moving direction of the CRSIAD allows itself to roll into the section that was removed and potentially create contact again with the lower anchor webbing across the CRS (Eddie Bauer Alpha Elite model). In that case, additional material needed to be added to the CRSIAD to prevent such rolling effect while maintaining adequate structural support to the CRS.

The geometry was then created to fulfill the above two requirements as shown in Figure 90. The red arrow is pointing to the section where material was removed to clear the potential conflict with the lower anchor strap. The yellow arrow is pointing to the addition of the material. The added section on the CRSIAD was created with smooth curves so that it can blend into the shape of the main frame of the CRSIAD to help with even stress distribution. The face marked in green in Figure 77 was created at a matching angle with the seat back of the CRS to ensure appropriate contact between this face and the CRS. At this point, the new geometry of the CRSIAD was ready to be virtually tested to verify the resolution to the conflict issue mentioned earlier in this section.

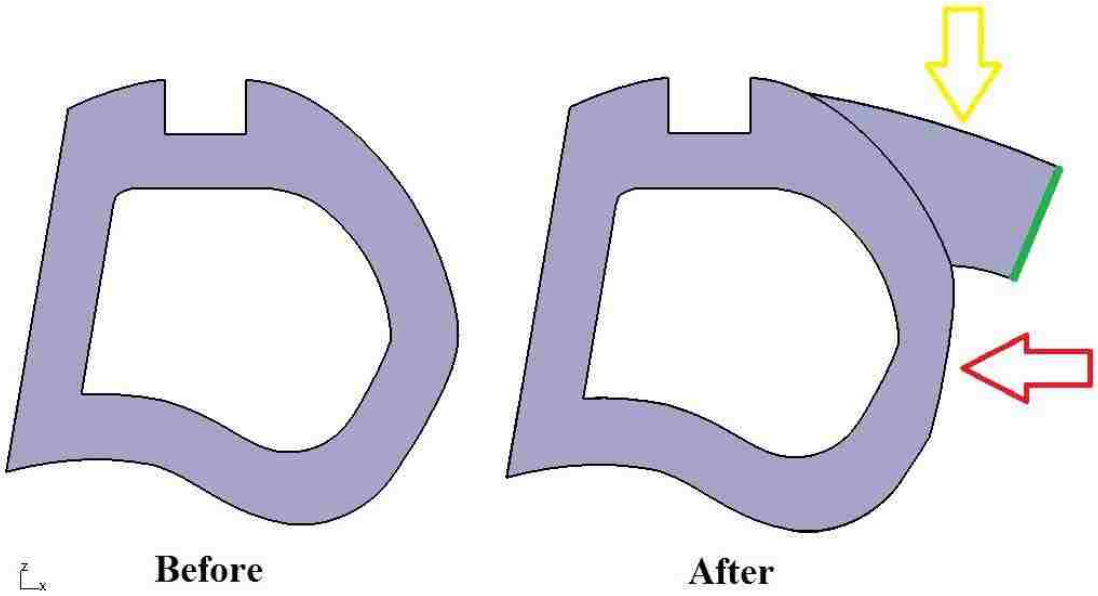

Figure 77. Modification completed on CATIA to show the added section (pointed by yellow arrow) and trimmed section (pointed by red arrow).

The new geometry was then imported into LS-DYNA for stress analysis. All the procedures used here are identical to Section 8.1. With the change on the geometry of the CRSIAD, new mesh had to be constructed for the simulation to be conducted. Due to the added sections to the geometry as described previously, triangular elements were used at the sharp corners near the boundary between the added sections and the existing geometry. Mesh quality check was performed as shown in Table 15 below. The triangular elements caused 0.108% of element violation for Jabobian and 0.036% of element violation for both the Minimum and Maximum Triangular Angles. Such small percentage of element violation was acceptable which was verified by the simulation results later in this section.

Quality Check Items	Minimum Value	Maximum Value	Number of Violated Elements (%)
Characteristic Length (mm)	1.2	5.66	0
Aspect Ratio	1	5.15	0
Skew (deg)	0	34.2	0
Warpage (deg)	0	0	0
Jacobian	0.457	1	3 (0.108%)
Minimum Quadratic Angle (deg)	55	90	0
Maximum Quadratic Angle (deg)	90	140	0
Minimum Triangular Angle (deg)	13.8	53	1 (0.036%)
Maximum Triangular Angle (deg)	65.4	123	1 (0.036%)

Table 16. Mesh quality check for the testing.

The new geometry of the CRSIAD assembly is shown in Figure 78 . Since the only change on this FEA model was the geometry, all other parameters and conditions were copied directly from the previously used key file (LS-DYNA).

Figure 78. Modified geometry of the CRSIAD with its mesh quality.

With the added material to the device, the weight of the main frame was increased by 0.193 kg, which brought the overall weight of the assembly to 5.014 kg excluding all the ratchet, webbing and clips.

The simulation was successfully conducted for both forward-facing and rearward-facing configurations of the CRS installation. The energy balance for both the forward-facing and rearward-facing configurations, as shown in Figure 79 and Figure 80, showed that total energy and external work are converged. The majority of the energy is still internal energy with a positively increasing sliding energy until the load was held constant at 90 ms.

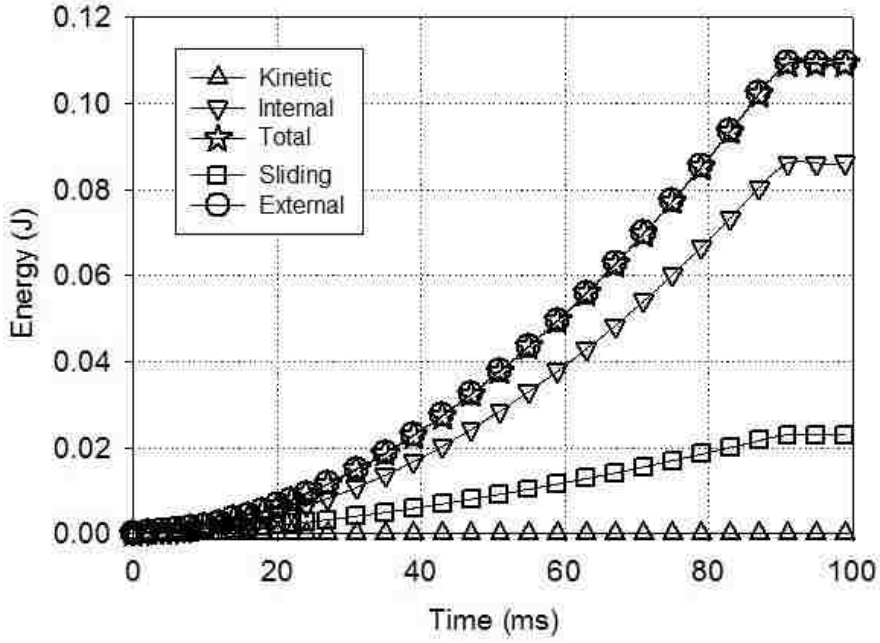

Figure 79. Energy balance for forward-facing configuration simulation (implicit approach) with modified geometry.

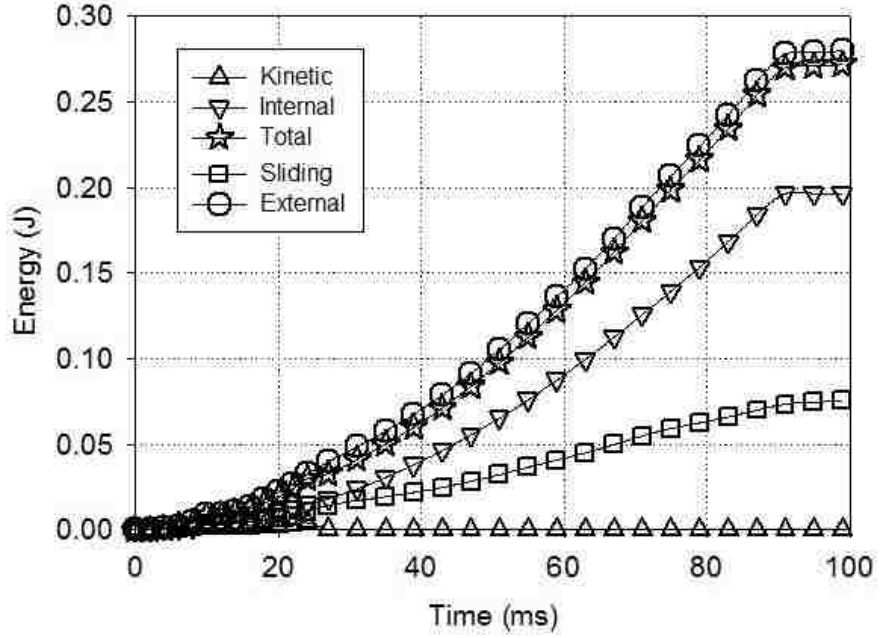

Figure 80. Energy balance for rearward-facing configuration simulation (implicit approach) with modified geometry.

By looking at the stress distribution on the device main frame by Von Misses Criterion in LS-PrePost at the maximum loading condition, the stress levels are shown in Table 17, the stress levels on forward-facing configuration are consistently lower than the previous results from Section 7.4.4 due to additional support from the added material on the structure of the CRSIAD. However, the stress levels for rearward-facing configuration remained close to previous results from Section 7.5.4 since the added material was not contributed to the loading condition in the rearward CRS configuration. With the stress levels confirmed to be within yield limits, the device was virtually verified to be ready for manufacturing.

Test Type in the Direction of Wood Fibre	Forward-facing Configuration Stress at Max Loading (MPa)	Rearward-facing Configuration Stress at Max Loading (MPa)	Material Yield Strength (MPa)
Tensile In Parallel	1.865	2.981	17.638
Compression In Parallel	2.650	3.979	29.818
Tensile In Perpendicular	0.131	0.168	0.327
Compression In Perpendicular	0.406	0.741	11.546
Shear In Parallel	0.679	0.672	5.490
Shear In Perpendicular	0.202	0.222	3.137

Table 17. Stress levels from both forward and rearward configuration simulation compared with material yield strengths.

The added sections to the CRSIAD were cut by CNC machine in the machine shop on campus (University of Windsor) and glued to the existing structure. Two reinforcement wood screws were installed on each of the added sections to the main frame of the CRSIAD to ensure a permanent bonding. The removal of the material was also completed according to the revised CATIA drawings, which are available in the "CAD" folder in the disc. The modified device main frame of the CRS is shown in Figure 81 as a comparison between the before and after states of the geometry.

A **B**

Figure 81. Original device main frame (A) and modified version (B).

The new device main frame was then placed back onto the Eddie Bauer Alpha Elite model of CRS to verify the fitment. As shown in Figure 82 (A), the clearance is measured to be 25.4 mm at the previously conflict area of the CRSIAD and the lower anchor strap of the CRS. Figure 82 (B) also shows how the back faces of the

added sections of the CRSIAD matched up with the seatback profile of the CRS. The modified main frame was then brought into the store again for verifying all the CRS models that previously had the clearance issue. None of the CRS models in the store was found to have the same issue again. With the remaining components unchanged (loading beam and ratchet assembly), the modified CRSIAD was ready to be tested for the next iteration.

A **B**

Figure 82. The modified CRSIAD fitment with the CRS model Eddie Bauer Alpha Elite with the conflicted zone (A) and seating with the additional wing sections (B).

10.3.5 Iteration Five

The testing of the latest CRSIAD assembly on the Eddie Bauer Alpha Elite model of CRS yielded successful results for both forward and rearward configurations of the CRS installation. The lower anchor strap of the CRS had no contact with the back portion of the CRSIAD when the CRS was fully preloaded by the CRSIAD. The geometry design of CRSIAD was considered complete at this point.

Further improvement was made on the ratchet on its easiness of manipulation. The ratchet had the tendency to sag due to gravity during the webbing adjustment so that it was difficult to keep the ratchet in the centre of the loading beam while the webbing was adjusted. Sometimes the ratchet had to be held by one hand while the other hand was adjusting the webbing, which was cumbersome in the tight space in the vehicle. Velcro strap was found useful to secure the ratchet onto the CRSIAD as shown in Figure 83. With the weight of the ratchet being supported by the velcro strap, operating the ratchet had become a lot easier as well as making adjustment to the webbing.

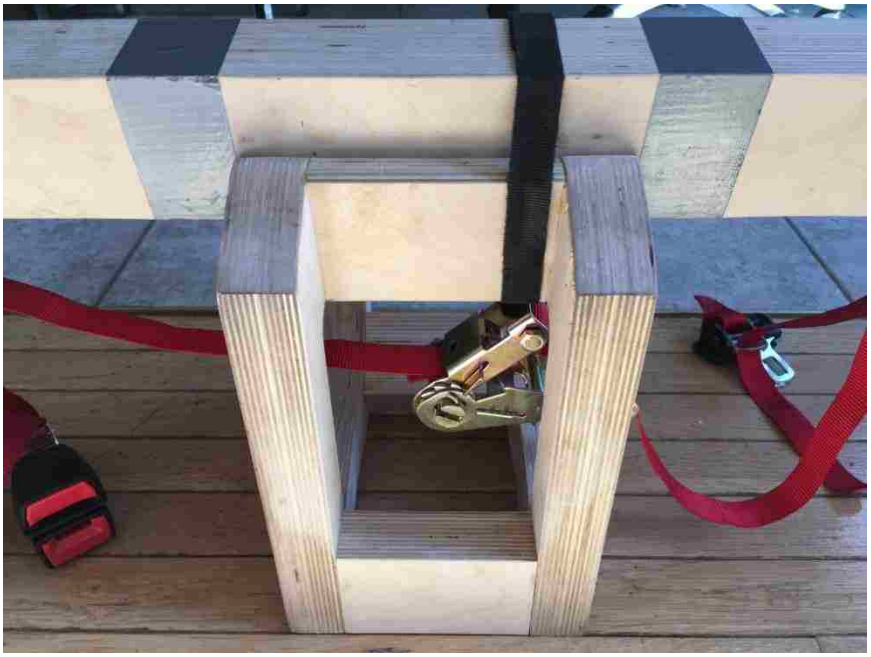

Figure 83. Positioning of the ratchet with the aid of Velcro strap.

The finalized installation steps are listed below. This procedure was used in all future testing from this point.

1. Prepare the CRS according to standard CRS installation procedures [4]. Place the CRS on either side of the rear seat on the vehicle.

2. Attach the LATCH and top tether clips according to standard CRS installation procedures [4].

3. Apply H-clip to the vehicle seatbelt on the outboard side (as explained in Section 4.1.4). Ensure seatbelt clip is sitting at as low position as possible and yet unable to extend with any pulling force.

4. Prepare the CRSIAD into the configuration as shown in Figure 65 from Section 10.1.2.

5. Ensure ratchet is supported by the velcro strap from the loading beam and located the centre of the loading beam. Set the clip and buckle from the ratchet webbing into a matching pattern as vehicle seatbelt system. Ensure the ratchet is in engaged position with no excessive webbing coils in it. If there is excessive coiling, disengage the ratchet and release coiling by pulling webbing out of the ratchet.

6. Place CRSIAD on the top of the CRS with the side marked "FRONT" facing towards the installer.

7. Attach the clip and buckle of the ratchet webbing of the CRSIAD to the corresponding vehicle buckle and clip of the seatbelt system.

8. Tighten the ratchet webbings by using adjustable clips on each end. Ensure the webbing is in a snug state.

9. Complete the setup as shown in Figure 66. The CRSIAD is ready to be used by applying the ratchet.

10. Apply the ratchet to load the CRSIAD into the CRS while feeling the slack between the CRS and car seat cushion. Keep applying the ratchet until the slack is less than one inch in any direction between the CRS and the car seat.

11. With the CRS appropriately preloaded by the CRSIAD, tighten the CRS by pulling the lower anchor webbing until it can no longer extend.

12. Release the CRSIAD by disengaging the ratchet and release ratchet webbing, or press the adjustable clip on either side of the system to release stress.

13. Remove the CRSIAD out of the CRS and installation is complete.

10.4 User Feedback

10.4.1 User Satisfaction Survey

The CRSIAD prototype was tested successfully with all its improvement till this point. However, it was important to collect some average users' feedback to support the worthiness of using CRSIAD as an aid for installing CRS.

A survey questionary sheet was created to effectively collect feedbacks from the users based on the experience of using the CRSIAD. The questions are listed in the section below. A sample user feedback survey sheet is available in Figure Q in Appendix F.

1. Do you think CRSIAD is portable (easy to carry around)?

2. Do you find the device easy to set up?

3. Do you think less physical effort is needed to install CRS with the aid of CRSIAD?

4. Do you think this device will mitigate CRS misuse in terms of installation?

5. Would you buy this device for reasonable price to mitigate CRS misuse to improve children's safety in car accidents?

6. Do you have any recommendation of improving CRSIAD?

Users were to be asked to evaluate the question 1 to 5 with a scale from 0 to 10. All the questions in the survey contain a comment section for the users to provide comments.

A group of fifteen attainable engineers and co-op engineering students were gathered during their leisure time in March 2016 to test the CRSIAD on various personal vehicles. The tested vehicles were all equipped with LATCH. The installation procedure from Section 10.3.5 was provided to the participants for the installation of the CRS with the aid of the CRSIAD. User feedback sheet described above was provided to the users for their feedbacks. The average scores for Question 1 to 5 were calculated and shown in Figure 84.

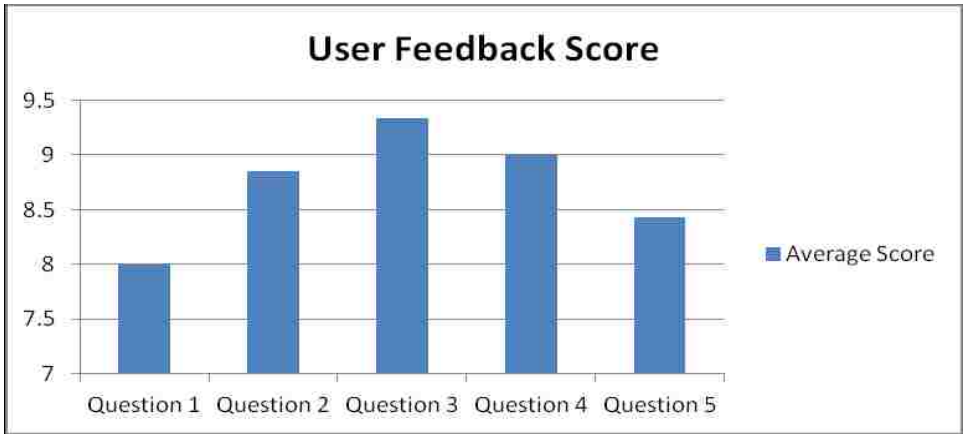

Figure 84. Average scores for all questions in the survey sheet.

The chart reflected a satisfaction level of the users in terms of their experience of using the CRSIAD. The users scored high (average score of 9.3) on Question 3 as they mostly believed the CRSIAD would reduce the physical effort of installing CRS, which was one of the major objectives of constructing the CRSIAD. The Ontario Professional Engineer (OPE) Mr. D. Pereira had complimented on the device's right contour to match the CRS seating surface. The users scored lowest on

Question 1. Eleven users had complained about the weight of the device and they suggested that a lighter material can be used to potentially reduce the weight of the device. Mr. D. Pereira has suggested a swivel handle to be installed on the device so the device can be carried around more easily. The FEA Analyst Engineer Mr. K. Czubernat had mentioned that carrying the device for multiple CRS installations in the same day could be cumbersome due to its weight. For Question 2, the easiness of setup, nine users had commented the procedure being straight-forward and easy to understand and implement. For Question 4 with an average score of 9, users mostly believed that by mitigation of CRS misuse is possible with the use of CRSIAD. Two users commented that the device would be inconvenient for home use but useful for child seat clinic institutions. For Question 5, with a score of 8.4, two users were reserved on purchasing the device for home use. They commented on the size being bulky that it would occupy their housing space. Five users would purchase the device as long as the cost is lower than the CRS itself.

10.4.2 Professional Review

The CRSIAD was at ready-state to be reviewed by the professionals in child safety industry. The feedbacks from the professional personnel were necessary to verify the functionality of the CRSIAD. Their suggestions would be valuable to improve the design of the CRSIAD. With the approval of local Ontario Provincial Police Constable Shawna Coulter (based in Windsor, ON), the CRSIAD was allowed to be brought into a child seat clinic session on February 27th 2016 to be reviewed by OPP officers and constables at Tecumseh, Ontario.

The device was tested on a convertible CRS (Safety 1st Alphaomega 65) in a 2007 Ford Freestyle. A forward-facing configuration installation for CRS was performed (shown in Figure 85). The CRSIAD was used to preload CRS into the second-row seat of the vehicle, followed by the completion of the CRS installation.

The installation was performed by a certified CRS installer while being observed by OPP officers. The CRS was successfully installed with the aid of the CRSIAD.

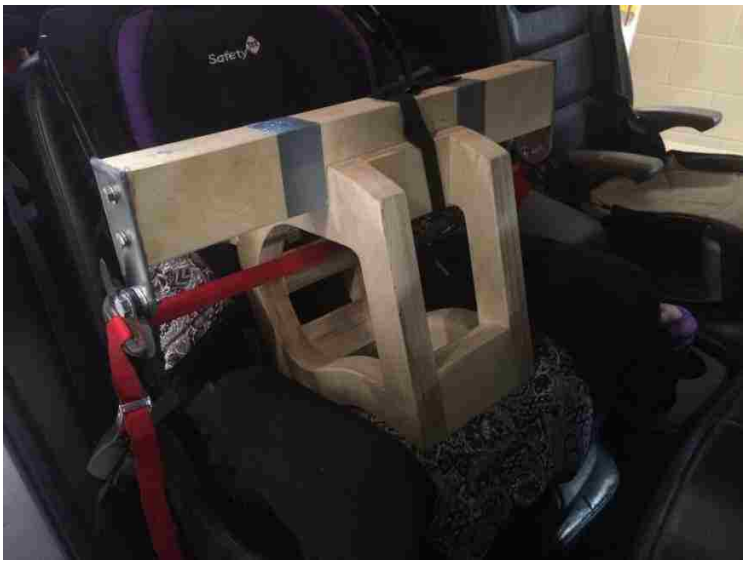

Figure 85. The CRSIAD set up in the test vehicle in forward-facing configuration.

After observing the installation, OPP constable S. Bertoni (based at Harrow, ON) was generally satisfied with the performance of CRSIAD in terms of its functionality. The fact that CRSIAD was loading the CRS towards the lower anchor direction was appreciated and noted as the most effective pre-loading direction for CRS. Officer Bertoni also believed this device was easy to use. He suggested further reduction of the material as he believed some areas of the structure were excessive for the loading condition associated with installation. He commented that the size of the CRSIAD could be more compact. Furthermore, he suggested that the ratchet device would be best if it was located on the top of the loading beam so that it would be easier to operate.

OPP Auxiliary S. Brazil, who also complimented a trial CRS installation with the CRSIAD device, had provided positive feedback on the CRSIAD's functionality as well as easiness to operate. He had also suggested that the size of the device

could be reduced and indicated that - perhaps a different type of tightening mechanism could be adapted to shorten the time necessary for pre-loading. He indicated that the device has the potential to be used at car seat clinic events where time is important.

OPP Constable Ms. S. Coulter (based at Windsor, ON) supported the use of CRSIAD. She suggested a load measurement device should be handy to indicate when to stop the loading process of the CRSIAD. It can be fitted in the webbing of the ratchet assembly to measure load. With the ability to tell when to the loading is sufficient, any potential damage due to overloading of the system can be prevented.

Certified child seat installer Mr. K Czubernat (former FEA Simulation Engineer from FCA Canada, Windsor, Ontario) had successfully performed installation of a CRS with aid of the CRSIAD in his personal vehicle (2005 Saturn Vue). Easiness of using the device was also indicated after completing the installation. An important afterthought was also provided: Any excessive preloading force may prevent users themselves from removing the CRS at later time when necessary. This comment further justified the need for some form of load measuring device to provide user feedback to ensure that the LATCH webbing is not overly tightened. This point also coincided with Officer Coulter's suggestions.

11. Conclusions and Future Work

11.1 Material Testing Data

The material yield and ultimate strengths data are shown in Table 4 and 5 in Section 6.9.

11.2 Material Model Validation and Verification

Complete material model of the CRSIAD is available in Section Appendix D. The validation metrics are available in Section Appendix E. The validation metrics are satisfactory for the material model MAT_WOOD to be used.

11.3 The Final CRSIAD FEA Analysis

The stress levels of the finalized FEA model of the CRSIAD at maximum loading conditions are available in Table 17 from Section 10.3.4. With satisfying stress levels in both forward and rearward configurations, the device was virtually proved that it would not yield under the maximum loading conditions.

11.4 User Feedback and Professional Review

The participated OPP officers and engineers generally appreciated the use of the CRSIAD to help installing CRSs and ensuring a suitable load within LATCH webbing. They all believed that the CRSIAD project is a good start in an effort to mitigating CRS misuse as well as reducing physical effort of installing a CRS into a passenger car.

The successful CRS installation with the aid of the CRSIAD has proved the effort of creating the CRSIAD worthwhile. The use of the CRSIAD has reduced physical effort to install CRS as indicated in Section 10.4.1 - it replaced the need for

the installer to place their knees on the CRS to perform correct CRS installation. The ratcheting mechanism is quick and effective which meets most users' requirement for time-saving. The CRSIAD is also compact with reasonable weight that would favor most female users. Although there are areas for improvement as suggested by professional personnel and surveyed users, the CRSIAD has showed a promising base point on the path of improving child safety and potentially saving many children's lives from car accidents by mitigating CRS misuses.

11.5 Future Geometry Optimization

From users' feedback, the weight of the CRSIAD can be further reduced (Section 10.4.3) for better portability. Although the overall mass of the CRSIAD main frame and beam was weighed to be 5.1 kg, it reached 6.2 kg with the added ratchet assembly and attachments. Moving the entire CRSIAD in and out of the cars could be cumbersome for women.

Further geometry optimization is possible to reduce the overall weight. The device was proven to be robust by both simulation results (Section 10.3.4) and real testing. However, the maximum stress levels in some areas are well under the yielding limits, which made it possible for some amount of material to be further reduced to achieve a lighter weight of the CRSIAD.

The possibility exists for choosing a different material for constructing the CRSIAD since the maximum stress in some fibre directions are well under the yielding limits. The study of selecting more appropriate material with reasonable pricing can be done in the future.

11.6 Future Component Improvement

As suggested by half of the participants who tested the CRSIAD, a more easily accessible tightening mechanism can be used to replace the ratchet assembly. The

device would be easier to operate without having to reach into the CRSIAD structure by hand and operate the ratchet.

Mounting the ratchet on the top surface of the loading beam would seem to be feasible for achieving easy access to the ratchet, which requires modification to the beam and webbing design. Instead of using solid beam as the current design, a hollow beam could be possible to allow appropriate routing of the webbing as well as mounting the ratchet at outboard location.

Load measuring device can be added to the webbing of the CRSIAD to provide users with real-time feedback of the load level in the system as mentioned in Section 10.4.2. An audible warning would be a good feature to remind the installer to stop operating the ratchet when sufficient preload is reached to the CRS. This will prevent the user from either over-tightening the ratchet to cause damage in the CRSIAD or under-tightening the ratchet to cause insufficient preload to the system.

Although ratchet assembly is intuitive and simple to operate, a better and faster mechanism can be convenient to the tightening mechanism of the CRSIAD. For example, a pneumatic cylinder is possible to be used to replace the ratchet as a new tightening device. Loading and releasing pressure can occur more rapidly with the air cylinder than the gear-driven mechanical ratchet, which saves time for the users to operate.

REFERENCES

[1] Federal Motor Vehicle Safety Standards, Standard No. 225; U.S. Department of Transportation, Federal Motor Carrier Safety Administration, Washington, DC.

[2] Klinich, Kathleen D., Manary, Miriam A., Flannagan, Carol A. C., Ebert-Hamilton, Sheila, Malik, L. A., Green, Paul A., and Reed, Mathew P. Labels, Instructions and Features of Convertible Child Restraint Systems (CRS): Evaluating Their Effects on CRS Installation Errors, University of Michigan Transportation Research Institute, Ann Arbor, MI.

[3] LATCH 101: The Basics. https://thecarseatlady.wordpress.com/latch/latch-101-the-basics (2011), accessed on April 5, 2013.

[4] How Child Car Seats Work, Auto Safety and Regulatory Devices. http://auto.howstuffworks.com/car-driving-safety/safety-regulatory-devices/child-car-seat5.htm (2010), accessed on May 6, 2013.

[5] Lawrence E. Decina, Kethy H. Lococo, and Charlene T. Doyle, Child Restraint Use Survey: LATCH Use and Misuse, National Highway Traffic Safety Administration, Washington, DC.

[6] Education Development Center, Inc (EDC), Precious Cargo Child Passenger Safety, Children's Safety Network, Waltham, MA.

[7] Benjamin Hoffman, MD, FAAP, Kathleen Carlson, MS PhD[2], Lindsay DIckey, MPH[2], Adrienne Gallardo, MS[1] and Marianne Bridwell-Chapman, BA[1], Unsafe from the Start: Critical Misuse of Car Safety Seats for Newborns at Initial Hospital Discharge, OHSU Doernbecher Children's Hospital, Portland, OR.

[8] Lawrence E. Decina, Kethy H. Lococo, and Charlene T. Doyle, Child Restraint Use Survey: LATCH Use and Misuse, TransAnalytics, LLC, Kulpsville, PA.

[9] Tsai, Y-F., Perel M, Driver's Mistakes When Installing Child Seats, National Highway Traffic Safety Administration, US Department of Transportation, Washington, DC.

[10] Rothenstein J, Howard A, Parkin P, Khambalia A, Macarthur C. Community paediatricians: counseling patterns and knowledge of recommendations relating to child restraint use in motor vehicles, Faculty of Medicine, University of Toronto, Toronto, ON.

[11] Decina, L.E., Lococo, K., and Block, A. Misuse of Child Restraints: Results of a Workshop to Review Field Data Results. NHTSA Traffic Safety Facts, National Highway Traffic Safety Administration, Washington, DC.

[12] Stephen H.M. Brown, Diane E. Grondin, Jim R. Potvin, Strength limitations to proper child safety seat installation: Implications for child safety, Department of Kinesiology, University of Windsor, Windsor, ON.

[13] Tanya Kapoor, William Altenhof, Anne Snowdon, Andrew Howard, Jim Rasico, Fuchun Zhu, Daniel Baggio, A numerical investigation into the effect of CRS misuse on the injury potential of children in frontal and side impact crashes, Department of Mechanical, Automotive and Materials Engineering, University of Windsor, Windsor, ON.

[14] Federal Motor Vehicle Safety Standards, Standard No. 213, Child Restraint Systems, U.S. Department of Transportation, Federal Motor Carrier Safety Administration, Washington, DC.

[15] Additional Statistics – Child Passenger Safety Week 2013, Child Car Safety and National Highway Traffic Safety Administration (NHTSA), Washington, DC.

[16] Install a child seat, Ontario Ministry of Transportation, www.mto.gov.on.ca/english/safety/install-child-car-seat.shtml (2009), accessed on February 5, 2016.

[17] Samuel J. Record, M.A., M.F. “The Mechanical Properties of Wood”, Part I, Department of Forest Products, Yale University, New Haven, CT.

[18] Ashby, M., et al., Materials: Engineering, Science, Processing and Design, Cambridge University, Cambridge, UK.

[19] Metal Pricing Chart, https://www.metalprices.com (2003), accessed on July 16, 2015.

[20] ASTM D 143 - 94 Standard Test Methods for Small Clear Specimens of Timber, ASTM International, West Conshohocken, PA.

[21] Plywood, https://en.wikipedia.org/wiki/Plywood (June 2013), accessed on June 3, 2015.

[22] Yvonne D. Murray, Manual for LS-DYNA Wood Material Model 143, FHWA-HRT-04-097, Research, Development, and Technology Turner-Fairbank Highway Research Center, Mclean, VA.

[23] Flinn, Richard A.; Trojan, Paul K. Engineering Materials and their Applications. Boston: Houghton Mifflin Company, Boston, MA.

[24] ASTM D 1037 – 99 Standard Test Methods for Evaluating Properties of Wood-Base Fiber and Particle Panel Materials, ASTM International, West Conshohocken, PA.

[25] Ferdinand P. Beer, E. Russel Johnston, Jr., John T. DeWolf, Mechanics of Materials Fourth Edition, 10020, McGraw-Hill Higher Education, New York, NY.

[26] William L. Oberkampf, Timothy G. Trucano, Verification and validation in computational fluid dynamics, Progress in Aerospace Sciences 38 (2002) 209-272, USA.

[27] Yvonne D. Murray, J.D. Reid, R.K. Faller, B.W. Bielenberg, and T.J. Paulsen, Evaluation of LS-DYNA Wood Material Model 143, Research,

Development, and Technology Turner-Fairbank Highway Research Center, Mclean, VA.

[28] Review of Solid Element Formulations in LS-DYNA, Properties, Limits, Advantages, Disadvantages, DYNAmore, Stuttgart.

[29] John O. Hallquist, LS-DYNA Theory Manual; Livermore Software Technology Corporation, Livermore, CA.

[30] Child Passenger Safety: Fact Sheet, Centers for Disease Control and Prevention, Atlanta, GA.

[31] Traffic Safety Facts 2003 Data, National Center for Statistics and Analysis, NHTSA, Washington, DC.

[32] Tanya Kapoor, William Altenhof, Andrew Howard, Jim Rasico, Fuchun Zhu, Methods to mitigate injury to toddlers in near-side impact crashes, Department of Mechanical, Automotive and Materials Engineering, University of Windsor, Windsor, ON.

[33] Children's Safety Network, Precious Cargo: Child Passenger Safety, www.childrenssafetynetwork.org (2001), accessed on May 20th, 2013.

[34] Braver, E.R., Whitfield, R., Ferguson, S.A., Seating positions and children's risk of dying in motor vehicles crashes. Injury Prevention 4, London, UK.

[35] Refaat Hanna, Children Injured in Motor Vehicle Traffic Crashes, National Highway Traffic Safety Administration, Washington, DC.

[36] Yi-Fang D. Tsai and Michael Perel, Drivers' Mistakes When Installing Child Seats, National Highway Traffic Safety Administration, Washington, DC.

[37] 2013 Fact Sheet, Education Development Center, Inc (EDC), Children's Safety Network, Waltham, MA

APPENDICES

Appendix A CRS Measurements Survey

CRS Model	Outer Width (in)	Inner Width (in)	Point 1 (in)		Point 2 (in)	
			X	Y	X	Y
Safety 1st Complete Air LX Convertible		10.5	-14	30	-33	30.5
Cosco Eddie Bauer 3 in 1 - Vancouver	18.1	10.5	-17	34	-34	28.5
DionoRadion RXT Convertible	15.4	10.5	-12	25	-23.5	18.5
Safety 1st Alpha Omega Elite 3 in 1	18.1	10.5	-13	32	-34	15
EvenfloSuperible 65 Convertible	19.5	9	-25	45	-34	33
Britax Marathon Convertible	18.1	9.5	-22	45	-29	32
BritaxPavallion 65 G3	18.9	10	-20	46	-17	29
Graco Multi-stage	19		-17	29	-31	29
Evenflo Maestro Combo Booster	18.8		-22	-29	-31	23.5

CRS Model	Outer Width (in)	Inner Width (in)	Point 1 (in)		Point 2 (in)	
			X	Y	X	Y
Evenflo Symphony 65 DLX All in One	19.1	9	-20	31.5	-39	35
Safety 1st Alphaomega Elite 65 3 in 1	18.1	11	-15	30	-39	29
Evenflo Ex-triumph LX Convertible	20.1	9.5	-11	48	-26	36
Safety 1st Scenera LX Convertible	17.5	10.5	-19	42	-26	34
Evenflo Titan 65	19.5	9	-20	49	-33	33
Safety 1st Guide 65	19.2	11	-22	30	-30	28
Safety 1st Alpha Omega 3 in 1	17.7	10.5	-16	32	-33	30
ClekOobr Full Black Booster		11				
GracoSnugride 35		9				
GracoSnugride 30		9				
BabyTrend EZ Flex-Loc		8.5				
Maxi-CosiMico		9				

CRS Model	Outer Width (in)	Inner Width (in)	Point 1 (in)		Point 2 (in)	
			X	Y	X	Y
Peg Perego Primo Viaggio Sip		9.5				
ChiccoKeyfit		10				
Radian RXT Booster + Convertible		11				
Foonf Convertible		11				
Britax Advocate 65 G3 3 in 1		10				
Britax Boulevard 65 G3 3 in 1		9.5				
Eddie Bauer Alpha Elite	18.1	10.5	-17	34	-34	28.5

Table 18. Survey of attainable CRS models in the stores with design constraints.

Appendix B Specimen Blueprints

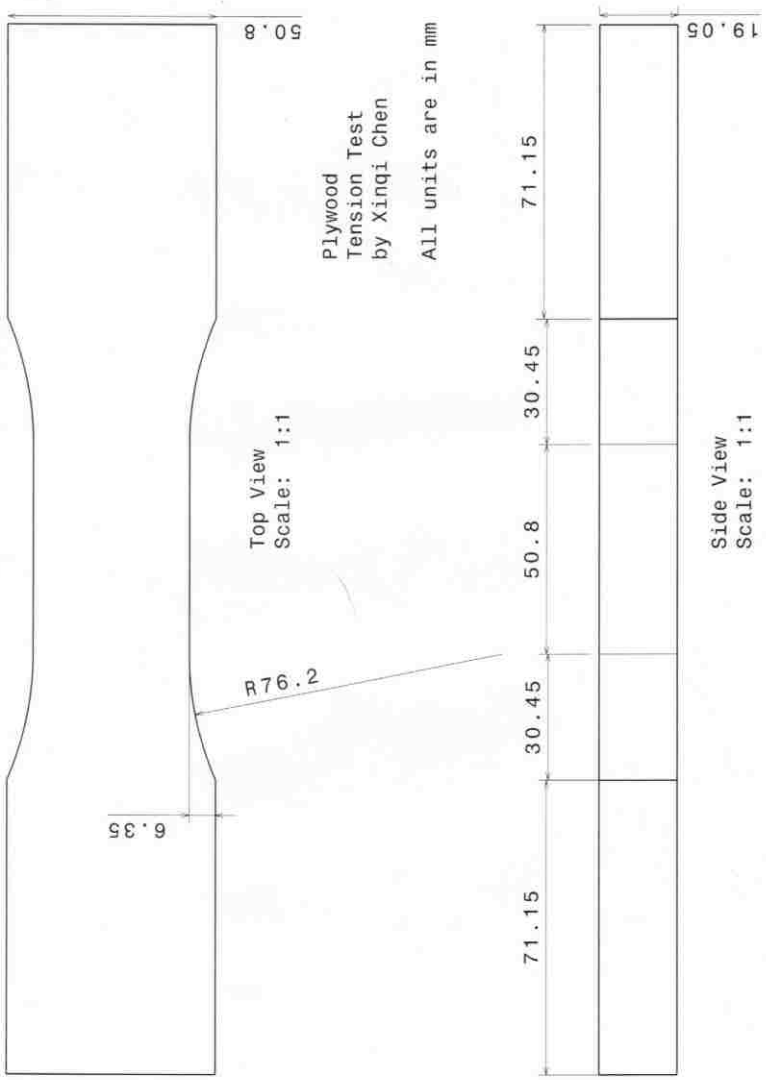

Figure A. Tensile Test Parallel to Surface Specimen.

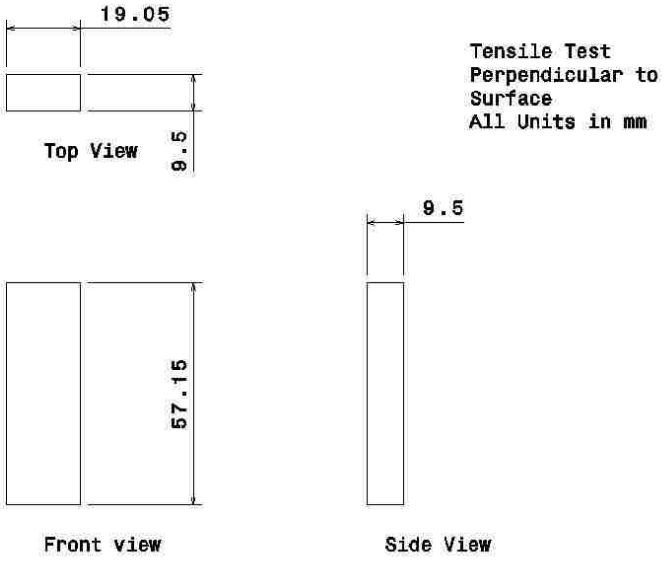

Figure B. Tensile Test Perpendicular to Surface Specimen.

Figure C. Compression Test Parallel to Surface Specimen.

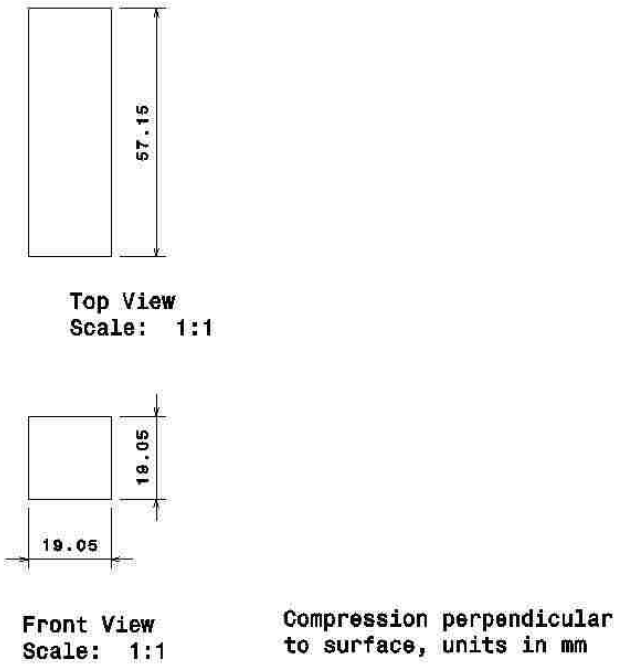

Figure D. Compression Test Perpendicular to Surface Specimen.

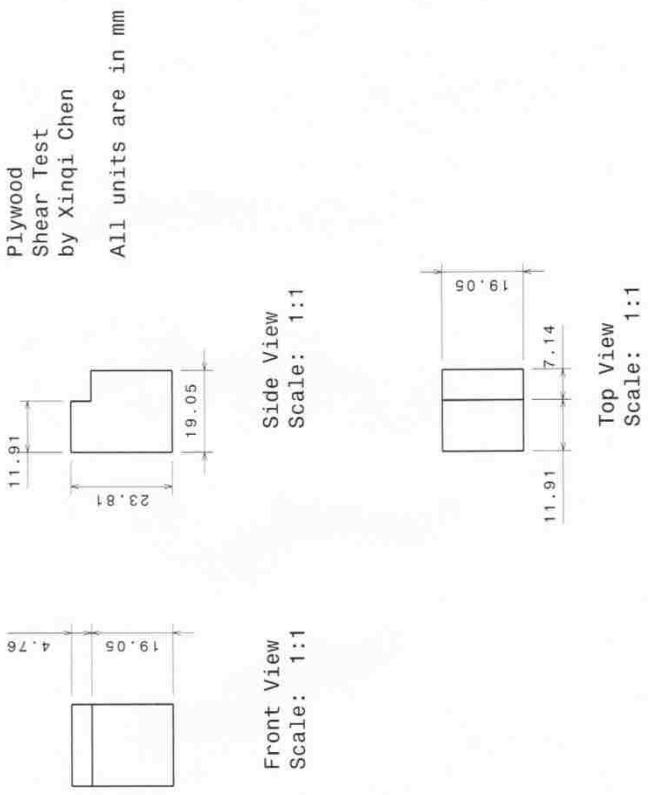

Figure E. Shear Test Parallel to Surface Specimen.

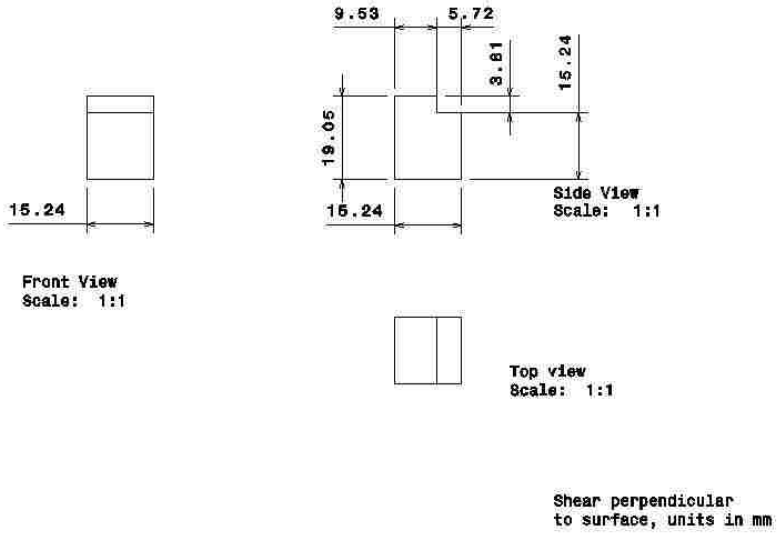

Figure F. Shear Test Perpendicular to Surface Specimen.

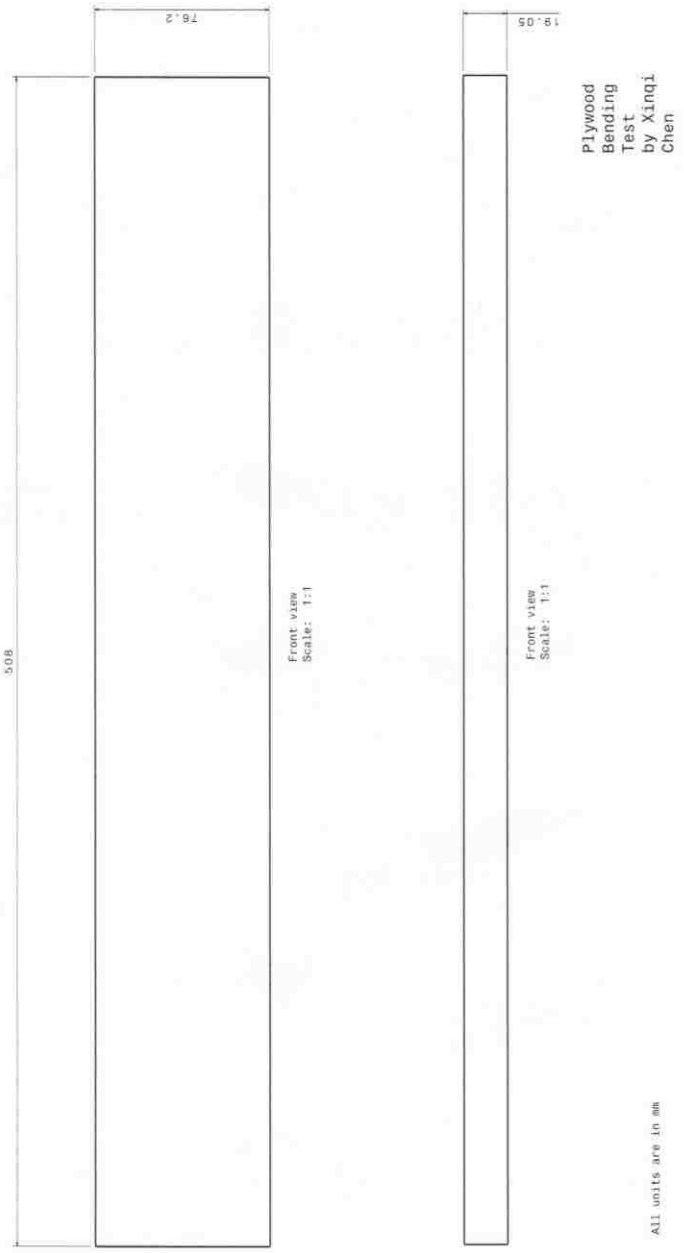

Figure G. Three-point-bending Test Specimen.

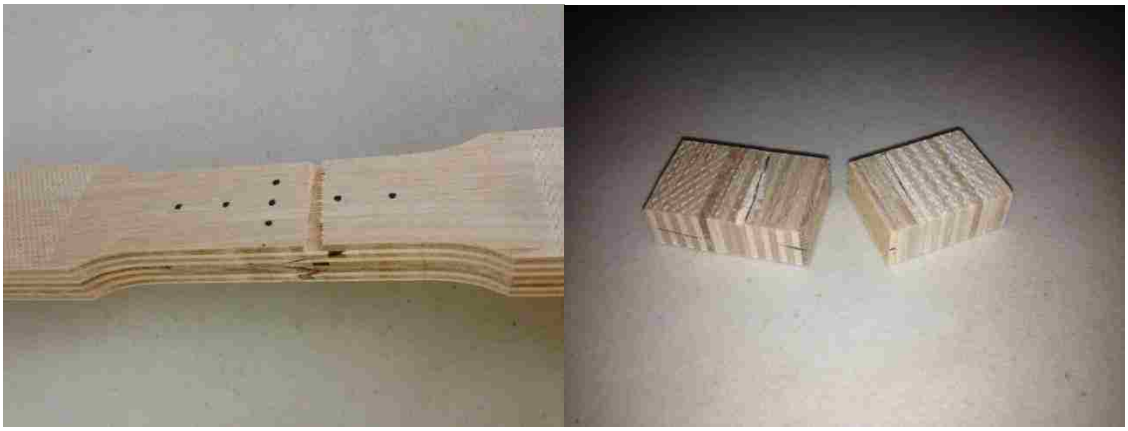

Figure H. Failed Specimen in Tensile Parallel Test (Left), Perpendicular Test (Right).

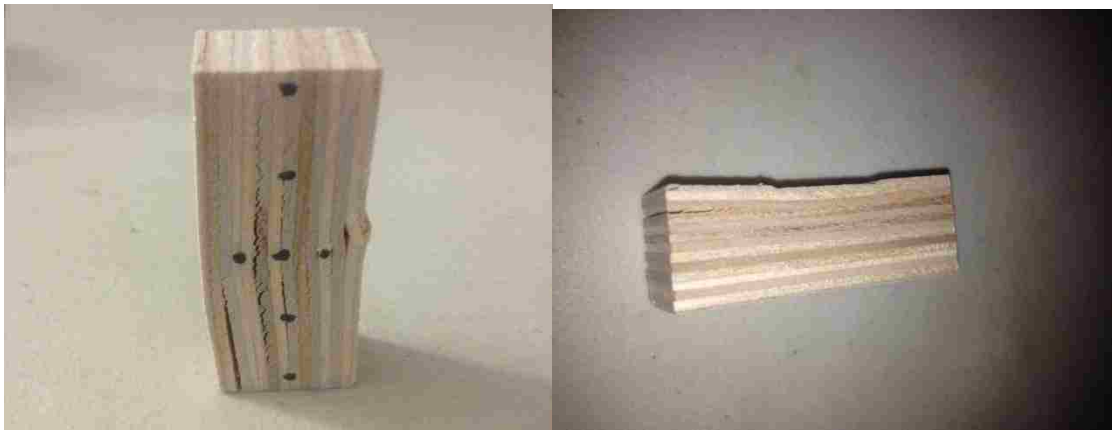

Figure I. Failed Specimen in Compression Parallel Test (Left), Perpendicular Test (Right).

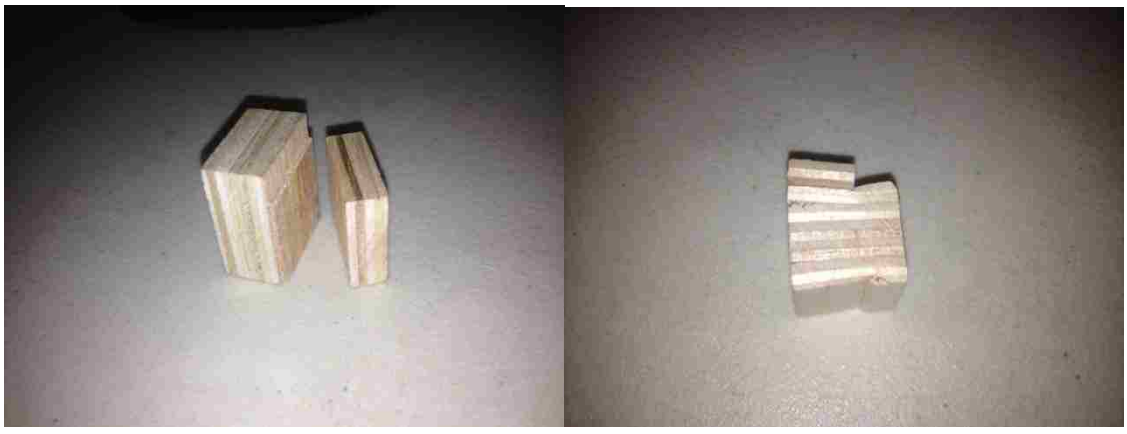

Figure J. Failed Specimen in Shear Parallel Test (Left), Perpendicular Test (Right).

Appendix C Material Testing Raw Data

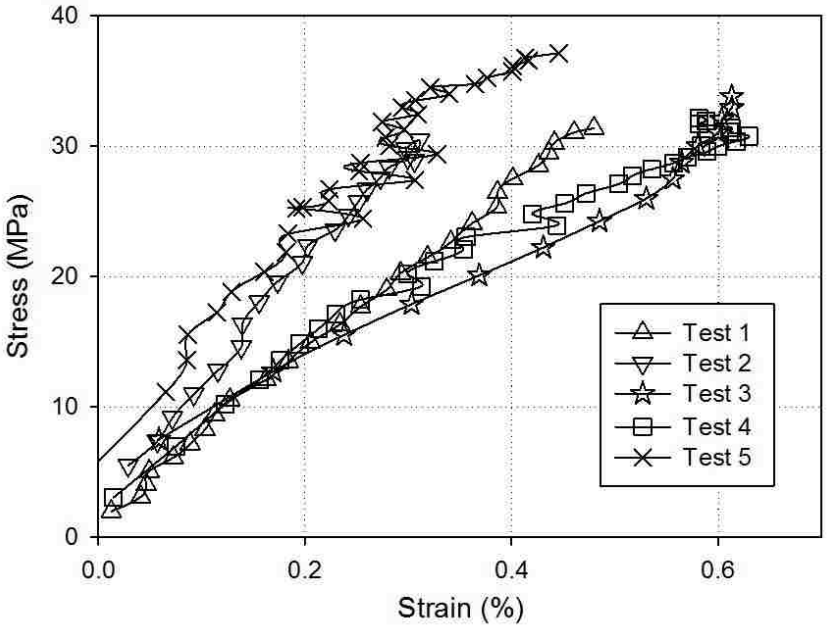

Figure K. Tensile test in parallel direction of the wood fibre.

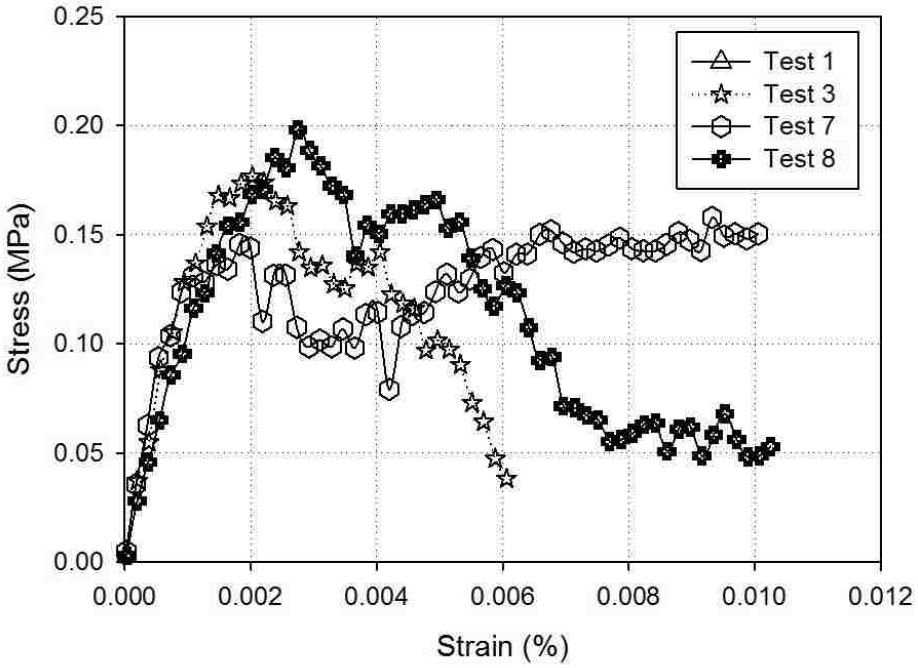

Figure L. Tensile test in perpendicular direction of the wood fibre.

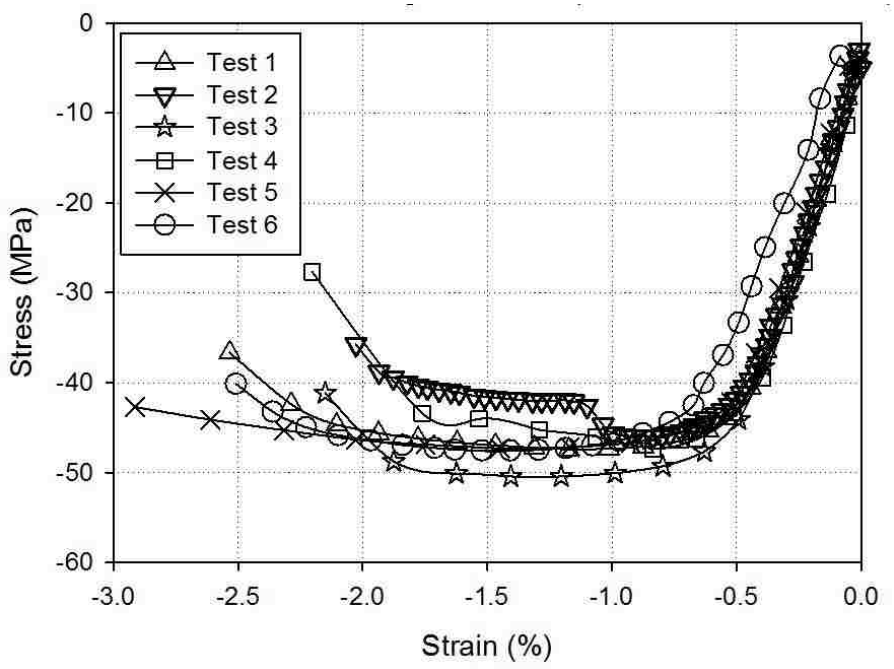

Figure M. Compression test in parallel direction of the wood fibre.

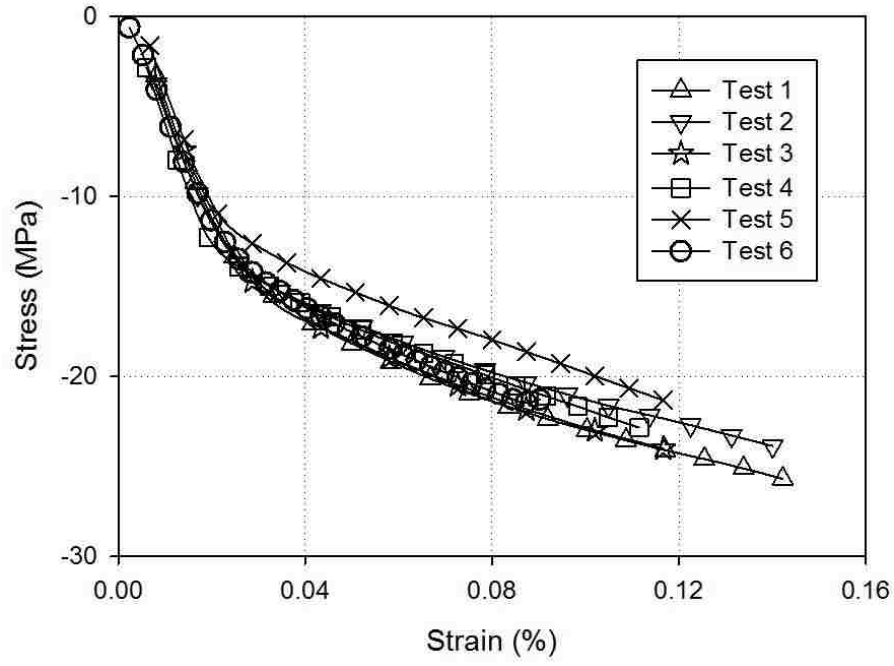

Figure N. Compression test in perpendicular direction of the wood fibre.

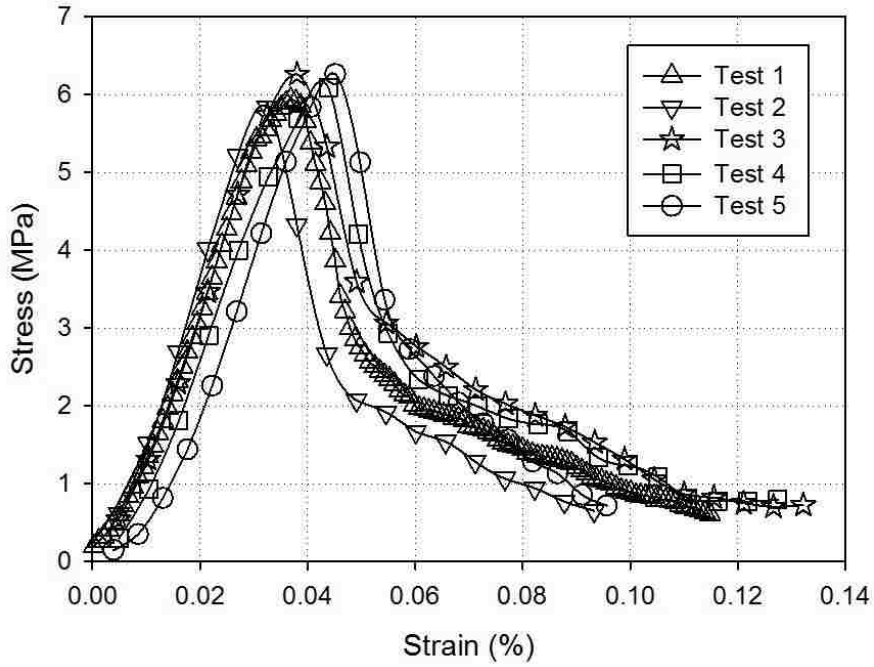

Figure O. Shear test in parallel direction of the wood fibre.

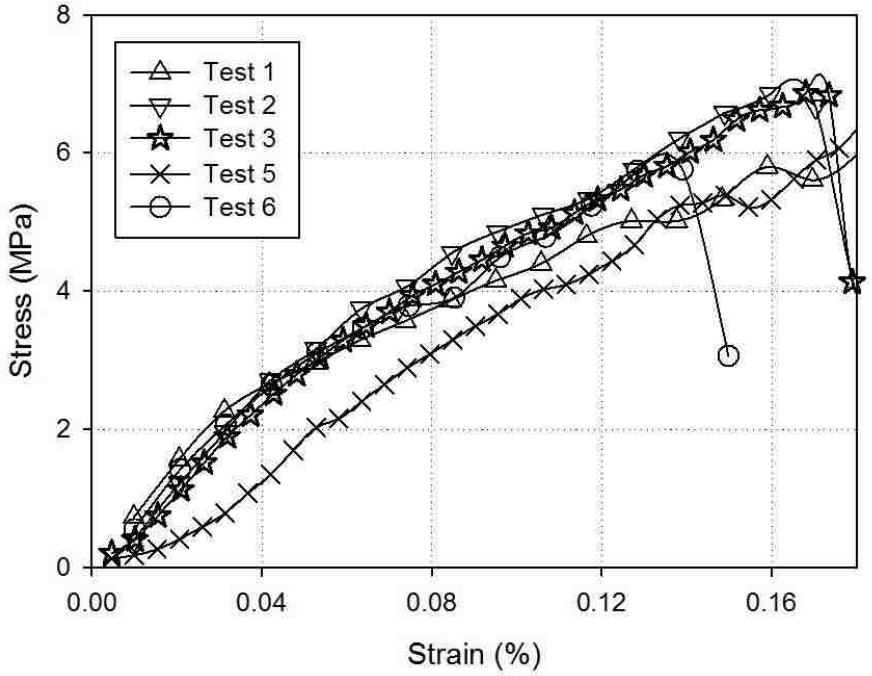

Figure P. Shear test in perpendicular direction of the wood fibre.

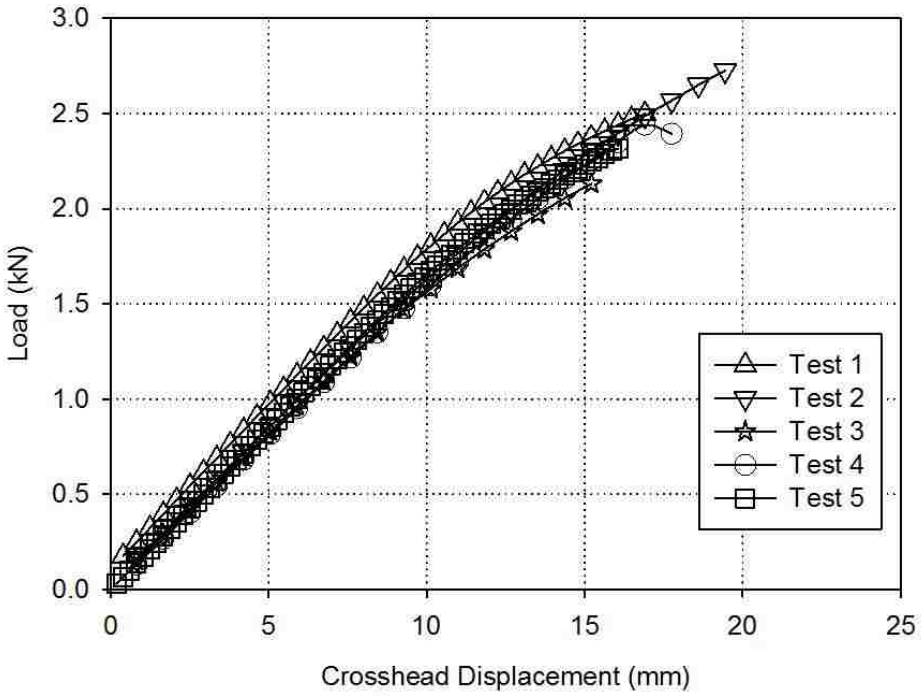

Figure Q. Three-point-bending test.

Appendix D Wood Material Models

	Baltec Plywood (used for constructing the CRSIAD)	Southern Pine	Douglas Fir
EL	9.810 GPa	11.350 GPa	15.190 GPa
ET	4.620E-01 GPa	2.470E-01 GPa	3.240E-01 GPa
GLT	4.970 GPa	7.150E-1 GPa	7.840E-01 GPa
GTR	4.340E-01 GPa	8.800E-02 GPa	1.160E-01 GPa
vLT	0.280	0.160	0.390
XT	3.372E-02 GPa	8.520E-02 GPa	1.076E-01 GPa
XC	4.600E-02 GPa	2.120E-02 GPa	2.390E-02 GPa
YT	2.010E-04 GPa	2.100E-03 GPa	2.300E-03 GPa
YC	9.550E-02 GPa	4.100E-03 GPa	2.500E-03 GPa
S‖	4.440E-03 GPa	9.100E-03 GPa	6.600E-03 GPa
S⊥	2.021E-04 GPa	1.270E-02 GPa	9.300E-03 GPa
Gf I ‖	1.000 GPa*mm	2.234E-02 GPa*mm	2.234E-02 GPa*mm
Gf II ‖	2.300E-03 GPa*mm	8.384E-02 GPa*mm	8.384E-02 GPa*mm
B	2.100E+01	3.000E+01	3.000E+01
dmax‖	9.999E-01	9.999E-01	9.999E-01
Gf I ⊥	1.009E−03 GPa*mm	2.100E-04 GPa*mm	2.100E-04 GPa*mm
Gf II ⊥	2.000E−02 GPa*mm	7.880E-04 GPa*mm	7.880E-04 GPa*mm
D	1.800E+01	3.000E+01	3.000E+01
dmax⊥	9.999E-01	9.999E-01	9.999E-01
N‖	4.000E-01	5.000E-01	5.000E-01
c‖	2.000E+02	4.000E+02	4.000E+02
N⊥	8.500E-01	4.000E-01	4.000E-01
c⊥	1.000E+01	1.000E+02	1.000E+02

Table 19. The developed material Models compared with the Southern Pine material model and the Douglas Fir material model.

Appendix E Material Testing Results

Tensile Parallel	Up to Yield	Up to Failure	**Tensile Perpendicular**	Up to Yield	Up to Failure
Validation Metrics	0.979	0.971	Validation Metrics	0.967	0.883
Accumulated Error	0.021	0.029	Accumulated Error	0.033	0.119
Compression Parallel	Up to Yield	Up to Failure	**Compression Perpendicular**	Up to Yield	Up to Failure
Validation Metrics	0.984	0.965	Validation Metrics	0.929	0.833
Accumulated Error	0.016	0.036	Accumulated Error	0.086	0.210
Shear Parallel	Up to Yield	Up to Failure	**Shear Perpendicular**	Up to Yield	Up to Failure
Validation Metrics	0.979	0.971	Validation Metrics	0.829	0.825
Accumulated Error	0.057	0.093	Accumulated Error	0.185	0.192
3-Point-Bending	Up to Yield	Up to Failure			
Validation Metrics	0.975	0.974			
Accumulated Error	0.052	0.053			

Table 20. Validation Metrics.

Appendix F User Satisfaction Survey of the CRSIAD

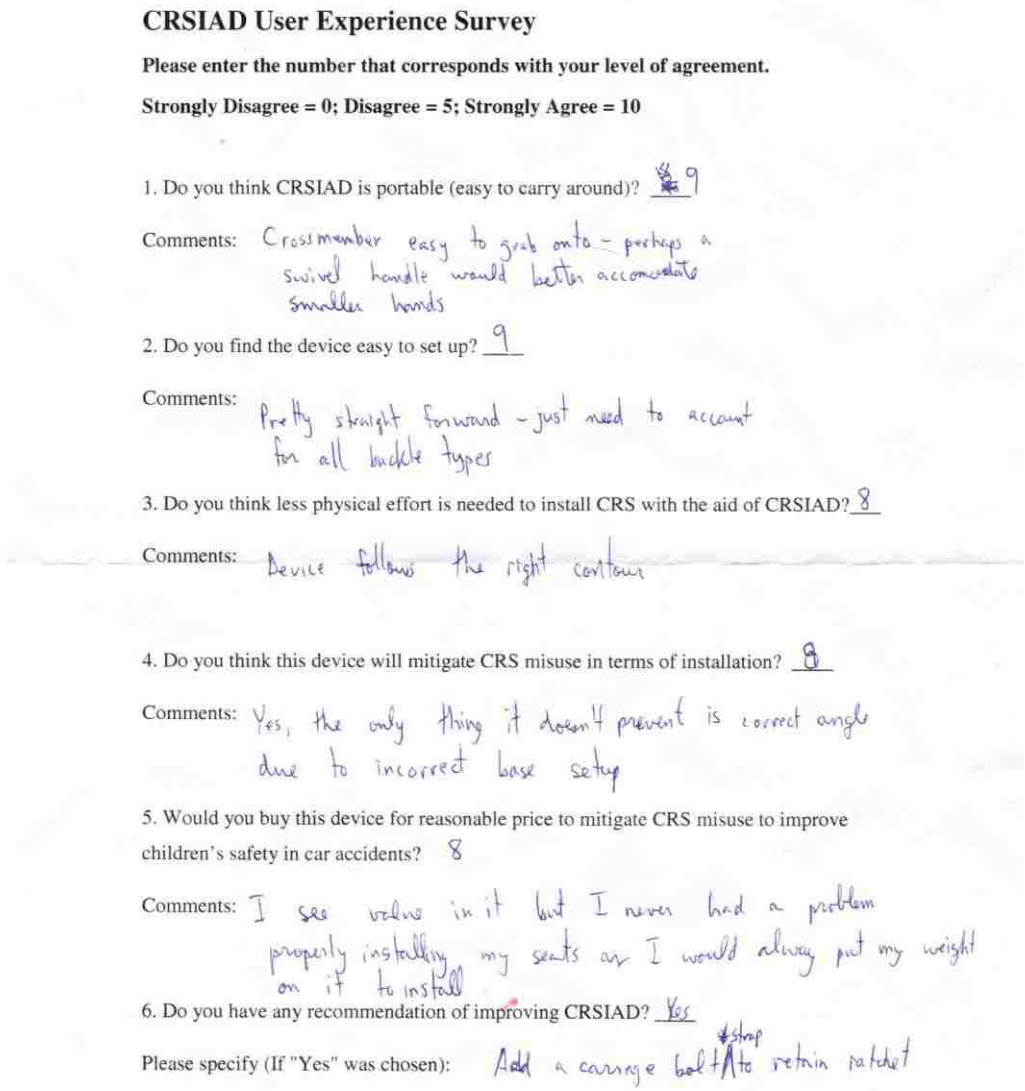

CRSIAD User Experience Survey

Please enter the number that corresponds with your level of agreement.

Strongly Disagree = 0; Disagree = 5; Strongly Agree = 10

1. Do you think CRSIAD is portable (easy to carry around)? 9

Comments: Crossmember easy to grab onto - perhaps a swivel handle would better accomodate smaller hands

2. Do you find the device easy to set up? 9

Comments: Pretty straight forward - just need to account for all buckle types

3. Do you think less physical effort is needed to install CRS with the aid of CRSIAD? 8

Comments: Device follows the right contour

4. Do you think this device will mitigate CRS misuse in terms of installation? 8

Comments: Yes, the only thing it doesn't prevent is correct angle due to incorrect base setup

5. Would you buy this device for reasonable price to mitigate CRS misuse to improve children's safety in car accidents? 8

Comments: I see value in it but I never had a problem properly installing my seats as I would always put my weight on it to install

6. Do you have any recommendation of improving CRSIAD? Yes

Please specify (If "Yes" was chosen): Add a carriage bolt strap to retain ratchet

Figure R. User satisfaction survey from an OPE.

VITA AUCTORIS

NAME: Xinqi Chen

PLACE OF BIRTH: Shanghai, China

YEAR OF BIRTH: 1984

Education:

Shanghai Huadongmofan High School

1999 – 2002

University of Windsor

2004 – 2009